Doctoral Dissertation (Shinshu University)

Effect of melt spinning and drawing conditions on the fiber structure development of polyethylene terephthalate

March 2019

Ren Tomisawa

Interdisciplinary Graduate School of Science and Technology,
Shinshu University
Department of Bioscience and Textile Technology

Table of Contents

Chapter 1

General Introduction

Chapter 1: General Introduction

1. Relationship between processing condition and properties of PET fiber

Polyethylene terephthalate (PET) is a polyester produced by condensation polymerization of terephthalic acid and ethylene glycol, which is firstly synthesized by Whinfield and Dickson in 1941 [1]. PET is the commodity polymer mainly used in the industrial field. Particularly, PET is known as the material of the most produced synthetic fiber. The PET fiber has excellent properties, such as dimensional stability, mechanical and thermal properties, and chemical resistance, and is utilized not only for clothing and home furnishings, but also the reinforcing fiber for tires, belts, and hoses.

In general, synthetic fiber is produced by the spinning, drawing and annealing process. That is, fiber shape is formed by the spinning process with the extension of molten polymer or polymer solution after extrusion from the spinneret. The as-spun fiber is heated and stretched in the drawing process. And the drawn fiber is heat-annealed to stabilize the fiber shape. There are three major spinning methods, wet, dry, and melt spinning. The wet spinning is applied for producing acrylic, rayon, and spandex fibers, the dry spinning is applied for producing acetate, acrylic and poly(vinyl alcohol) fibers, and the melt spinning is applied for nylon, polypropylene and polyester fibers. To improve the molecular orientation and properties of as-spun fiber, it is drawn in most cases. The as-spun fibers are first heated by heating devices, hot roller or hot bath for example, and drawn by take-up roller. By the drawing, the molecular chains oriented along the fiber axis, and the strength of fiber increases.

The properties of PET fibers are strongly influenced by the processing conditions. Particularly, the spinning and drawing processes are important because the fiber structure is mainly formed on these processes by the orientation-induced crystallization. The fiber structure is mostly determined by the drawing process, and the maximum draw ratio is limited by the spinning conditions. Therefore, the mechanical and thermomechanical properties of PET fibers, tensile strength and Young's modulus for example, are depend on the melt spinning and drawing conditions. For example, a partially oriented yarn (POY), obtained at a spinning speed of 2000–4000 m/min, are suitable to produce fibers with a high modulus and low shrinkage, and they are used in products requiring dimensional stability at high temperature, like tire cords. Meanwhile, high-tenacity fibers can be prepared by spinning at low speed and then drawing to a high draw ratio. High-tenacity fibers are used in products requiring high tensile strength, like seat belts [2]. In recent years, a new spinning procedure called laser spinning has been proposed [3, 4]. In this procedure, rapid fiber heating by a laser beam irradiated onto molten fibers lowers the spin-line stress with minimal thermal decomposition. The resulting fibers possess a uniform network structure, which leads to the improved tensile strength of the maximally drawn fibers [3]. There have been similar trials for producing high-strength fibers, so-called "melt structure control", which formed uniform molecular network structures by controlling the melt spinning process [3-10].

The theoretical strength of PET was calculated with assuming an energy elastic deformation of a

perfectly ordered crystal. The theoretical strength and theoretical modulus of polymer was estimated the elastic constants of bond distance, bond angle, and rotation angle of the bond in the polymer chain. Each elastic constant was obtained by the FTIR spectra. The theoretical strength of 28 GPa was obtained for PET crystal [11]. However, the tensile strength of industrially produced fiber could not exceed 5% of the theoretical value. The hierarchic model as shown in Fig. 1.1 was proposed to explain the difference between the properties theoretically estimated by the single crystal and realistic produced fiber. The microfibril is a long fibrillar structure having a few nanometers thickness, and it consist of sequentially repeating crystal and amorphous phases with a long period of approximately 10 nm [12]. Also, the fibrils are thought to be the gathered bundle of microfibrils having several tens of nanometers thickness, and macrofibrils are thought to be the bundle of fibrils having few micrometers thickness [13, 14]. These fibrillar structures have reported for various polymers [15-18]. In particular, the microfibril is important to evaluate the fiber strength from the theoretical strength. So we have payed attention to the morphology forming process of microfibril.
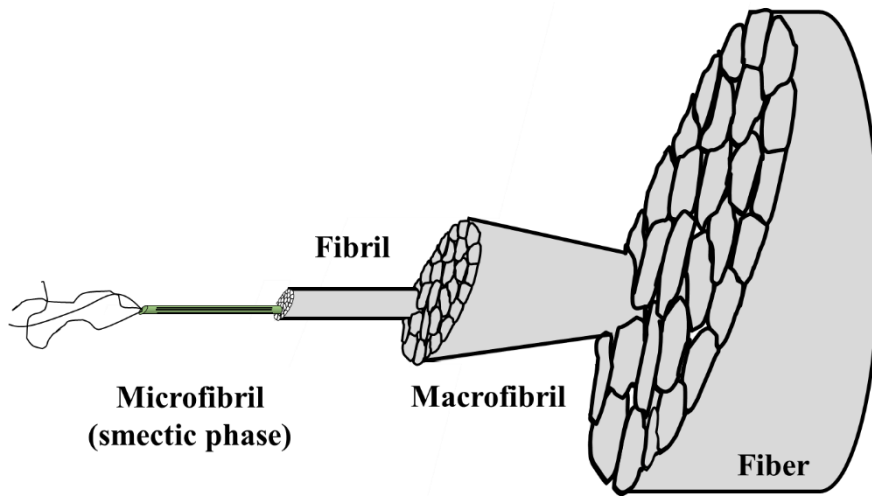
Fig. 1.1 Schematic diagram of hierarchical higher-order structures in fiber.

2. On-line measurement

The fiber structure development with the orientation-induced crystallization was observed by the on-line measurement on the fiber production processes. For example, Haberkorn et al. [19] obtained X-ray images of a polyamide 66 on a high-speed spin-line. They observed the structure development at a time resolution of 0.16 ms, using a fiber running speed of 5500 m/min and a necking width fluctuation of about 3 cm. Kolb et al. [20] obtained X-ray images of PET on a 4000 m/min high-speed spin-line with a time resolution of 0.3 ms. Hirahata et al. conducted an on-line measurement on the orientation-induced crystallization of PET during high speed spinning by means of synchrotron radiation wide angle X-ray diffraction (WAXD) [21]. X-ray studies of the batch drawing process have also been performed; for example, Mahendrasingam et al. [22] and Kawakami et al. [23] observed strain-induced phase-transition phenomena of PET films. Shioya et al. conducted a study on tensile fracture process of PET fibers using time-resolved small angle X-ray scattering (SAXS) [24]. On-line measurement of the continuous drawing process has also been performed. Ran et al. [25] and Wu et al. [26] reported the draw ratio dependence of fiber structure development based on in situ examination of a pin drawing process. However, because fiber structure development in a continuous drawing process is completed within a few milliseconds, it was difficult to monitor the fiber structure development precisely.

It has been suggested that the laser-heated drawing would overcome this difficulty. Because the necking point is held in the range of laser beam by the rapid and homogeneous heating of laser irradiation, changes in diameter [27], temperature [28], and structure after necking can be measured precisely. The temperature profile of the process agreed well with the temperature profile predicted using energy balance equations [29]. WAXD and SAXS patterns were also obtained by using a combination of laser-drawing and an ultrahigh-intensity X-ray source of synchrotron radiation, and they were used to investigate fiber structure development after necking for PET [29–31], polyethylene naphthalate [32], polypropylene [33], polyphenylene sulfide(PPS) [34], polybutylene terephthalate [35], and sea–island conjugated Polystyrene/PET [36]. Particularly, Yamaguchi et al. investigated the structure development of PET fibers drawn to various draw ratios similarly to this work [29-31] and they observed fibrillar-shaped metastable structures. In these studies, it was presumed that this structure is a precursor for microfibrils. This structure is called a smectic phase, which is the mesophase first reported by Bonart [37], and has also been reported for poly(ethylene naphthalate) [38] and poly(butylene terephthalate) [39]. The smectic phase has been reported during batch drawing [23] and heat treatments of oriented amorphous PET [40]. Recently, a higher measurement resolution has been achieved with the use of an undulator-equipped synchrotron X-ray source of the large synchrotron radiation facility (SPring-8) and the high-resolution SOPHIAS X-ray detector [41, 42]. Using this, a d-spacing of smectic phase could be measured with an error of only 0.0006 nm. Moreover, as the new X-ray scattering method, the ultra-small angle X-ray scattering (USAXS) image can be

obtained by longer camera length (several meters). The measurable range of scattering vector q of USAXS is 0.007 to 0.15 nm^{-1} and it corresponds a size of the scattering body of 50–900 nm. Then both the fibril shape of several tens to hundreds of nanometers and an arrangement of the fibrils can be observed by using USAXS.

3. Aims and objectives

There have been a huge number of studies of the relationship between the structure and properties of synthetic fibers, particularly focusing on improvement of their strength. In general, a higher molecular orientation and higher crystallinity increase the strength of synthetic fibers. However, in the case of highly oriented fibers, although the strength increases more with draw ratio, the molecular orientation and crystallinity tend to saturate. That is, the fiber strength cannot be explained by only molecular orientation and its crystallinity.

Some studies have proposed fiber structure models of above-described hierarchical structure [12, 43]. In particular, the two-phase model of crystal and amorphous phases was generally used to analyze the structure of microfibril [44-48]. In this model, microfibrils are considered the fundamental building blocks and they are made of lamellar stacks along the fiber axis. The molecules running through several crystal and amorphous regions are the so-called "intra-fibril tie-chains". Recently, many studies have revealed that the amorphous phase consists of two fractions, mobile amorphous fraction (MAF) and rigid amorphous fraction (RAF). RAF has partial order and is located between the MAF and the crystal regions [49]. RAF should be extended non-crystalline molecules and they seemed to be dispersed in and inter the microfibrils. Some researchers proposed a third phase, which is another phase based on crystal and amorphous phase, to correlate fiber structures and properties [50]. The third phase is seemed to be an oriented intermediate phase located mainly between the microfibrils. That is, RAF and the oriented intermediate phase can be regarded as the so-called "inter-fibril tie-chains". From these models, the fibrillar structure, so-called fibrils or microfibrils are important, that is, the number and tautness of inter-fibril and intra-fibril tie-chains is thought to decide the tensile strength of the resultant fibers. However, there was no measure to analyze the microfibril. Meanwhile, the fibrillar smectic phase, can be evaluate by the on-line measurement explained above, is considered as the precursor of microfibril. Therefore, the state of obtained microfibril can be investigated by the structure development of smectic phase.

Therefore in this study, we attempted to measure the proportion, d-spacing, persistence length, thickness, and second disorder parameter of the fibrillar smectic phase and the high-ordered structure which is long-period and the arrangement of microfibrils to quantify the number and tautness of inter-fibril and intra-fibril tie-chains and the uniformity of the inter-fibril tie-chains by using on-line measurement and ultrahigh intensity X-ray source of SPring-8. Analysis of the spinning speed and draw ratio dependence on the development of these structural parameters based on high-precision data

enables us to discuss the quantitative contributions of inter-fibrillar and intra-fibrillar tie-chains and its uniformity to the mechanical properties of the resultant fibers.

4. Outline

This study incorporates five chapters, with contents summarized as follows:

In Chapter 2, the fiber structure development was analyzed by measuring the time dependence of structural parameters including the amount of smectic phase, d-spacing of smectic phase, degree of crystallinity, and long period. Effect of melt spinning conditions on the fiber structure development of polyethylene terephthalate were investigated.

In Chapter 3, the fiber structure development was analyzed by measuring the time dependence of structural parameters including the amount of smectic phase, d-spacing of smectic phase, degree of crystallinity, and long period. Effect of draw ratio on the fiber structure development of polyethylene terephthalate were investigated.

In Chapter 4, in addition to the proportion and d-spacing, we also estimated the persistence length, thickness, and second disorder parameter of the fibrillar smectic phase. Effect of the spinning speed and drawing stress on the quantitative contributions of inter-fibrillar and intra-fibrillar tie-chains to the mechanical properties of the resultant fibers were investigated.

In Chapter 5, we analyzed the formation of the fibril-size structure after necking using ultra-small-angle X-ray scattering (USAXS). Ultra-SAXS observation of fibril-size structure formation after the necking of poly(ethylene terephthalate) and poly(phenylene sulfide) fiber were investigated.

In Chapter 6, the conclusions of this study were described.

References

1) J. R. Whinfield, J. T. Dickson, *British Patent*, 1941, 578 079 ICI.

2) Y. Liu, L. Yin, H. Zhao, G. Song, F. Tang, L. Wang, H. Shao, Y. Zhang, *J. Appl. Polym. Sci.*, 132, (2015), 42512.

3) M. Masuda, Y. Funatsu, K. Kazama, T. Kikutani, *Sen'i Gakkaishi*, 60, (2004), 338-345.

4) M. Masuda, W. Takarada, T. Kikutani, *Int. Polym. Process*, 25, (2010), 159-169.

5) T. Kikutani, J. Radhakrishnan, S. Arikawa, A. Takaku, N. Okui, X. Jin, F. Niwa, Y. Kudo, *J. Appl. Polym. Sci.*, 62, (1996), 1913-1924.

6) J. Radhakrishnan, T. Kikutani, N. Okui, *J. Text. Res.*, 67, (1997), 684-694.

7) H. J. Jeon, H. Ito, T. Kikutani, N. Okui, M.Okamoto, *J. Appl. Polym. Sci.*, 70, (1998), 665-674.

8) W. Takarada, H. Ito, T. Kikutani, N. Okui, *J. Appl. Polym. Sci.*, 80, (2001), 1575-1581.

9) K. Nakata, Y. Ohkoshi, Y. Gotoh, M. Nagura, Y. Funatsu, T. Kikutani, *Sen'i Gakkaishi*, 60, (2004), 352-355.

10) K. Nakata, F. Nakamura, Y. Ohkoshi, Y. Gotoh, M. Nagura, A. Hamano, S. Takada, T. Kikutani, *Int. Polym. Process*, 27, (2012), 386-391.

11) I. Sakurada, Y. Nukushina, T. Ito, *J. Polym. Sci.*, 57, (1962), 651-660.

12) A. Peterlin, *J. Polym. Sci.*, A-2, 7, (1969), 1151.

13) L. C. Sawyer, R. T. Chen, M. G. Jamieson, I. H. Musselman, P. E. Russell, *J. Material. Sci.*, 28, (1993), 225-238.

14) P. Fratzl, R. Weinkamer, *Progress in Materials Science*, 52, (2007), 1263–1334.

15) S. Yamaguchi, M. Tatemoto. M. Tsuji, *Kobunshi Ronbunshu*, 47, 2, (1990), 105-108.

16) K. Nakamae, M. Kotera, K. Iino, *Sen'i Gakkaishi*, 58, 4, (2002), 99-102.

17) Y. Abe, R. Sakamoto, *Kobunshi Ronbunshu*, 33, 5, (1976), 263-269.

18) K. Shimamura, S. Murakami, M. Tsuji, K. Katayama, Nihon *Reoroji Gakkaishi*, 7, 1, (1979), 42-46

19) H. Haberkorn, K. Hahn, H. Breuer, H.D. Dorrer, P. J Matthies, *J. Appl. Polym. Sci.*, 47, (1993), 1551-1579.

20) R. Kolb, S. Seifert, N. Stribeck, H.G. Zachmann, *Polymer*, 41, (2000), 2931-2935.

21) H. Hirahata, S. Seifert, H. G. Zachmann, K. Yabuki, *Polymer*, (1996), 37, 5131.

22) A. Mahendrasingam, C. Martin, W. Fuller, D. J. Blundell, R. J. Oldman, D. H. MacKerron, J. L. Harvie, C. Riekel, *Polymer*, 41, (2000), 1217-1221.

23) D. Kawakami, B. S. Hsiao, C. Burger, S. Ran, C. Avila-Orta, I. Sics, T. Kikutani, B. Chu, *Macromolecules*, 38, (2005), 91-103.

24) M. Shioya, T. Kawazoe, R. Okazaki, T. Suei, S. Sakurai, K. Yamamoto, T. Kikutani, *Macromolecules*, (2008), 41, 4758.

25) S. Ran, X. Zong, D. Fang, B. S. Hsiao, B. Chu, R. Ross, *J. Appl Crystallogr.*, 33, (2000), 1031-

1036.

26) J. Wu, J. M. Schultz, J. M. Samon, A. B. Pangelinan, H. H. Chuah, *Polymer*, 42, (2001), 7161-7170.

27) W. Okumura, T. Kanegae, Y. Ohkoshi, Y. Gotoh, M. Nagura, *Intern. Polym. Proc.*, 18, (2003), 46-52.

28) W. Okumura, T. Yamaguchi, Y. Ohkoshi, Y. Gotoh, M. Nagura, *Intern. Polym. Proc.*, 17, (2002), 124-132.

29) T. Yamaguchi, K. Komoriyama, Y. Ohkoshi, H. Urakawa, Y. Gotoh, N. Terasawa, M. Nagura, K. Kajiwara, *J. Polym. Sci., Polym. Phys.*, 43, (2005), 1090-1099.

30) T. Yamaguchi, K. H. Kim, T. Murata, M. Koide, S. Hitoosa, H. Urakawa, Y. Ohkoshi, Y. Gotoh, M. Nagura, M. Kotera, K. Kajiwara, *J. Polym. Sci., Polym. Phys.*, 46, (2008), 2126-2142.

31) K. H. Kim, T. Yamaguchi, Y. Ohkoshi, Y. Gotoh, M. Nagura, H. Urakawa, M. Kotera, T. Kikutani, *J. Polym. Sci., Polym. Phys.*, 47, (2009), 1653-1665.

32) K. H. Kim, R. Aida, Y. A. Kang, T. Ikaga, Y. Ohkoshi, I. Wataoka, H. Urakawa, *Polymer*, 53, (2012), 4272-4279.

33) Y. A. Kang, K. H. Kim, S. Ikehata, Y. Ohkoshi, Y. Gotoh, M. Nagura, M. Koide, H. Urakawa, *Polymer*, 52, (2011), 2044-2050.

34) K. Ide, T. Ikaga, Y. Ohkoshi, I. Wataoka, M. Masuda, Y. Maeda, *Sen'i Gakkaishi*, 70, (2014), 76-83.

35) K. H. Kim, Y.A. Kang, A. Yokoyama, T. Ikaga, Y. Ohkoshi, I. Wataoka, H. Urakawa, *Polymer*, 44, (2012), 1030-1035.

36) K. Sugawara, T. Ikaga, K.H. Kim, Y. Ohkoshi, K. Okada, H. Masunaga, T. Kanaya, M. Masuda, Y. Maeda, *Polymer*, 79, (2015), 37-46.

37) R. Bonart, *Kolloid-Z*, 213, (1966), 1-11.

38) K. H. Kim, R. Aida, Y. A. Kang, T. Ikaga, Y. Ohkoshi, I. Wataoka, H. Urakawa, *Polymer*, 53, (2012), 4272-4279.

39) T. Konishi, Y. Miyamoto, *Polymer*, 42, (2010), 349-353.

40) T. Asano, F. J. Balta Calleja, A. Flores, M. Tanigaki, M. Mina, C. Sawatari, H. Itagaki, H. Takahashi, I. Hatta, *Polymer*, 40, (1999), 6475-6484.

41) T. Hatsui, M. Omodani, T. Kudo, K. Kobayashi, T. Imamura, T. Ohmoto, A. Iwata, S. Ono, Y. Kirihara, T. Kameshima, *Proc. Int. Image Sensor Workshop*, 2013, Art. No. 3.05. http://www.imagesensors.org/Past%20Workshops/2013%20Workshop/2013%20Papers/03-_058_hatsui_paper.pdf

42) T. Hatsui, H. Graafsma, *IUCrJ*, 2, (2015), 371-383.

43) D. C. Prevorsec, *J. Polymer Sci. Symposium* no. 32, (1971).

44) R. Huisman, H. M. Heuvel, *J. Appl. Polym. Sci.*, 37, (1989), 595.

45) B. K. Samui, M. P. Prakasan, C.; amesh, D. Chakrabarty, R. Mukhopadhyay, *J. Text. I*, 104, (2013), 35.

46) P. B. Rim, C. J. Nelson, *J. Appl. Polym. Sci.*, 42, (1991), 1807.

47) N. S. Murthy, D. T. Grubb, *J. Polym. Sci. Polym. Phys.*, 41, (2003), 1538.

48) N. S. Murthy, D. T. Grubb, K. Zero, C. J. Nelson, G. Chen, *J. Appl. Polym. Sci.*, 70, (1998), 2527.

49) R. Rastogi, W. P. Vellinga, S. Rastogi, C. Schick, H. E. H. Meijer, *J. Polym. Sci. Polym. Phys.* 42, (2004), 2092.

50) Y. G. Fu, B. Annis, A. Boller, Y. M. Jin, B. Wunderlich, *J. Polym. Sci. Polym. Phys.*, 32, (1994), 2289.

Chapter 2

Effect of melt spinning conditions on the fiber structure development of polyethylene terephthalate

Chapter 2: Effect of melt spinning conditions on the fiber structure development of polyethylene terephthalate

1. Introduction

In this Chapter, the effects of the spinning conditions on the fiber structure development of polyethylene terephthalate after continuous neck-drawing were investigated using simultaneous WAXD/SAXS measurements. That is, here we analyze the effects of a spinning speed of 500–2000 m/min and laser spinning on the development of PET fiber structure. The fiber structure development is analyzed by measuring the time dependence of structural parameters including the amount of smectic phase, d-spacing of smectic phase, degree of crystallinity, and long period.

2. Experimental

2.1. Samples

The fibers used for drawing in this study were prepared by melt spinning PET (IV=1.3 dL/g) provided by Toray Co. The polymer was heated 310 °C, extruded from a nozzle with a single hole at a mass flow rate of 4.8 g/min, and taken up at 500–2000 m/min. The nozzle diameter (D) was 1.0 mm, and L/D = 3. In addition, CO_2 laser irradiation from three directions was focused onto the fibers at a position just under 2.5 mm from the nozzle, and taken up at 500 m/min. This process is hereafter referred to as laser spinning. The random polarized laser beam, whose wavelength and diameter were 10.6 μm and 4.5 mm, respectively, was generated by a PIN-60R laser (Onizuka Glass Co., Ltd.). The emitted laser beam was branched into four by a beam splitter. One branch was used to monitoring the beam power, while the other three were irradiated onto the fiber from three directions at an angle of 120° from each other in a horizontal plane. The laser power per branch was 10 W.

2.2. Drawing

The drawing system was the same as reported elsewhere [1]. A fiber was fed continuously from a feed roller, heated by the CO_2 laser beam, and drawn by the speed difference between the feed and take-up rollers. The fiber running speed after necking was fixed at 110 m/min, and the draw ratio was changed by modulating the fiber feeding speed. A random polarized laser beam with a wavelength and diameter of 10.6 μm and 6 mm, respectively, was generated by a PIN-30R laser (Onizuka Glass Co., Ltd.). The beam was irradiated onto the running fiber from three different directions. The drawing tension was measured by a tension meter (HS-1500S, Eiko Sokki Co., Ltd.). A 100-gf pickup was installed between the neck-drawing point and take-up roller. The drawing stress was calculated from the drawing tension and diameter of the drawn fiber.

2.3. Online measurement

The principle of the online measurement system was reported previously [1]. WAXD/SAXS patterns were obtained by irradiation of an X-ray beam onto the running fiber. The X-ray beam was 40 μm in the vertical direction and 50 μm in the horizontal direction. By moving the laser irradiation position, the distance from the necking point to the X-ray irradiation position was changed. The elapsed time after necking was calculated by dividing the distance by the running speed of the fiber.

The synchrotron X-ray beam used in this study was from SPring-8 BL03XU (FSBL), and an undulator was used to obtain an ultrahigh-intensity X-ray beam. The wavelength of the X-ray beam was 0.10 nm. For WAXD and SAXS measurements, the camera length was 78.7 and 1788 mm, respectively, exposure time for each measurement was 1 and 50 s, respectively, and the detector was a 1032 × 1032 pixel flat panel detector (50 μm/pixel) and 672 × 512 pixel CCD (126 μm/pixel), respectively. After the subtraction of air scattering, the obtained image was normalized by the total integrated intensity to compensate for the fluctuation of X-ray irradiation volume.

The average position of the necking point and its fluctuation width were determined by analysis of still images taken from the video movie recorded during each measurement. The resolution time was calculated by a reported method [2] by the position resolution, which was calculated from the fluctuation width of the necking point (0.09–0.20 mm), length of the necking point (0.12–0.31 mm), and width of the X-ray beam (0.05 mm). The obtained time resolution was 0.09–0.18 ms.

2.4. Birefringence

The birefringence for each fiber was measured by a polarized microscope (BX51-33POC, Olympus Co., Ltd.) with a monochromic filter of 546 nm. Tricresyl phosphate was used as an immersion oil. The average and standard deviation of birefringence were calculated for 10 samples.

2.5. Thermomechanical tests

Thermal and mechanical properties of drawn fibers were analyzed by tensile tests, thermomechanical analysis (TMA), and differential scanning calorimetry (DSC). The strength, elongation, Young's modulus, and natural draw ratio (NDR) were measured by a universal testing machine (Autograph AGS-X, Shimadzu Co. Ltd.) equipped with a 50 N load cell and air chuck. The sample length and elongation rate were 40 mm and 100 %/min, respectively, and the average and standard deviation of the strength, elongation, and Young's modulus were calculated for every ten samples. The NDR was defined as the draw ratio at which the tensile stress began to rise again with the dissipation of necking point.

A thermomechanical analyzer (TMA/SS6100, SII Nanotechnology Inc.) was used to measure thermal shrinkage factor and shrinkage stress at heating rates of 5 and 10 K/min, respectively. The sample length was 10 mm for both measurements. DSC was conducted using a calorimeter

(Thermoplus DSC8230, Rigaku Co. Ltd.) with a heating rate of 10 K/min. A powdered cut fiber sample was used for DSC measurements. The melting point and crystallinity were determined from the peak position and the heat of fusion of the DSC curve. The heat of fusion of a PET crystal (135 J/g) was used for the calculations.

3. Results and discussion

3.1. As-spun fibers

The formation conditions, structure, and physical properties of as-spun fibers are listed in Table 2.1 and 2.2. Crystallinity and birefringence increased while NDR and elongation decreased as spinning speed increased. In particular, because of its higher crystallinity and lower cold crystallization temperature than those of the other samples, the fiber taken up at 2000 m/min can be regarded as a POY. In contrast, the laser-spun fiber possesses lower molecular orientation and crystallinity than the fiber spun without laser irradiation. The laser-spun fiber also shows higher NDR and cold crystallization temperature than the others. Both lower spinning speed and laser irradiation of the spin line should decrease the spin line stress, and result in lower molecular orientation of the as-spun fiber. The lower spinning stress should also suppress oriented-induced crystallization, causing the large NDR and elongation at break.

Table 2.1 Spinning conditions and structural parameters of as-spun

Sample	Take-up speed / m/min	Birefringence	NDR	Cold crystallization temperature / °C	Melting temperature / °C	Crystallinity / %
500L	500 (Laser spinning)	0.002	3.4	146	252	5
500	500	0.004	3.0	136	253	8
1000	1000	0.009	2.4	132	254	10
1500	1500	0.019	1.9	126	254	13
2000	2000	0.023	1.5	119	253	26

Table 2.2 Mechanical and thermomechanical properties of as-spun

Sample	Tensile strength / MPa	Elongation / %	Young's modulus / GPa
500L	147	620	1.8
500	175	616	2.2
1000	215	407	2.2
1500	283	312	2.3
2000	322	213	2.5

Table 2.3 Drawing conditions and structural parameters of drawn fibers.

Sample	As-spun fiber	Draw ratio	Laser power /W	Drawing stress / MPa	Fiber temperature / °C 0 ms	Fiber temperature / °C 2 ms	Birefringence	Melting temperature / °C	Crystallinity / %
500L-L	500L	3.4	18.5	16	110	139	0.132	254	27
500L-H		5.1	21	106	146	194	0.213	256	42
500-L	500	3.0	18.4	22	108	136	0.118	255	28
500-H		4.2	21.5	103	142	189	0.182	254	40
1000-L	1000	2.5	22.5	24	104	143	0.129	255	32
1000-H		3.3	23	99	129	178	0.188	257	40
1500-L	1500	2.1	21.1	31	95	134	0.134	256	33
1500-H		2.7	25	105	118	171	0.167	257	38
2000-L	2000	1.9	23.3	48	94	138	0.147	253	34
2000-H		2.1	26.4	109	98	150	0.173	257	38

Table 2.4 Mechanical and thermomechanical properties of drawn fibers.

Sample	Tensile strength / MPa	Elongation / %	Young's modulus / GPa	Shrinkage at 200 °C / %	Maximum shrinkage stress Stress / MPa	Maximum shrinkage stress Temperature / °C
500L-L	532	87	6.9	4	18	82
500L-H	1100	29	12.5	9	84	180
500-L	582	95	7.6	5	17	101
500-H	916	38	12.6	9	72	180
1000-L	633	85	8.2	2	27	83
1000-H	897	34	11	8	76	186
1500-L	653	73	7.8	3	26	153
1500-H	847	38	10.8	6	59	195
2000-L	698	52	9.2	4	41	162
2000-H	880	36	11	6	72	194

3.2. Drawing

As shown in previous work, fiber structure development depends on the draw ratio [3]. Therefore, the selection of draw ratio is important to compare the effect of spinning conditions on fiber properties. The minimum and maximum draw ratios that a fiber can be stably drawn at in a continuous drawing process should be strongly related to the NDR and elongation at break of the as-spun fiber, respectively. Therefore, in this study, we planned to select the drawing conditions with both the minimum and maximum stable drawing stress or draw ratio for each set of spinning conditions. Selection of the latter was difficult because the fiber tended to break through the fluctuation of drawing stress during the measurement, so a unified drawing stress of about 100 MPa (actually 99–109 MPa) was used instead of the maximum stable drawing stress. This stress was close to the maximum drawing stress of 109 MPa of a fiber taken up at 2000 m/min, and somewhat lower than that of a fiber taken up at 500 m/min, which can be drawn stably up to a stress of 149 MPa. This indicates that there was a somewhat larger margin of the acceptable draw ratio when the fiber was taken up at 500 m/min; that is, the draw ratio was about 58% of the breaking draw ratio at room temperature, while they were 65%–70% for the other spinning conditions. Meanwhile, the minimum stable draw ratio was almost equal to the NDR except for a take-up speed of 2000 m/min, for which a higher draw ratio was needed to obtain stable drawing.

The drawing conditions, structural parameters, and physical properties of drawn fibers are listed in Table 2.3 and 2.4. The minimum stress for stable drawing decreased as spinning speed lowered and also by laser spinning. The minimum drawing stress should correspond to the stress at the natural drawing region, that is, the yield stress. Then, the minimum drawing stress increased with increasing molecular orientation driven by the rise of yield stress. The higher crystallinity, tensile strength, Young's modulus, and shrinkage stress of the minimally drawn fiber can be explained by the increase of drawing stress. In contrast, despite the clear increase of drawing stress, birefringence of the drawn fibers did not change much.

For the fibers exposed to a drawing stress of 100 MPa, the thermal shrinkage, tensile strength, and initial modulus increased with decreasing spinning speed and by laser spinning. Conversely, the elongation at break, thermal shrinkage stress, crystallinity, and birefringence of the fibers did not change much. Although these fibers were drawn under similar drawing stress and possessed similar structural parameters, clear differences in the properties of the drawn fibers were observed for the fibers obtained under different spinning conditions. These results show that the force-bearing structure in the drawn fibers cannot be represented only by crystallinity and birefringence, indicating the necessity of examining additional information about the structure. We explain the dependence of fiber properties on spinning conditions by considering the fiber structure development.

3.3. Fiber temperature profile

Because the crystallization rate depends on temperature, the fiber temperature profiles around the neck drawing point were estimated from the experimental conditions. Profiles were calculated using an energy balance equation that considered laser irradiation energy, heat transfer from the fiber surface, work of plastic deformation by an external force, and latent heat of crystallization [4]. The absorption coefficient of PET of 1.149×10^4 m^{-1} obtained for the wavelength of the laser beam was used to estimate laser irradiation energy [4]. The heat transfer coefficient was calculated using the experimental formula proposed by Kase and Matsuo [5]. To determine the heat of crystallization, the heat of fusion of drawn fibers was measured by DSC.

The estimated fiber temperature profiles are plotted against the distance from the laser beam axis in Fig. 2.1. Fiber temperature began to rise from −3 mm when the laser beam begin to irradiate the fibers. When the fiber temperature approached the glass transition temperature of PET, it increased steeply because of the plastic deformation that occurred during necking. The temperature continued to increase after necking because of the laser irradiation and latent heat of crystallization, and reached its maximum value at the edge of the laser beam (+3 mm). Fiber temperature then decreased to room temperature through heat transfer. Almost the same maximum temperature was estimated for all fibers drawn at the minimum draw ratio (Fig. 2.1(a)), while the maximum temperature increased with decreasing spinning speed at a drawing stress of 100 MPa (Fig. 2.1(b)). The increase of maximum temperature for the latter situation can be explained by the increase of the applied work for plastic deformation with increasing draw ratio.

As described in Section 3.6, the crystallization rate was estimated from the change of crystallinity until 2 ms after necking in this study. Thus, the estimated fiber temperature immediately after necking and 2 ms after necking are both shown in Table 2.3 and Fig. 2.1. The fiber temperature rises about 40 or 50 °C in this time for each respective set of drawing conditions.
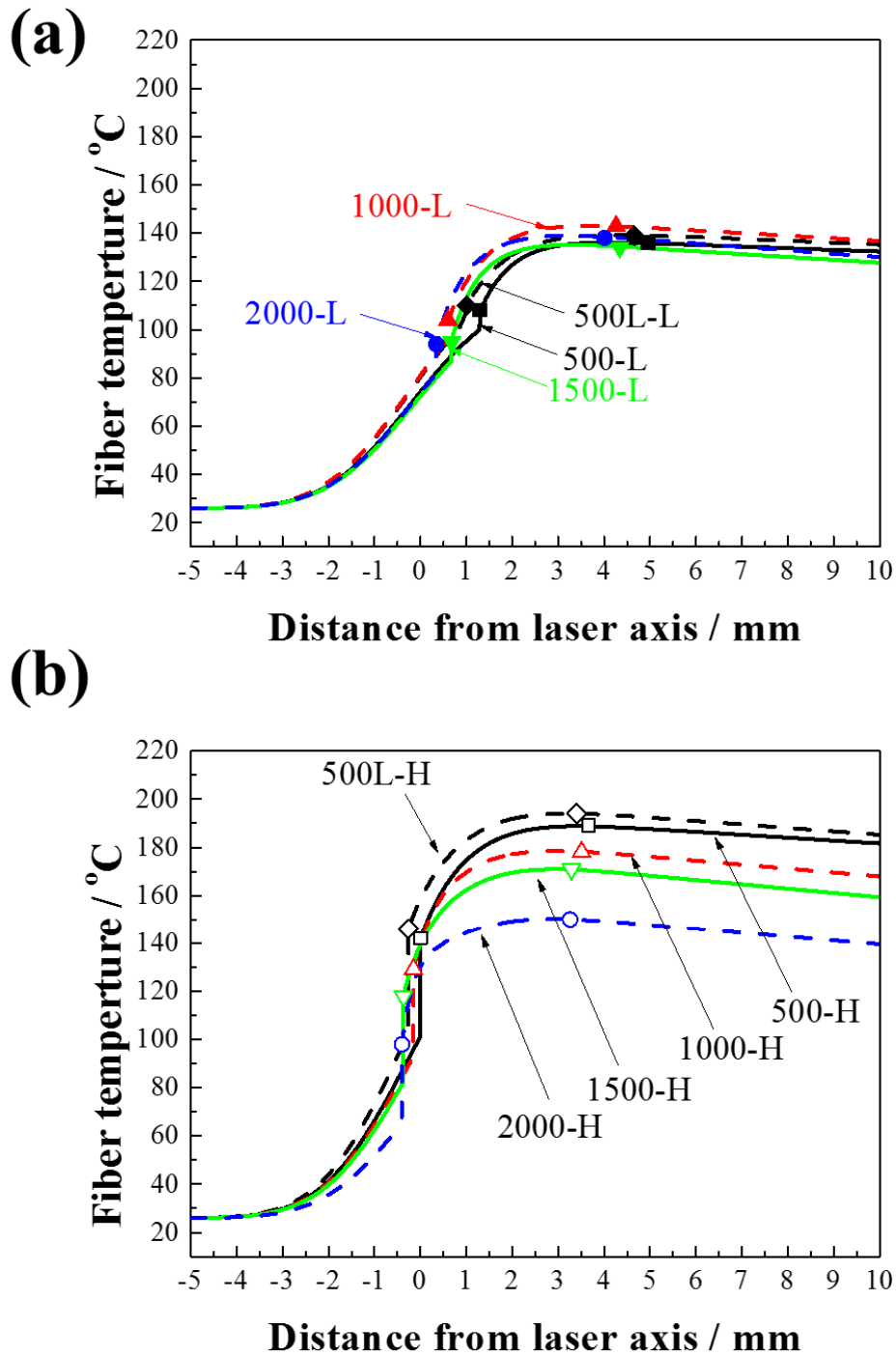
Fig. 2.1 Estimated fiber temperature profiles plotted against the elapsed time after necking for (a) the minimum draw ratio and (b) a drawing stress of 100 MPa. The estimated fiber temperatures immediately after necking and at 2 ms after necking are shown.

3.4. WAXD patterns

Part of the WAXD images are shown in Fig. 2.2. Only an amorphous halo was observed for the images obtained with negative elapsed time, that is, before necking. The amorphous halo was concentrated to the equatorial direction immediately after necking, and a streak-like diffraction, assigned to the (001′) diffraction of the smectic phase, appeared in the meridional direction after 0.2 ms. With the dissipation of the smectic diffraction, crystal diffractions appeared. The fiber structure development should be almost completed 2.0 ms after necking because the diffraction images are almost the same as those of drawn fibers.
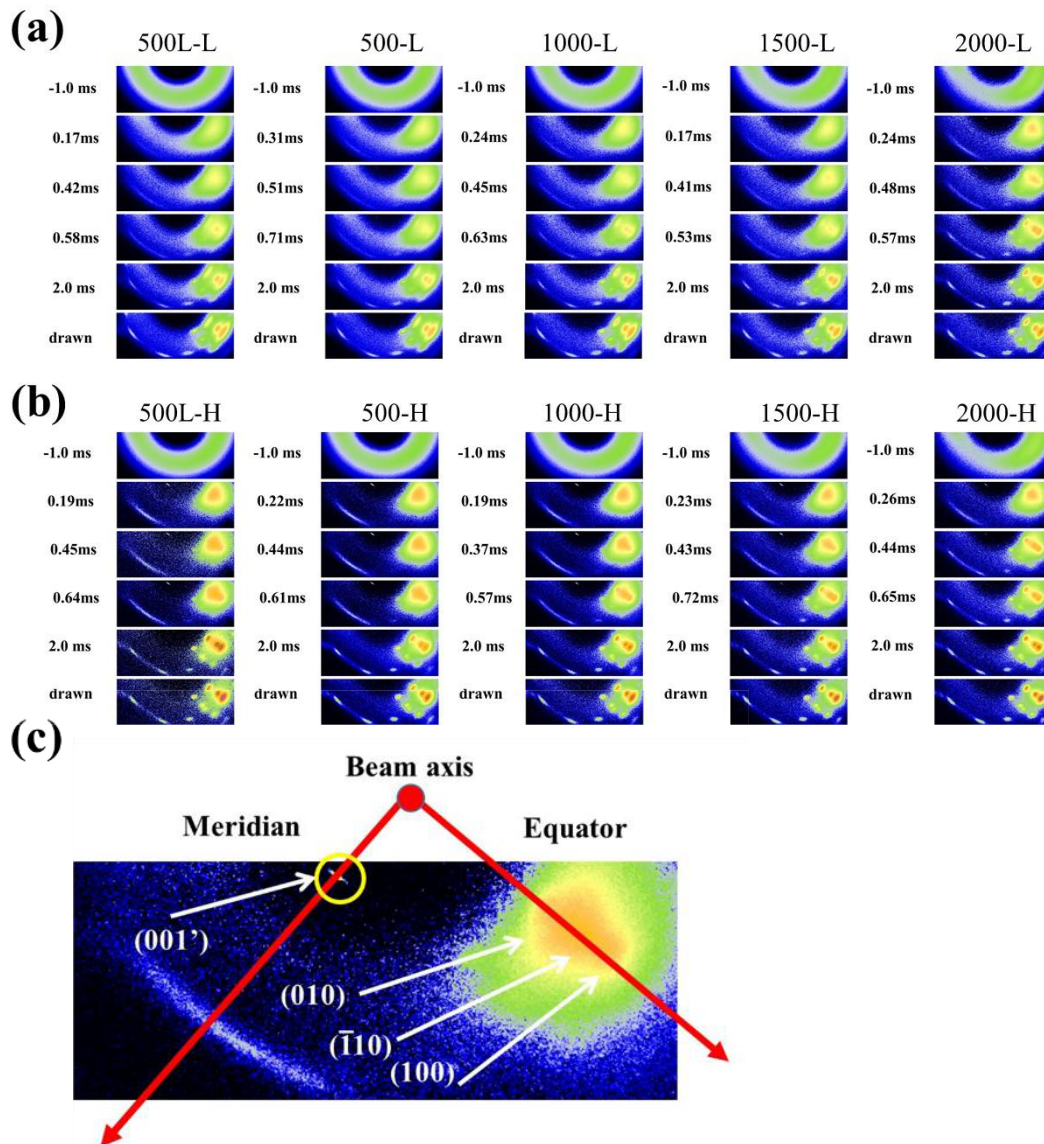
Fig. 2.2 WAXD patterns for the corresponding elapsed time after necking for (a) the minimum draw ratio and (b) a drawing stress of 100 MPa. (c) Enlarged image of sample 500-H 0.61 ms after necking. The equatorial and meridional axes and the (010), (-110), (100) and (001') diffractions are shown.

3.5. Smectic phase

The smectic phase is a metastable structure first reported by Bonart [6], and has also been observed for PEN [7] and PBT [8]. The smectic phase has been formed during batch drawing [9] and heat treatment of oriented amorphous PET [10]. In this study, a strong (001′) diffraction of the smectic phase was observed when the drawing stress was 100 MPa, particularly at low spinning speed. In contrast, a very weak (001′) diffraction was observed that disappeared immediately after necking for fibers drawn at the minimum draw ratio. This fact indicates that necking is not sufficient to form the smectic phase at the minimum draw ratio. Instead, an excessive draw ratio over the minimum draw ratio or an excessive drawing stress over the yield stress seems to be necessary to form the smectic phase. This is because the minimum draw ratio is decided by the NDR of the as-spun fiber, and the NDR is closely related to the yield stress. The excessive stress aligns the molecular chains along the fiber axis, and bundles of the aligned molecular chains should form the smectic phase.

Fig. 2.3 and 2.4 show the meridional integrated intensity and d-spacing of the (001′) diffraction of the fibers, respectively. The d-spacing decreased rapidly, and the diffraction almost disappeared within 0.5 ms after necking for the fiber taken up at 2000 m/min. While the intensity of the (001′) diffraction clearly increased with lower spinning speed, and was able to be observed for a longer time after necking. In particular, the fibers taken up at 500 m/min showed a clear strong (001′) diffraction over 1 ms after necking. Moreover, the laser-spun fiber showed a clear longer time for the decrease of d-spacing. It has been reported that fibers with uniformly distributed entanglements can be obtained by low-speed spinning or laser spinning [11]. Because of the uniform entanglement network in fibers spun at low speed, the drawing stress tends to be applied uniformly to each molecular chain, so more molecular chains are aligned uniformly by the drawing. The uniformly aligned molecular chain should form the highly ordered smectic phase. The smaller applied stress per molecular chain and highly ordered smectic phase can restrict the chain relaxation in the smectic phase, which may cause the longer relaxation time of d-spacing and the longer transition time to the triclinic crystal (see Section 3.6).

The crystallinity and birefringence of drawn fibers were almost the same (Section 3.2). However, the amount of smectic phase and its d-spacing observed immediately after necking showed clear spinning-speed dependence. This is important because the difference in smectic phase can explain the dependence of the properties of drawn fibers on spinning speed. In particular, the tensile and thermomechanical properties of a fiber should be strongly related to the status of the smectic phase because the smectic phase is thought to be bundles of fibrillar molecular chains that bear most of the tensile force in drawn fibers [1]. For example, high-strength drawn fibers can be obtained by taking up fibers at 500 m/min because a large content of the stable smectic phase is formed in the drawing process, which should allow the structure to bear more tensile force. In contrast, the smectic phase should not bear the drawing stress in a fiber taken up at 2000 m/min, in which only a little smectic

phase formed and then vanished immediately. In these PET fibers, the network structure consisting of oriented nuclei formed in the spinning process seems to mainly bear the drawing stress.
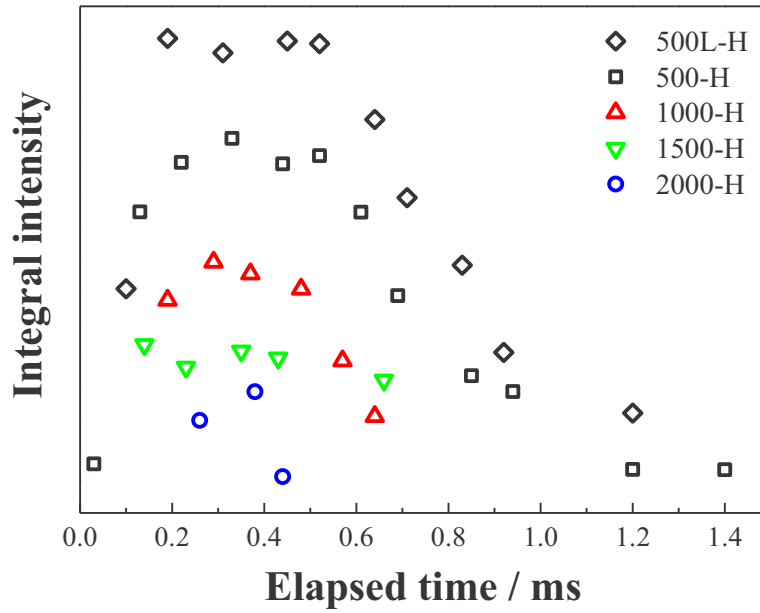
Fig. 2.3 Integrated intensities of the smectic (001') diffraction plotted against the elapsed time after necking. Sample conditions are shown in figure.
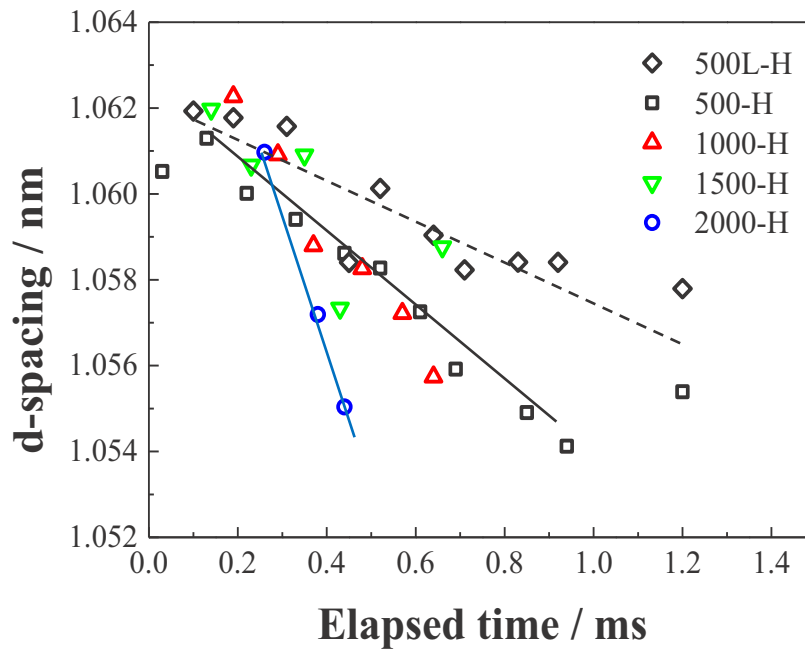
Fig. 2.4 The d-spacings of the smectic (001') diffraction plotted against the elapsed time after necking. Sample conditions are shown in figure.

3.6. Crystallization rate

The intensity profiles along the equatorial directions were obtained from WAXD patterns of the samples and fitted by Gaussian curves(equation 2.1),

$$I(\theta) = I_0 \exp\left\{-4\ln 2 \times \left(\frac{2\theta - 2\theta_0}{\beta}\right)^2\right\}, \tag{2.1}$$

where $2\theta_0$, I_0, and β are the position, intensity, and full width at half-maximum (FWHM) of the peak, respectively. The equatorial intensity profiles could be separated well into the (010), (-110), and (100) crystal diffractions, and a broad peak consistent with an amorphous or smectic phase. Crystallinity index was determined as the fraction of integrated intensity of the crystal diffractions to the total integrated intensity. Crystallinity indices for all samples started to increase from 0.5 ms after necking, and were almost saturated at 2.0 ms (Fig. 2.5). Secondary crystallization should occur after that because all the crystallinity indices for drawn fibers were obviously higher than those of respective fibers 2.0 ms after necking. The crystallization rate K_c, crystallization induction time t_0, and the final crystallinity $X_{c\infty}$ for the fibers were estimated using equation 2.2 with the crystallinity indices until 2.0 ms after necking, and are presented in Fig. 2.6.

$$X_{c(t)} = \left\{1 - K_c \exp\left(t - t_0\right)\right\} X_{c\infty}. \tag{2.2}$$

Fig. 2.5 reveals that measured crystallinity indices were fitted well with equation 2.2. For both types of drawing conditions, the crystallization rate decreased with lowering spinning speed and with laser spinning. The crystallization rates for fibers drawn with a drawing stress of 100 MPa were almost the same as those for fibers obtained with the minimum drawing stress except for the fiber taken up at 2000 m/min, for which a larger crystallization rate was observed for drawing under 100 MPa despite it having the smallest difference in drawing stress and draw ratio between them. All crystallization induction times for the minimum draw ratio were about 0.3 ms, and somewhat longer induction times were observed for the fibers spun at lower speed and drawn under 100 MPa.

Fibers spun at low speed displaying almost no dependence of crystallization rate on drawing stress have been reported previously [3]. It was explained that the crystallization acceleration usually observed with molecular orientation was prevented by the delay of crystallization because of the smectic phase formation. This indicates that the crystallites should originate mainly from the smectic phase for the fibers spun at 500-1500 m/min in this study. The clear dependence of crystallization rate on drawing stress observed for the fibers spun at 2000 m/min can be explained by the absence of the

smectic phase at the beginning of crystallization. The crystallization rate increased with increasing molecular orientation because the crystallization was not restricted by the smectic phase, even at a drawing stress of 100 MPa. The oriented nuclei formed in the as-spun fiber should promote crystallite growth during drawing of this fiber, so it showed the highest crystallization rate despite having the lowest fiber temperature.

For PET/polystyrene (PS) conjugated spun fibers, no crystallization induction time was observed after drawing [2]. The authors suggested that the PET component did not bear the drawing stress; instead the PS component mainly bore it. However, the induction time observed for all fibers in this study was no less than 0.3 ms. It is considered that some structure that specifically bears the stress immediately after necking restricted the molecular motion and delayed the beginning of crystallization. For the fiber taken up at 500 m/min and drawn under 100 MPa, this structure should be the smectic phase. A somewhat longer induction time might indicate the higher stability of this phase. Meanwhile, a molecular network including oriented nuclei mainly bore the stress for the fiber taken up at 2000 m/min.
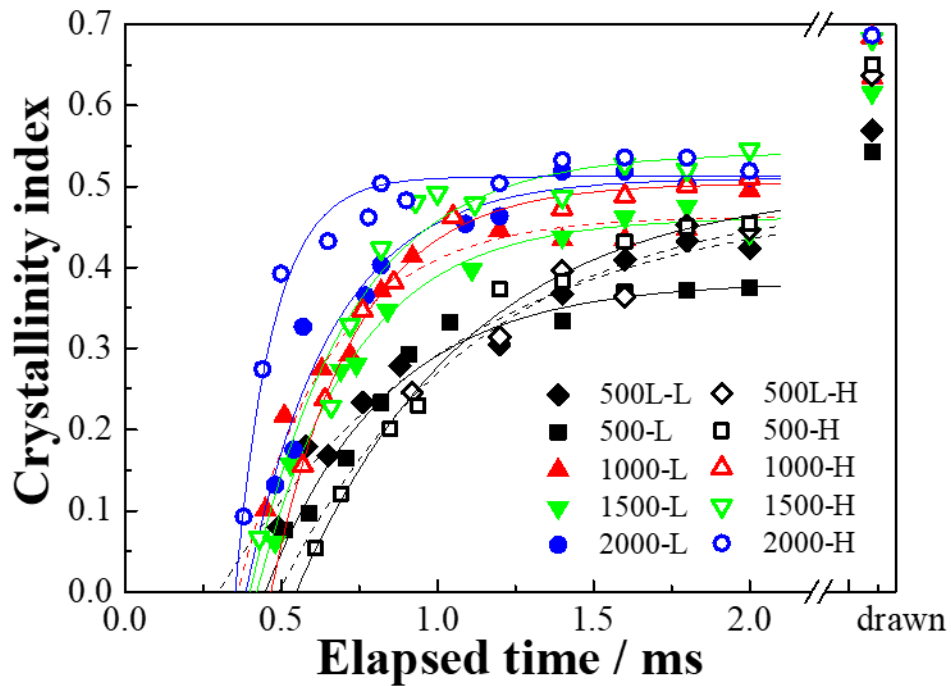
Fig. 2.5 Crystallinity indices estimated from the WAXD equatorial profiles plotted against the elapsed time after necking. Sample conditions are shown in the figure.
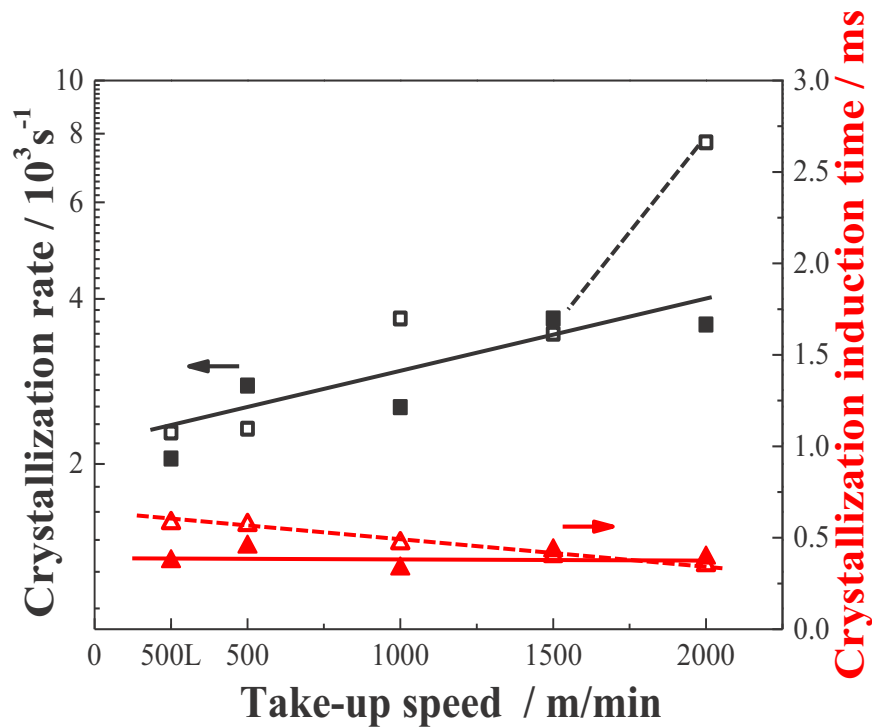

Fig. 2.6 Crystallization rate and crystallization induction time calculated from the crystallinity indices for fibers drawn with the minimum draw ratio (■ and ▲) and at a drawing stress of 100 MPa (□ and △).

3.7. Crystal orientation

By assuming the orientation axis of each PET crystal was tilted in the (−230) plane from the c-axis [12], the tilting angle and crystal orientation factor were calculated from the intensity profile along the azimuthal angle (φ). The (010) and (100) diffractions were considered to be two overlapping peaks symmetrical to the equator, and then the intensity profiles can be expressed by equation 2.3. Each peak was fitted by a Pearson VII type curve, expressed by equation 2.4, with the peak position (φ_P) and a shape factor m of 2. The measured profiles were fitted well with the curves. The crystal orientation factor (f), i.e., the orientation factor of the orientation axis to the fiber axis, was obtained by equation 2.5. The tilting angle (t) was obtained from the peak positions (φ_P) and the d-spacing of (hkl) plane (d_{hkl}) using equation 2.6. The lattice constants used for the calculation were $a = 0.452$ nm, $b = 0.598$ nm, $c = 1.077$ nm, $\alpha = 101°$, $\beta = 118°$, and $\gamma = 111°$; i.e., those reported by Tomashpol'skii et al. [13].

$$I(\varphi) = i(\varphi, \varphi_p) + i(\varphi, -\varphi_p) \tag{2.3}$$

$$i(\varphi, \varphi_p) = \frac{I_0}{\left\{ 1 + 4\left(\frac{\varphi - \varphi_p}{\tau} \right)^2 \left(2^{\frac{1}{m}} - 1 \right) \right\}^m} \tag{2.4}$$

$$f = \frac{3\langle \cos^2 \varphi \rangle - 1}{2}, \quad \langle \cos^2 \varphi \rangle = \frac{\int_0^{\pi/2} i(\varphi, 0) \cos^2 \varphi \sin \varphi \, d\varphi}{\int_0^{\pi/2} i(\varphi, 0) \sin \varphi \, d\varphi} \tag{2.5}$$

$$\cos \varphi_p = d_{hkl} \left[\left(\frac{h}{2} + \frac{k}{3} \right) c \sqrt{\frac{1 - \cos^2 t}{c^2 L - K^2}} + \frac{l}{c} \left(\cos t - K \sqrt{\frac{1 - \cos^2 t}{c^2 L - K^2}} \right) \right] \tag{2.6}$$

Where, $K = \frac{ac}{2} \cos \beta + \frac{bc}{3} \cos \alpha$, $L = \frac{a^2}{4} + \frac{b^2}{9} + \frac{ab}{3} \cos \gamma$

The obtained f and t are shown in Fig. 2.7. There were almost no changes in f and t observed for all samples after the crystal diffraction was clearly detected. With increasing spinning speed for the minimum draw ratio, t decreased while f of the (010) plane increased. These tendencies can be explained by the increase of drawing stress. However, a small t and large f of the (100) plane were also observed for the laser-spun fiber despite it having the lowest drawing stress of the samples. The reason for this is not clear. In contrast, both f and t became saturated for fibers drawn at a drawing stress of 100 MPa at f of over 0.98 and t of less than 3°.
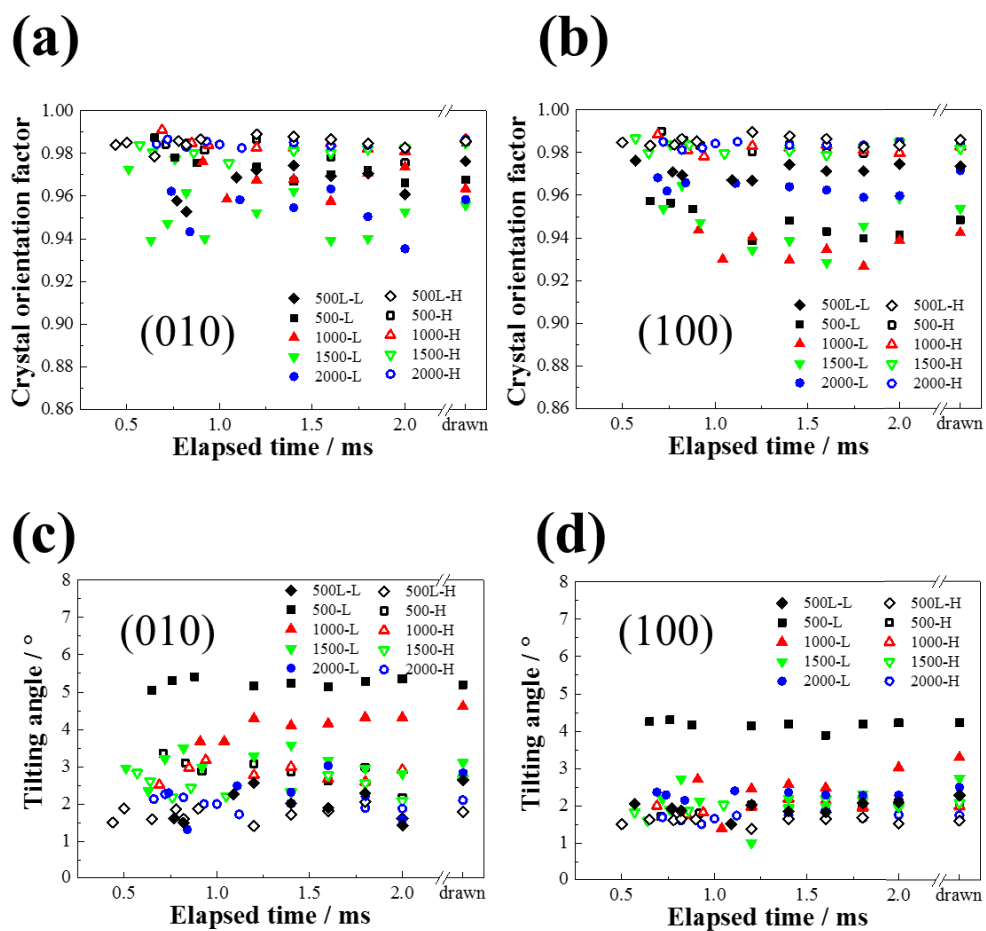
Fig. 2.7 (a, b) Crystal orientation factors and (c, d) tilting angles of the (010) and (100) planes of the fibers. Sample conditions are shown in the figure.

3.8. SAXS patterns

Part of the SAXS images are shown in Fig. 2.8. By drawing at the minimum draw ratio, an X-shaped pattern appeared about 0.3 ms after necking, and then changed to a four-point pattern for all spinning conditions (Fig. 2.8(a)). On the contrary, for a drawing stress of 100 MPa, although the patterns finally became a similar equatorial bar-like pattern, clear spinning condition dependence was observed in the initial stage of structure development (Fig. 2.8(b)). That is, the four-point pattern similar to that found with minimum drawing stress was observed at about 0.3 ms, and it changed to the bar-like pattern, probably because of the overlap of the meridional two-point patterns, as time elapsed for the fiber taken up at 2000 m/min. While a bar-like pattern was already observed at 0.4 ms, it shifted gradually to higher angle for the fibers taken up at 500m/min.

An X pattern was also reported for fibers drawn with the minimum draw ratio, and was explained by the shear-band-like structure formed by necking [3, 14]. The shear-band-like structure should be a molecular bundle aligned along the shear plane. The four-point SAXS pattern can also be explained by the crystallites formed along the shear plane. Incidentally, it has been proposed that an entangled molecular network forms in the as-spun fibers [15]. Therefore, at necking for the minimum draw ratio, the shear deformation is thought to be terminated by the extension of part of the molecular network. Despite the clear dependence of the spinning conditions on drawing stress, the similar structure development for the minimum draw ratio indicates that the molecular bundle aligned along the shear plane does not directly bear the drawing stress and tensile force applied to the drawn fiber. Therefore, there must be force-bearing chains connecting the entanglements in molecular bundles. These force-bearing chains are thought to be a part of the molecular network mentioned above, and the crystallites seemed to be developed from the force-bearing chains. Crystallites surrounded by the molecular bundle involving entanglements was also supposed for nano-oriented crystals [16].

A four-point pattern was observed in the initial stage of structure development for the fibers taken up at 2000 m/min even under a drawing stress of 100 MPa. This indicates that crystallites also formed along the molecular bundle aligned along the shear plane in this case. Thereafter, the gradual pattern change suggests the rearrangement of crystallites along the oriented nuclei formed in the spinning process, which is probably caused by relaxation of the molecular bundle. The crystallites grown from the oriented nuclei seemed to bear most of the drawing stress, whereas the crystallites formed along the shear plane hardly bore any stress. By interlocking the crystallites with large internal differences in borne stress, the thermal shrinkage of obtained fibers is thought to be restricted because the crystallites originally formed along the shear bands block the thermal shrinkage.

(a)

(b)
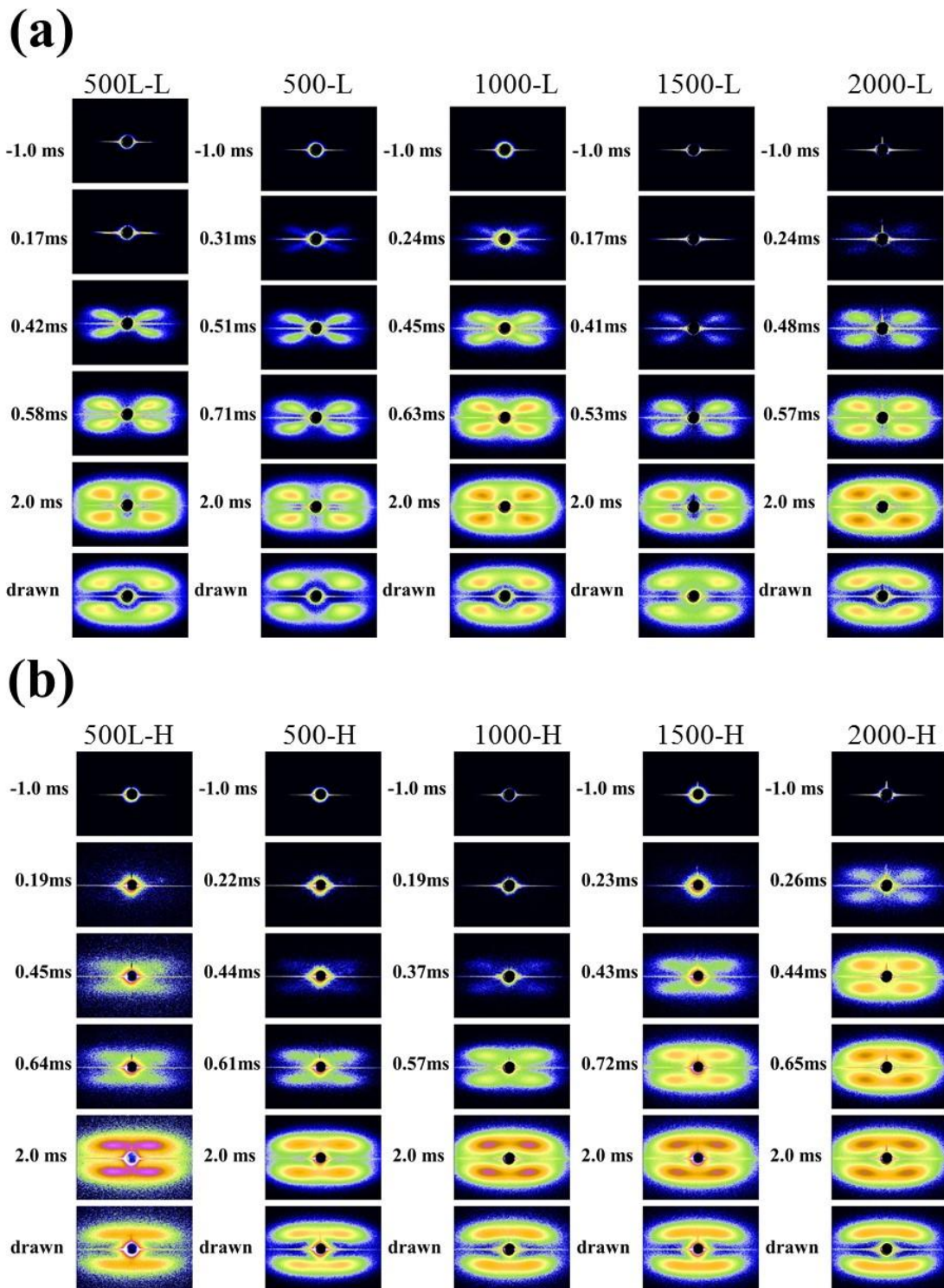
Fig. 2.8 SAXS patterns at different elapsed times for fibers after necking drawn at (a) the minimum draw ratio and (b) a drawing stress of 100 MPa.

3.9. Long period

The long period shown in Fig. 2.9 was calculated by the Bragg formula from the peak position obtained by fitting each meridional SAXS profile with a Gaussian curve and base line. The long period increased with drawing stress. In particular, the larger long period in the initial stage of structure development and a steep decrease until 2.0 ms were observed for the fibers spun at 500 m/min and then drawn under a stress of 100 MPa. In contrast, most crystallites should be formed together with the periodic structure for the other samples because the long period did not change much.

The decrease in the long period and the low crystallization rate observed for the fibers spun at 500 m/min and drawn under a stress of 100 MPa suggest that the crystallites formed gradually from the smectic phase. Yamaguchi et al [1] also observed these phenomena and proposed a model in which the fibrillar smectic phase was transformed into a microfibril structure consisting of a sequence of crystallites and amorphous phases connected by tie chains. Because the smectic phase is thought to be formed mainly by extended polymer chains, numerous taut tie chains bearing the external force should be formed in the amorphous phase. Moreover, the development of bar-like patterns without passing through the four-point pattern indicates that the microfibril developed directly from the aligned molecular bundle formed at necking by way of fibrillar-shaped smectic phase. Therefore, a tightly interlocked structure hardly formed between the fibrils. As a result, fibers possessing high strength but also large thermal shrinkage tend to be formed by the high-ratio drawing of fibers spun at low speed.
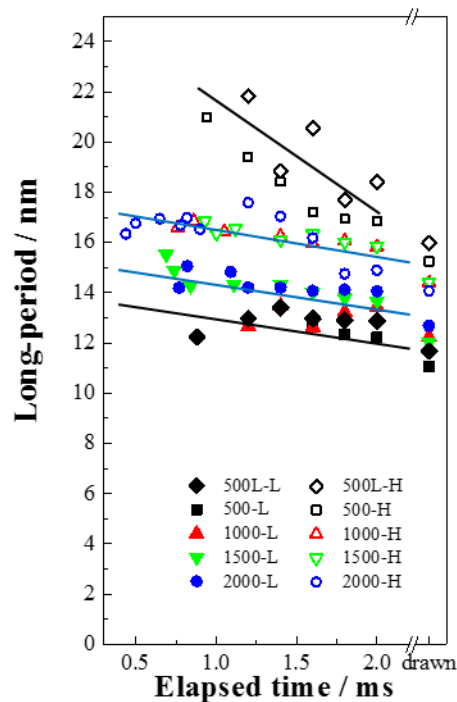

Fig. 2.9 Long periods obtained from SAXS patterns plotted against the elapsed time after necking. Sample conditions are shown in figure.

33

3.10. Effect of spinning conditions on fiber structure development

Schematic diagrams of fiber structure development are shown in Fig. 2.10. By drawing at the minimum stable draw ratio, crystallites appear to be formed along the shear-band-like structure formed by necking. The NDR is influenced by the structural organization [17]. Because the shear deformation caused by necking changes the entangled chain network to a shear-band-like structure with connective chains, the size and orientation of the entangled molecular network formed in the melt-spinning process [11] determines the NDR. Although the X-shaped SAXS pattern was observed for all spinning conditions, the drawing stress increased with the spinning speed. The increase of drawing stress increases the molecular orientation, which raises the crystallization rate and changes the properties of the drawn fiber.

Clear dependence of the structure development on spinning speed was observed for the high-ratio drawing under high drawing stress. The smectic phase should preferentially form in fibers spun at low speed or by laser spinning, while the oriented nuclei formed in the spinning process tend to grow in fibers spun at high speed. By drawing fibers spun at low speed over their NDR, the smectic phase is considered to be oriented chain bundle formed by the excessive drawing of the shear-band-like structure. Because the maximum draw ratio is decided by the entanglement structure in the as-spun fibers, the length and amount of smectic phase should depend on the spinning conditions. Therefore, structure development is typically observed for fibers spun at 500 m/min with a uniform entangled molecular network [11]. Take-up speeds of no more than 1500 m/min are thought to be included in this category of structure development in this study. The maximum draw ratio and amount of smectic phase decreased with increasing spinning speed. Drawing at high strain rate in a high-speed spin line produced a molecular network with nonuniform entanglement density, which caused stress concentration at specific areas, inducing solidification of the fiber through the formation of oriented nuclei in the force-bearing chain. The stress should also be concentrated on the molecular network in the drawing process, and then the crystallites formed by the oriented nuclei seem to grow preferentially in this case. However, the above-mentioned shear-band-like structure was also formed in the fibers taken up at 2000 m/min because they showed clear necking and a four-point SAXS pattern during the initial stage of structure development. The mixture of these two mechanisms might be typical structure development of a POY. The fiber spun at the higher speed, a so-called fully oriented yarn, should be another extreme model of the fiber structure development. Because orientation-induced crystallization proceeded on the spin line, the as-spun fiber was mainly composed of the crystallites formed in the spin line [18]. Stable neck drawing is no longer possible in this case because of the dissipation of the natural drawing region.
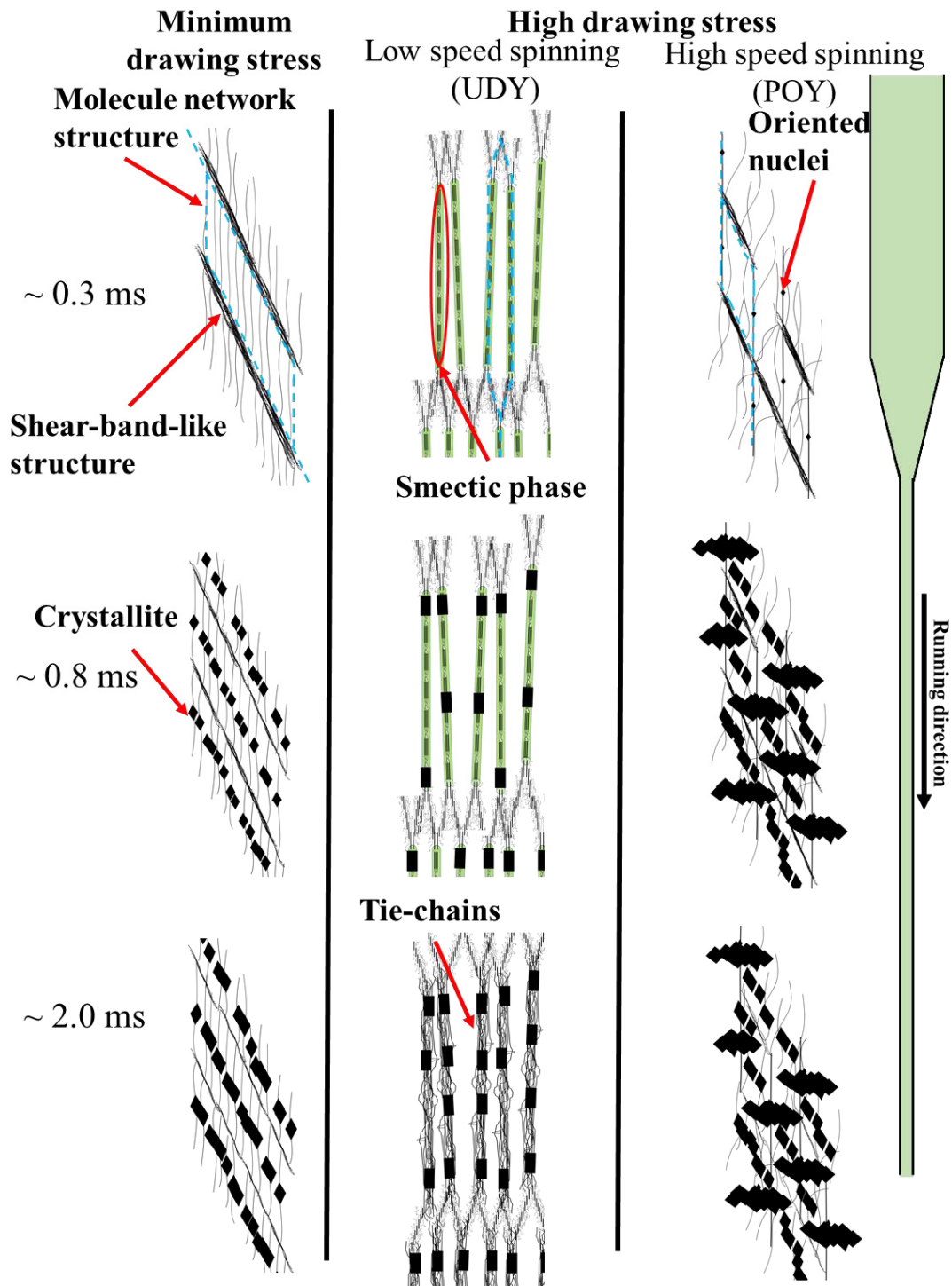
Minimum drawing stress
Molecule network structure

~ 0.3 ms

Shear-band-like structure

Crystallite
~ 0.8 ms

~ 2.0 ms

High drawing stress
Low speed spinning (UDY)

Smectic phase

Tie-chains

High speed spinning (POY)
Oriented nuclei

Running direction

Fig. 2.10 Schematic diagram of fiber structure development. The structures of the molecular network in the fibers are shown as blue lines.

35

4. Conclusions

The effects of spinning conditions on the structure development of PET fibers after necking were analyzed by WAXD/SAXS measurements. Fibers obtained with a spinning speed of 500–2000 m/min were used for the measurements. The fibers obtained from laser spinning using a CO_2 laser beam irradiated onto the fiber at the melt spinning line were also analyzed. The as-spun fibers were drawn continuously at the minimum stable draw ratio and under a drawing stress of about 100 MPa. The latter was almost the maximum drawing stress at which all the as-spun fibers could be drawn stably. The WAXD and SAXS images were captured simultaneously until 2.0 ms after necking using synchrotron radiation. The time resolution of the measurements was 0.09–0.18 ms.

An X-shaped SAXS pattern was observed about 0.3 ms after necking for all fibers drawn at the minimum stable draw ratio. This indicates that necking, which determines the minimum stable draw ratio, decided the fiber structure development.

In contrast, clear dependence of the structure development on spinning speed was observed for fibers drawn under a drawing stress of 100 MPa. A strong smectic (001′) diffraction and larger long period, particularly less than 1 ms after necking, were observed for the fibers spun at 500–1500 m/min, while almost no smectic phase was observed at the beginning of crystallization for that spun at 2000 m/min. A higher crystallization rate and clear draw ratio dependence of crystallization rate were also observed for the fiber spun at 2000 m/min despite it having the lowest fiber temperature and smallest difference in drawing stress of the fibers investigated.

These results suggest the crystallites were mainly formed by the phase separation of the fibrillar smectic phase for the fibers spun at 500–1500 m/min, while they mainly developed from the oriented nuclei formed in the spinning process for the fibers spun at 2000 m/min. Although no marked differences of birefringence, crystallinity, and SAXS patterns were observed for the drawn fibers, there were clear differences in their tensile strength and thermal shrinkage behavior. The clear differences in structure development described above indicate the capability of structure development analysis to aid in designing fiber properties.

References

1) T. Yamaguchi, K. H. Kim, T. Murata, M. Koide, S. Hitoosa, H. Urakawa, Y. Ohkoshi, Y. Gotoh, M. Nagura, M. Kotera, K. Kajiwara, *J. Polym. Sci., Polym. Phys.*, 46, (2008), 2126-2142.

2) K. Sugawara, T. Ikaga, K.H. Kim, Y. Ohkoshi, K. Okada, H. Masunaga, T. Kanaya, M. Masuda, Y. Maeda, *Polymer*, 79, (2015), 37-46.

3) R. Tomisawa, T. Ikaga, K.H. Kim, Y. Ohkoshi, K. Okada, H. Masunaga, T. Kanaya, M. Masuda, Y. Maeda, *Polymer*, 116, (2017), 357-366.

4) W. Okumura, T. Yamaguchi, Y. Ohkoshi, Y. Gotoh, M. Nagura, *Intern. Polym. Proc.*, 17, (2002), 124-132.

5) S.Kase, and T.Matsuo, *J. Polym. Sci. Part A*, 3, 2541, (1965)

6) R. Bonart, Kolloid-Z, 213, (1966), 1-11.

7) K. H. Kim, R. Aida, Y. A. Kang, T. Ikaga, Y. Ohkoshi, I. Wataoka, H. Urakawa, *Polymer*, 53, (2012), 4272-4279.

8) T. Konishi, Y. Miyamoto, *Polymer*, 42, (2010), 349-353.

9) D. Kawakami, B. S. Hsiao, C. Burger, S. Ran, C. Avila-Orta, I. Sics, T. Kikutani, B. Chu, *Macromolecules*, 38, (2005), 91-103.

10) T. Asano, F. J. Balta Calleja, A. Flores, M. Tanigaki, M. Mina, C. Sawatari, H. Itagaki, H. Takahashi, I. Hatta, *Polymer*, 40, (1999), 6475-6484.

11) M. Masuda, Y. Funatsu, K. Kazama, T. Kikutani, *Sen'i Gakkaishi*, 60, (2004), 338-345.

12) R. P. Daubeny, C. W. Bunn, *J. Polym. Sci., Polym. Chem*. 226, (1954), A1954, 531.

13) Y. Y. Tomashpol'skii, G. S. Markova, *Polym. Sci. USSR*, 6, (1964), 316-324.

14) K. Okada, M. Nakada, Y. Higashioji, K. Takahashi, Y. Ohkoshi, T. Kanaya, *Koubunshi Ronbunshu*, 71, (2014), 593-600.

15) T. Kikutani et al. "*Fundamental and Practical Technologies for Nano-structured Polymeric Materials*", 2008, p.56-110, CMC press, ISBN978-4-7813-0043-6.

16) K. N. Okada, J. Washiyama, K. Watanabe, S. Sasaki, H. Masunaga, M. Hikosaka, *Polymer*, 42, (2010), 464-473.

17) M. Kuriyagawa, K. Nitta, *Polymer*, 52, (2011), 3469-3477.

18) J. Shimizu, T. Kikutani, A. Takaku, N. Okui, *Sen'i Gakkaishi*, 40, (1984), T177-183.

Chapter 3

Effect of draw ratio on fiber structure development of polyethylene terephthalate

Chapter 3: Effect of draw ratio on fiber structure development of polyethylene terephthalate

1. Introduction

In this Chapter, the effects of the draw ratio on the fiber structure development of polyethylene terephthalate after continuous neck-drawing were investigated using simultaneous WAXD/SAXS measurements. Specifically, we tried to explain the draw ratio dependence of the tensile strength and thermal shrinkage stress by the changes in structural parameters with the fiber structure development, i.e., the amount and d-spacing of the smectic $(001')$ diffraction, and the long period obtained by the SAXS images.

2. Experimental

2.1. Sample

The fibers used for drawing were prepared by melt-spinning PET (IV = 1.3 dL/g) provided by the Toray Co. The polymer was heated at 310 °C, extruded from a one-hole nozzle at a mass flow rate of 4.8 g/min, and taken-up at 500 m/min. The nozzle diameter was 1.0 mm, and the length/diameter ratio was 3.

2.2. Drawing

The drawing system used has been described in a previous report [1]. Fibers were fed continuously from a feed roller, heated by irradiation with a CO_2 laser beam, and drawn based on the speed difference between the feed and take-up rollers. The fiber running speed after necking was fixed at 110 m/min, and the draw ratio was changed by changing the fiber-feeding speed. A random polarized laser beam of wavelength and diameter 10.6 μm and 6 mm, respectively, was generated using a PIN-30R laser (Onizuka Glass Co., Ltd.). The beam was used to irradiate running fibers from three different directions. The drawing tension was measured using a tension meter (HS-1500S, Eiko Sokki Co., Ltd.) A 100 gf pickup was installed between the neck-drawing point and the take-up roller. The drawing stress was calculated from the drawing tension and the diameter of the drawn fiber. The drawing conditions are shown in Table 1. The range of draw ratios, 3.0–4.5, was the range for stable neck-drawing during more than 5 min, i.e., the neck-drawing point was not stable at a draw ratio less than 3.0, and the fiber was liable to break at a draw ratio above 4.5. The minimum draw ratio of 3.0 was almost equal to the natural draw ratio (NDR) estimated from the stress–strain curve for the as-spun fibers. The laser power for each drawing condition was determined to enable fluctuations in the neck-drawing point to be minimized.

2.3. On-line measurements

Method of on-line measurement and calculation of time resolution are the same as section 2.3 of Chapter 2. In Chapter 3, the fluctuations of the necking point of 0.09–0.14 mm, the width of the necking point of 0.13–0.28 mm, and the width of the X-ray beam of 0.05 mm were used for calculation. Then, the obtained time resolution was 0.09–0.16 ms.

For the X-ray analysis, calculation of proportion and d-spasing of smectic phase, crystallinity index, crystallization rate, crystallization induction time, crystal orientation factor, tilting angle and long-period are the same as Chapter 2.

2.4. Birefringence

Refer to section 2.4 of Chapter 2.

2.5. Thermomechanical tests

Refer to section 2.5 of Chapter 2.

3. Results and discussion

3.1. Structure and properties of drawn fibers

The structure and properties of the drawn fibers are listed in Tables 3.1 and 3.2. The crystallinity was determined using DSC, based on a heat of fusion of 135 kJ/kg [3]. The birefringence and crystallinity of the drawn fibers increased with increasing draw ratio but seemed to reach a maximum value at a draw ratio above 4.2. The properties of the drawn fibers also changed with changes in the draw ratio; the tensile strength, Young's modulus, thermal shrinkage factor, maximum thermal shrinkage stress, and temperature of maximum shrinkage increased, whereas the elongation decreased, with increasing draw ratio. However, there were some differences at draw ratios greater than 4.2. The Young's modulus and shrinkage factor seemed to reach a maximum value above a draw ratio of 4.2, whereas the tensile strength, elongation, and shrinkage stress continue to change. These results indicate that the effect of draw ratio on the fiber structure changed at a draw ratio of 4.2. We therefore focused on the difference between the draw ratio dependence of the fiber structure development at draw ratios below and above 4.2.

Table 3.1 Drawing conditions and structural parameters of drawn fibers.

Draw ratio	Laser power /W	Drawing stress / MPa	Birefringence x10³	Crystallinity / %
as-spun	-	-	4	12
3.0	18	22	118	27
3.3	19	29	151	34
4.2	22	103	182	42
4.5	25	149	198	38

**Table 3.2** Mechanical and thermomechanical properties of drawn fibers.

| Draw ratio	Young's modulus / GPa	Tensile strength / MPa	Elongation / %	Shrinkage at 200°C / %	Maximum shrinkage stress	
					Stress / MPa	Temperature /°C
as-spun	2.2	175	616	-	-	-
3	7.6	582	95	5	17	101
3.3	9.4	629	69	7	30	117
4.2	12.6	916	38	9	72	180
4.5	12.3	1030	27	8	78	194

3.2. Fiber temperature profiles

The fiber temperature profile around the neck-drawing point was determined using a forward difference method, based on the energy balance equation, with consideration of the laser irradiation energy, heat transfer from the fiber surface, work of plastic deformation by an external force, and latent heat of crystallization [11]. The absorption coefficient of PET, $1.149 \times 10^4 \, \mathrm{m^{-1}}$, obtained for the laser beam wavelength was used to calculate the laser irradiation energy [4]. The heat transfer coefficient was estimated experimentally using the equation proposed by Kase and Matsuo [5]. The heat of crystallization and the heat of fusion of the drawn fibers were determined using DSC.

Fig. 3.1(a) shows plots of the estimated fiber temperature against the distance from the laser beam axis. The fiber temperature began to rise at −3 mm, when the laser beam began to irradiate the fibers. Fiber necking occurred when the fiber temperature was near the glass-transition temperature. The fiber temperature increased steeply as a result of the heat of plastic deformation at the necking, continued to increase by the heat of laser irradiation and the latent heat of crystallization, and reached a maximum at the edge of the laser beam (+3 mm). The fiber temperature then decreased to room temperature by heat transfer. Necking occurred at almost the same temperature for all draw ratios. This is because the increase in the laser power and the decrease in the fiber running speed before necking are cancelled by the upstream shift of the necking. In contrast, the steep increase in the fiber temperature at necking increased with increasing draw ratio because of the increase in applied work at necking. The maximum fiber temperature also increased with increasing draw ratio. In particular, for a draw ratio from 4.2 to 4.5, in spite of the small difference in the draw ratio, the temperature increased greatly because of the large increase in the drawing stress. In Fig. 3.1(b), the horizontal axis is converted to elapsed time after necking. As discussed below, the fiber structure mainly developed in the 2 ms after necking. The temperatures at 0 and 2 ms after necking are shown in Table 3.
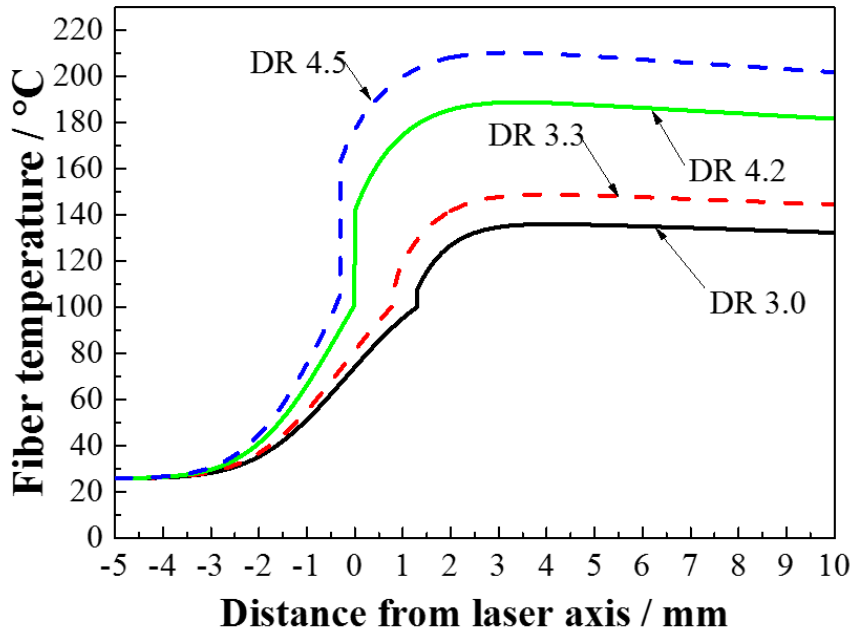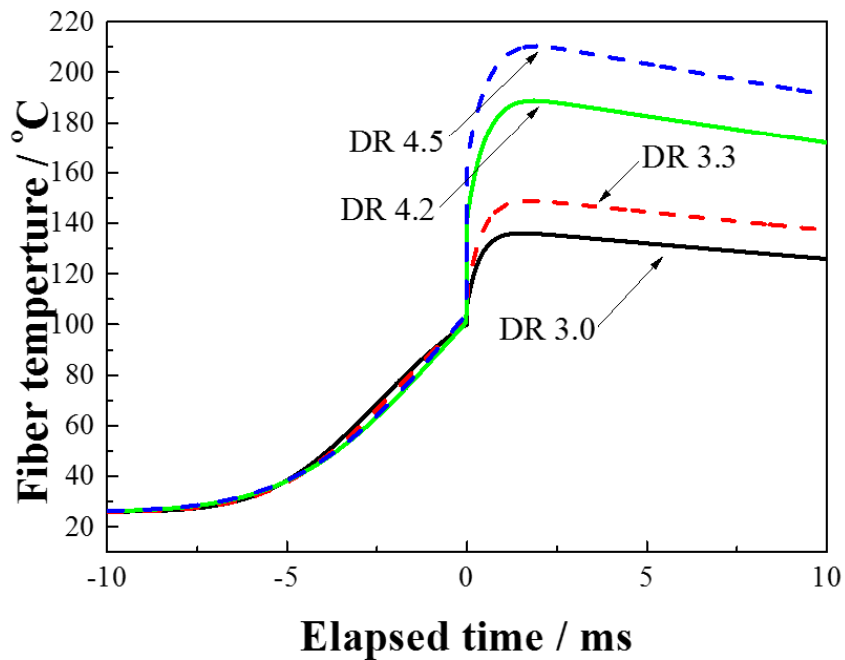
Fig. 3.1 Estimated fiber temperatures plotted against (a) elapsed time after necking and (b) distance against necking point. Draw ratios (DR) are shown in the figure.

3.3. WAXD image

The WAXD images are shown in Fig. 3.2. The elapsed times after necking are noted in the figure. In particular, for a higher draw ratio, a sharp meridional diffraction with a long streak along the layer line was observed at around 0.3 ms after necking. This is the (001′) diffraction of the smectic phase, which is a metastable structure formed during batch drawing [6] or heat-treatment of an oriented amorphous material [7]. The smectic phase was first reported by Bonart [8], and has also been reported for poly(ethylene naphthalate) [9] and poly(butylene terephthalate) [10]. After 0.5 ms, the intensity of the (001′) diffraction started to decrease and an equatorial broad peak separated into the (010), (–110), and (100) crystal diffractions. The stronger and sharper equatorial diffractions observed for the fibers drawn 4.2 and 4.5 times than for those drawn 3.0 and 3.3 times suggest a higher crystallinity and higher crystal orientation of the former than of the latter. However, there were no clear differences between the crystallinities and crystal orientations observed for the fiber drawn 4.2 times and that drawn 4.5 times.
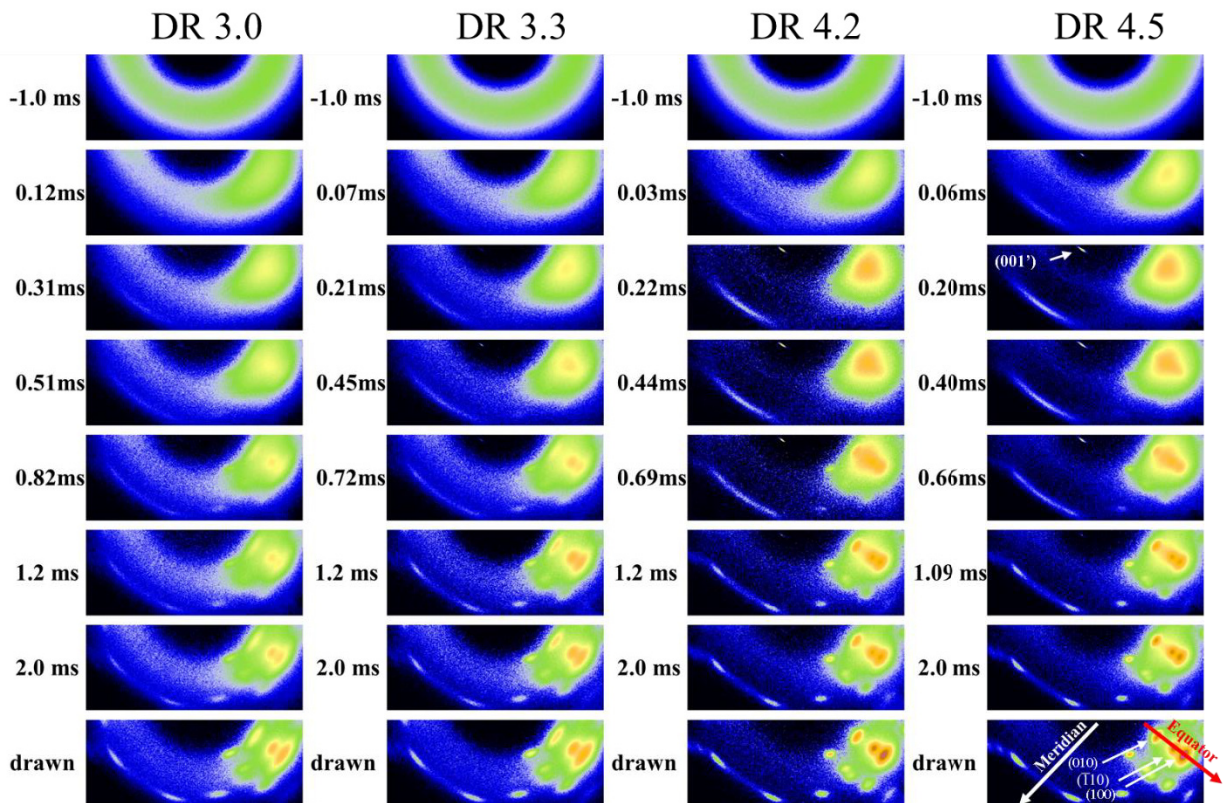

Fig. 3.2 Wide-angle X-ray diffraction patterns at corresponding elapsed times after necking. Draw ratios (DR) are shown.
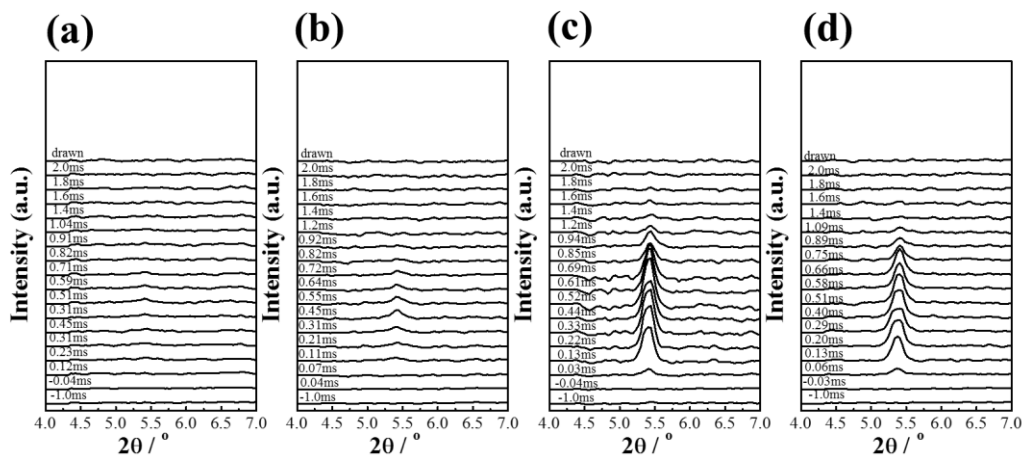
Fig. 3.3 Meridional X-ray intensity profiles at draw ratios (a) DR 3.0, (b) DR 3.3, (c) DR 4.2, and (d) DR 4.5.

3.4. Smectic phase

The meridional intensity profiles obtained from Fig. 3.2 are shown in Fig. 3.3. A sharp smectic (001′) diffraction was observed at a diffraction angle of 5.4°. The integral intensity and the d-spacing are shown in Fig. 3.4 and 3.5, respectively. The intensity reached a maximum at about 0.3 ms, and then decreased. The intensity clearly increased with increasing draw ratio from 3.0 to 4.2, and the diffraction could be observed for a longer time after necking. In contrast, the intensity did not increase but the d-spacing increased with increasing draw ratio from 4.2 to 4.5. Because the d-spacing for a draw ratio of 4.5 was close to the length of the chemical repeating unit, 1.077 nm [11], the smectic phase seems to be composed of almost fully extended chains. The larger d-spacing is caused by the higher drawing stress applied to the smectic phase. A larger stress is also applied to the molecular network including the smectic phases, and extends the molecular chains connecting the smectic phases.

Yamaguchi et al. reported that the d-spacing increases with increasing draw ratio, but no clear dependence of the intensity on the draw ratio was reported [1]. This phenomenon could be explained by the insufficient time resolution of the measurements. Because of the restriction of their light source generated by a bending magnet system, the time resolution of their measurements was no less than 0.6 ms. The light source generated by the undulator-equipped system used in this study had an intensity 10^4 times that of a bending magnet system [11]. It gave a shorter resolution time of about 0.1 ms and images with improved signal/noise ratios, which enabled a more quantitative evaluation of the draw ratio dependence of the (001′) intensity. Sugawara et al. also used an undulator-equipped system and reported that the intensity increased with increasing draw ratio, but there was no obvious change in the d-spacing [20]. The results of this work suggest that an increase in the d-spacing is only observed at high draw ratios, at which the amount of smectic phase is saturated.

A clear decreasing trend in the d-spacing was also observed for a draw ratio of 4.5. Kawakami et. al. [6] reported the increase of d-spacing before the phase transition from smectic phase to crystal. The opposite tendency is caused by the difference of drawing conditions, i. e. batch drawing and continuous drawing. For batch drawing, smectic phase was formed with the increase of molecular orientation. While for continuous drawing in this study, it was formed after necking. The d-spacing decrease is accompanied by emission of stored energy. Kim et. al. [12] observed the delayed emission of stored energy 0.6 ms after necking by measuring the fiber temperature profiles, i.e., part of work of the external force applied at the necking is stored elastically in the smectic phase, and emitted by the relaxation that is indicated by the d-spacing shrinkage. The relaxation is accompanied by transformation of the smectic phase to the triclinic crystal.
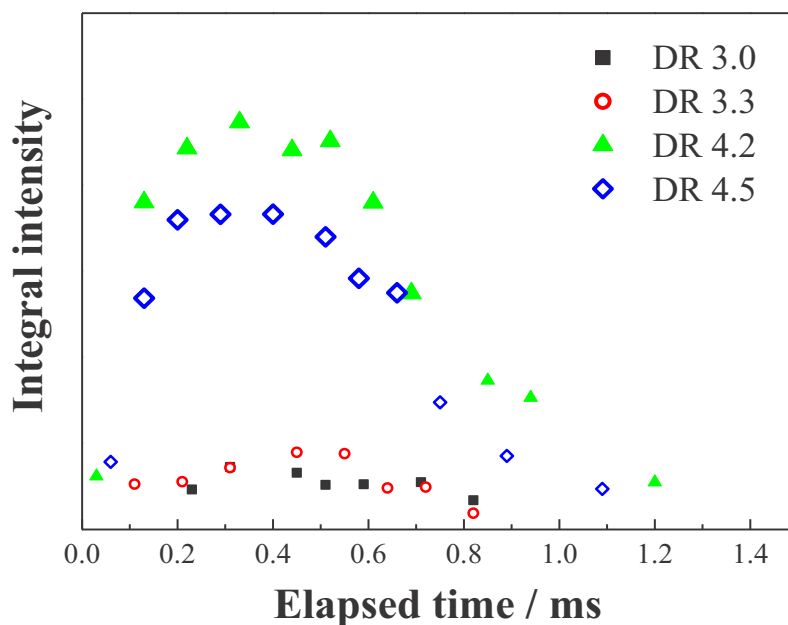
Fig. 3.4 Integrated intensities of smectic (001') diffractions plotted against elapsed time after necking. Draw ratios (DR) are shown in figure. Small plots indicate lower diffraction intensities and are less reliable.
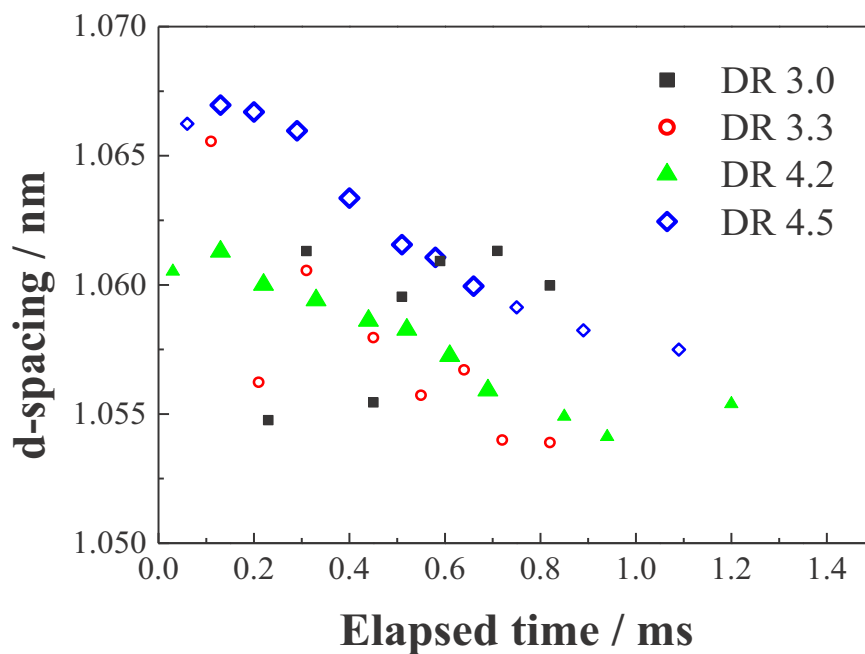
Fig. 3.5 Plots of (001') diffraction *d*-spacings against elapsed time after necking. Draw ratios (DR) are shown in figure. Small plots indicate lower diffraction intensities, as in Fig. 4.

3.5. Crystallization

The crystallinity indices for all the samples started to increase from 0.5 ms after necking, and were almost saturated at 2.0 ms (Fig. 3.6). However, because they are clearly lower than those of drawn fibers, secondary crystallization should be occurred after 2.0 ms. The crystallization rate K_c, crystallization induction time t_0, and final crystallinity $X_{c\infty}$ were estimated using equation 2.2, based on the crystallinity indices up to 2.0 ms after necking; the values are listed in Table 3.3.

The $X_{c\infty}$ value increased with increasing draw ratio up to 4.2, in agreement with the trend in the crystallinities of the drawn fibers. In contrast, there were no clear draw ratio dependences at crystallization rates of 2.3–2.8 ms^{-1} and crystallization induction times of 0.4–0.6 ms. Yamaguchi et al. [1] and Sugawara et al. [2] observed similar crystallization behaviors during continuous drawing of PET, and a K_c of 0.7 ms^{-1} and t_0 of 0.6 ms were reported by the former [1]. The lower crystallization rate than the result in this study should be caused by pattern smearing at an insufficient time resolution. The crystallization rates and crystallization induction times obtained in this study are more reliable because the time resolution of 0.1 ms was sufficiently shorter than the crystallization time. It is worth noting that there were no obvious differences among the crystallization rates obtained at different draw ratios in spite of the clear difference in molecular orientation. A higher molecular orientation generally caused an increase in the crystallization rate. The crystallization rate should also increase with increasing fiber temperature for the temperature range estimated at 3.2. Therefore, the almost constant crystallization rate observed in this work indicates that orientation-induced crystallization should be suppressed at high draw ratios, probably by formation of the smectic phase. The crystallization rate seems to be reduced by the decrease in the free energy change for crystallization via a metastable smectic phase compared with that for direct crystallization from the oriented amorphous phase, i.e., crystallization seems to be suppressed by the decreased molecular mobility in the smectic phase compared with the amorphous phase.

Table 3.3 Crystallization behavior.

Draw Ratio	Fiber Temperature / °C		$X_{c\infty}$ / %	t_0 / ms	K_c / 10^3 s^{-1}
	0 ms	2 ms			
3.0	108	136	37	0.5	2.8
3.3	112	157	41	0.4	2.4
4.2	142	189	45	0.6	2.3
4.5	165	210	48	0.5	2.5
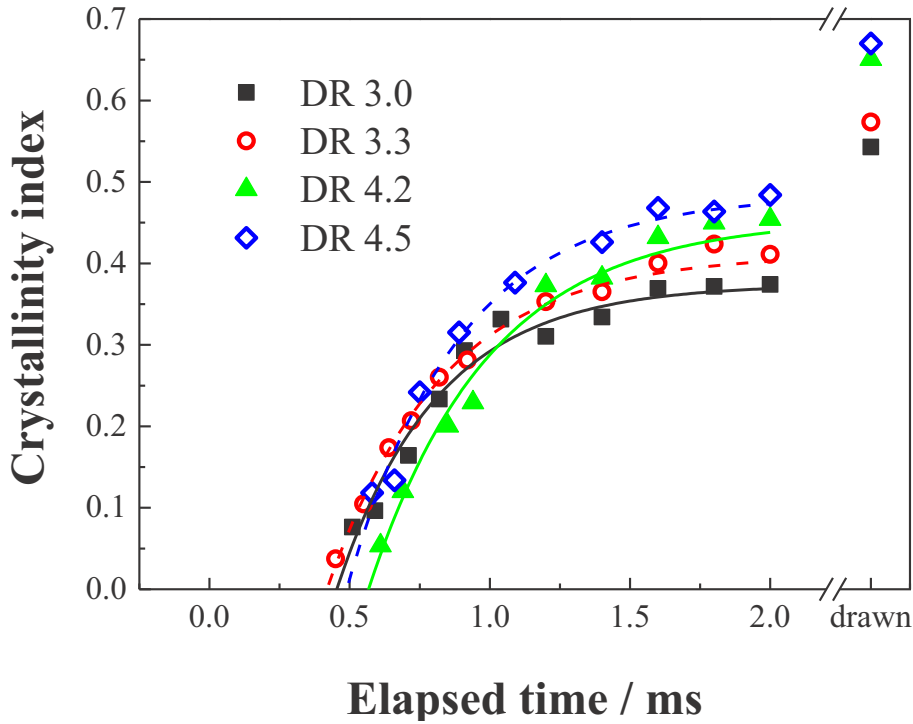
Fig. 3.6 Crystallinity indices estimated from wide-angle X-ray diffraction equatorial profiles plotted against elapsed time after necking. Draw ratios (DR) are shown in figure.

3.6. Crystal orientation factor and tilting angle

By assuming the orientation axis of PET crystal is tilted in the (−230) plane from the *c*-axis [13], the tilting angle and crystal orientation factor were calculated from the intensity profile along the azimuthal angle (φ). The crystal orientation factors and tilting angles are shown in Fig. 3.7 and 3.8, respectively. The crystal orientation factor increased, whereas the tilting angle decreased, with increasing draw ratio up to 4.2. This trend corresponds to increases in the drawing stress and birefringence. In contrast, from a draw ratio of 4.2 to 4.5, although the tilting angle continuously decreased, the crystal orientation factor was almost saturated. The saturation of the crystal orientation corresponds to that of birefringence, and the continuous decrease in the tilting angle corresponds to the increase in the smectic *d*-spacing, as described in section 3.4, by the increase in the drawing stress.

For draw ratios of 3.0 and 3.3, both the crystal orientation factor and tilting angle for the (100) diffraction increased after 2 ms. The simultaneous increases in the crystal orientation factor and tilting angle suggest the formation of lamellar crystals by secondary crystallization. In contrast, for draw ratios of 4.2 and 4.5, neither the crystal orientation factor nor the tilting angle changed after 2 ms. This indicates that secondary crystallization mainly occurred in fibrils.
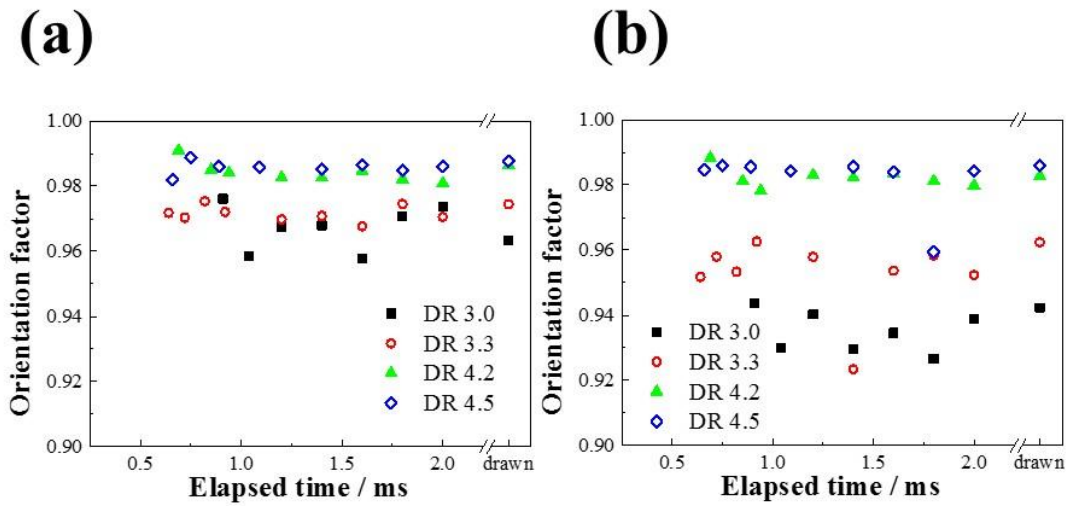
Fig. 3.7 Orientation factors of crystal *c*-axis estimated from (a) (010) and (b) (100) diffractions plotted against elapsed time after necking. Draw ratios (DR) are shown in figure.

Fig. 3.8 Tilting angles of crystal *c*-axis estimated from (a) (010) and (b) (100) diffractions plotted against elapsed time after necking. Draw ratios (DR) are shown in figure.
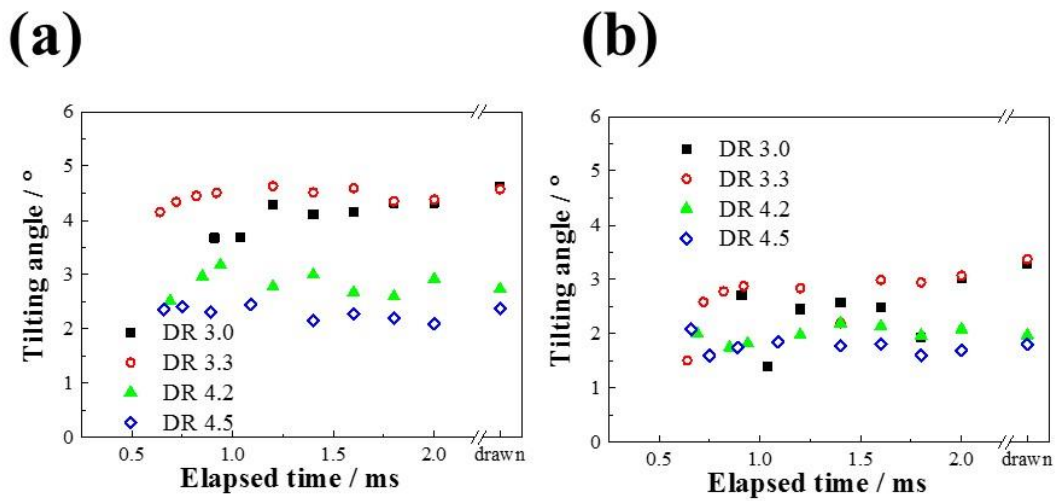
3.7. SAXS image

Fig. 3.9 shows SAXS images. The scattering intensities increased with time elapsed for all draw ratios. For draw ratios of 3.0 and 3.3, the X-shaped scattering pattern observed at 0.2-0.3 ms changed to a four-point pattern 0.8 ms after necking. In contrast, for draw ratio of 4.2 and 4.5, the X-pattern was not observed, but a meridional two-point pattern overwrapped with a four-point pattern appeared directly at 0.4-0.5 ms after necking instead.

The X-patterns observed for the lower draw ratios were also observed for high-speed-spun PET fiber [15, 16]. It was explained by the series of crystallites aligned to the direction tilted to the fiber axis. Okada et al. observed changes in the SAXS image of an axial-planar-oriented PET film obtained by continuous uniaxial drawing. A two-point pattern was observed in the through-view images, whereas X-like patterns were observed in the edge-view images [17]. This suggests that the density difference along the shear-band-like structure [18] should be developed by compression along the film thickness. The shear deformation seemed to be occurred along the surface of the benzene ring because the surface oriented along the normal of film by the deformation. The X-patterns observed in this study thought to be caused by the similar shear deformation at necking. By forming crystallites along the structure, the X-pattern changed to a four-point pattern.

The long periods obtained from the meridional intensity profiles are shown in Fig. 3.10. The long periods at draw ratios of 4.2 and 4.5 were clearly higher than those at draw ratios of 3.0 and 3.3. In addition, the long periods at higher draw ratios decreased significantly up to 1.0 ms. The decrease in the long period with decreasing smectic (001′) intensity suggests that the new crystallites were formed and developed in the smectic phase. This agrees with the model proposed by Yamaguchi et al. that the fibrillar smectic phase was divided into a sequence of crystallites and amorphous phases including tie molecules [1].
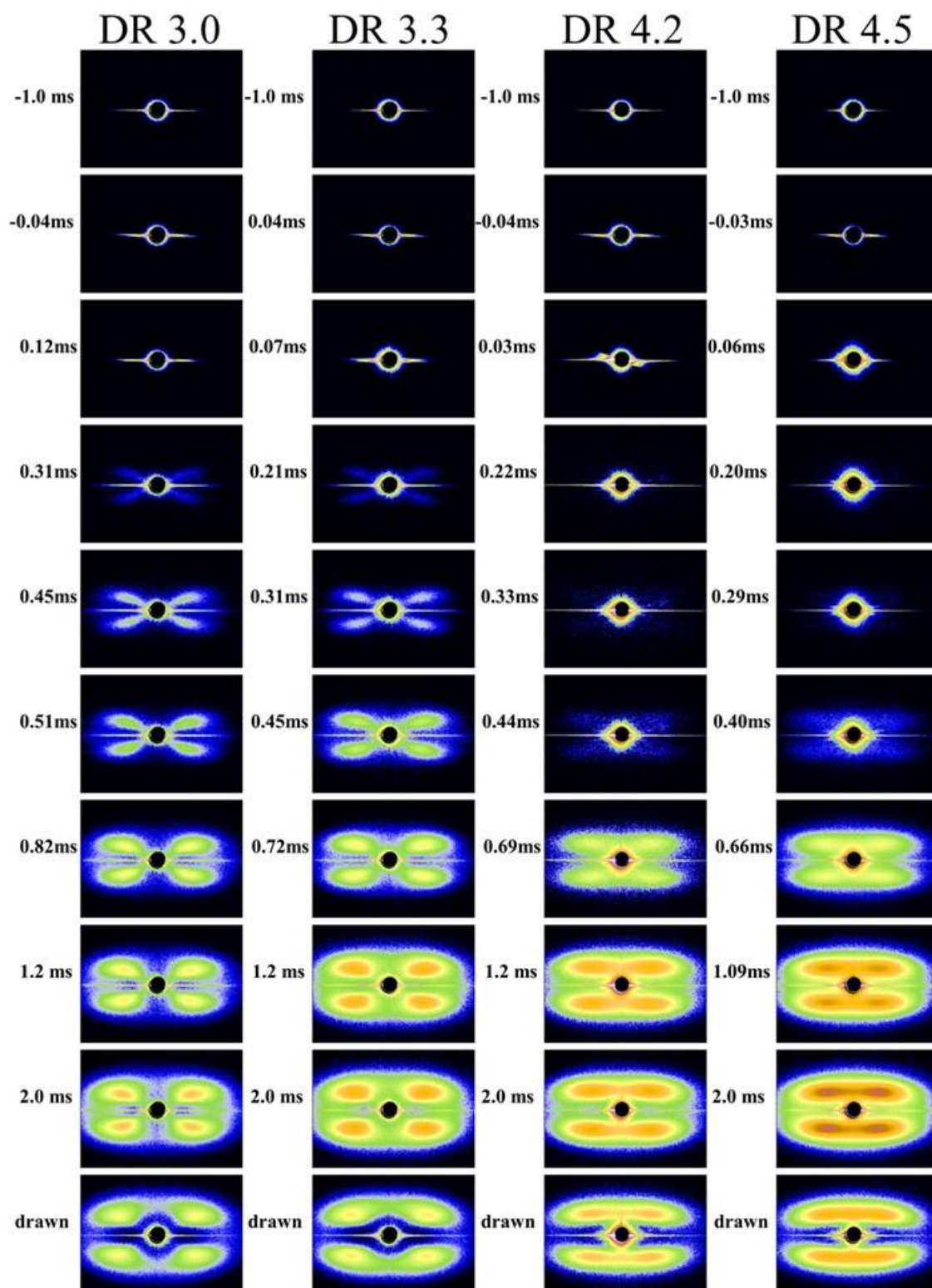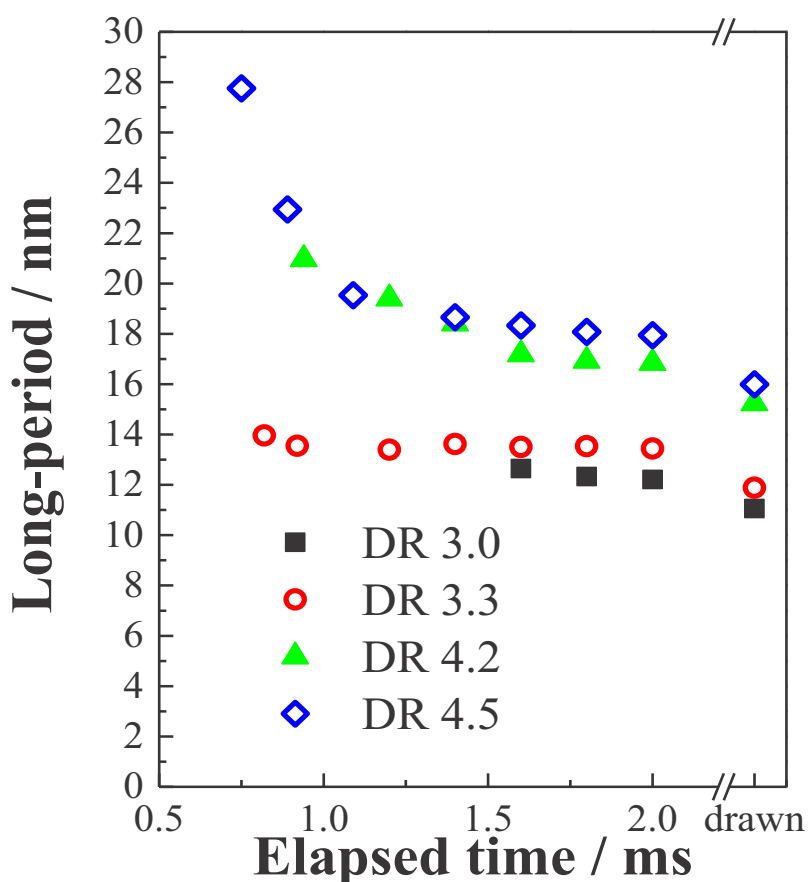
Fig. 3.9 SAXS patterns for corresponding elapsed times after necking. Draw ratios (DR) are shown in the figure.

Fig. 3.10 Long periods obtained from SAXS patterns plotted against elapsed time after necking. Draw ratios (DR) are shown in figure.

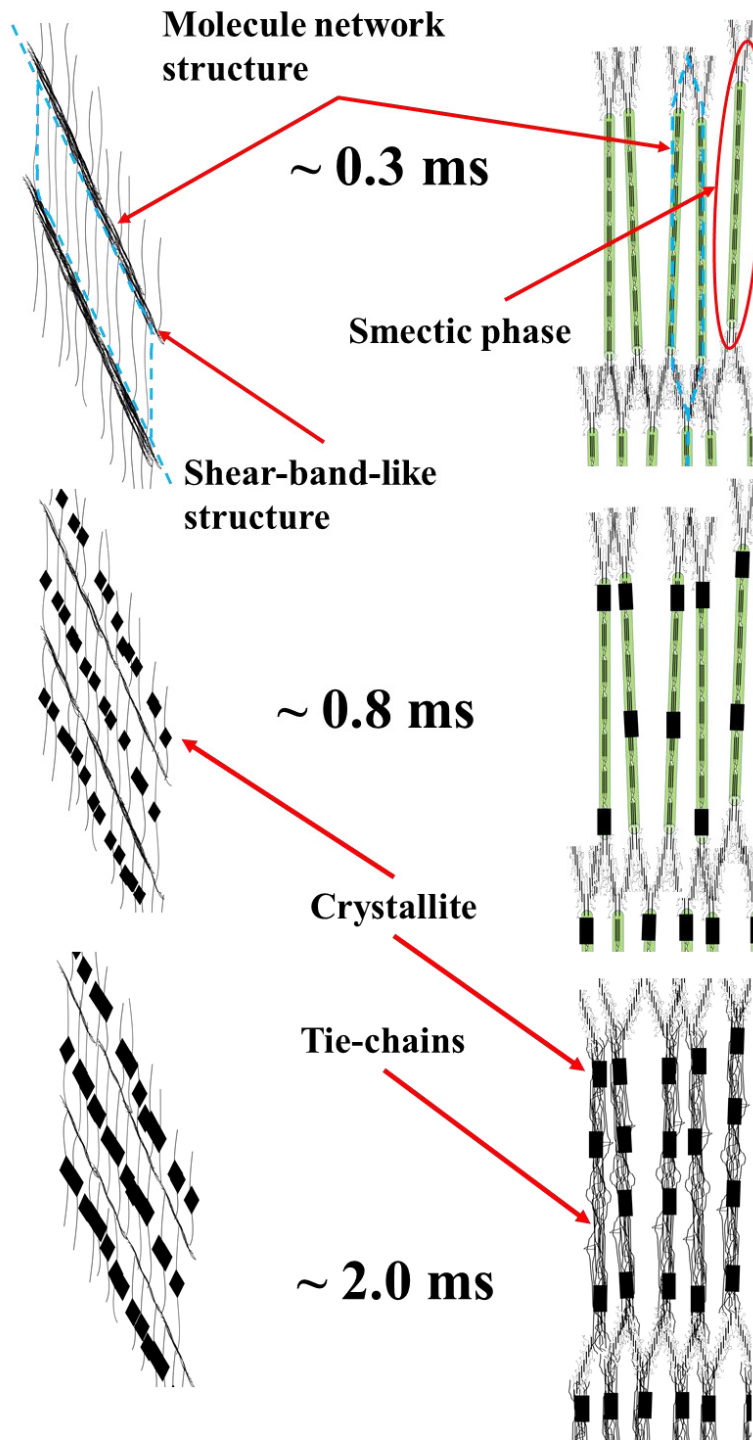### 3.8. Structure development and properties of drawn fibers

Fig. 3.11 shows a schematic diagram of fiber structure development. About 0.3 ms after necking, an X-pattern or smectic (001′) diffraction appeared for lower or higher draw ratios, respectively. Both structures were transformed into structures including oriented crystallites until 2 ms, at almost the same rate. For the minimum stable draw ratio of 3.0, the X-pattern arose from shear deformation of necking, and changed to a four-point pattern until 0.8 ms after necking, with the formation of crystallites. In contrast, for draw ratios of 4.2–4.5, bundles of oriented molecular chains formed by necking were transformed into a smectic phase until 0.3 ms after necking, and further transformed into the long-period structure of crystallites and amorphous phase. The transformation from the smectic phase to the long period structure started before 0.8 ms, and almost finished at 2.0 ms after necking. With the transformation, the long period decreased gradually with increasing formation of new crystallite in the fibrils. These phenomena are agreed with the model proposed by Yamaguchi et al. [1].

54

As mentioned Section 3.4, the (001′) diffraction was very weak and disappeared immediately after necking for fibers drawn at draw ratio 3.0 and 3.3. The draw ratio 3.0 is the minimum draw ratio, and it is almost the same with the NDR of as-spun fiber. Because the NDR is closely related to the yielding, intensity of the (001′) diffraction indicates that the excessive drawing stress over the yielding stress is necessary to form the smectic phase. The excessive drawing stress aligns the molecular chains along the fiber axis, and bundles of the aligned molecular chains should form the smectic phase. In contrast, the shear-band-like structure was formed by the yielding stress at the minimum draw ratio, while it was not observed for the higher draw ratio. For the latter case, we think that a part of molecular bundle formed along the shear-band was aligned to the fiber axis by the excessive stress, and the smectic phase was formed at necking instead of the shear-band-like structure.

The draw ratio dependences of the drawn fiber properties, shown in Table 2, can be explained by the fiber structure development. For draw ratios of 3.0–4.2, the change in the properties can be explained by an increase in the amount of smectic phase. The larger amount of the highly oriented fibrillar smectic phase transformed into the larger amount of long-period structure consist of a sequence of crystallites and amorphous phases. Because the larger the amount of taut tie chains connecting the crystallites in the long period structure bears the more tensile force applied to the drawn fiber in tensile test, a higher Young's modulus, higher tensile strength, and larger shrinkage stress of the drawn fiber were obtained [19, 20]. With increasing draw ratio from 4.2–4.5, the amount of smectic phase did not change but its d-spacing increased. The larger d-spacing in the smectic phase and smaller tilting angle is caused by higher drawing stress, which should be applied to the fibrillar smectic phases and molecular network connecting them. Because the more tensile force is applied to the molecular network connecting fibrils, which is the weakest point of the structure, the tensile strength increases more with increasing draw ratio. The molecular network connecting fibrils can be thought as the part of the stress-bearing network structure which determines the tensile strength of PET fibers [21].

DR 3.0   **DR 4.2 - 4.5**

Molecule network
structure

~ 0.3 ms

Smectic phase

Shear-band-like
structure

~ 0.8 ms

Crystallite

Tie-chains

~ 2.0 ms

Fig. 3.11 Schematic diagram of fiber structure development. The structures of the molecular
network in the fiber are shown as blue lines.

4. Conclusion

We investigated the effects of draw ratio on the fiber structure development of PET during continuous neck-drawing at draw ratios from 3.0 to 4.5, or drawing stress from 22 to 149 MPa. The fiber structure development was investigated using simultaneous WAXD/SAXS measurements until 2.0 ms after necking with a time resolution of 0.09–0.16 ms, achieved using an ultrahigh-intensity X-ray beam generated by the SPring-8 synchrotron facility equipped with an undulator.

An X-shaped SAXS pattern was observed, but no (001′) smectic phase diffraction was observed for the minimum stable draw ratio. The intensity of the (001′) diffraction increased with increasing draw ratio up to 4.2. However, no clear draw ratio dependences of the crystallization rate and induction time, 2.3–2.8 ms^{-1} and 0.4–0.6 ms, respectively, were observed. The d-spacing of the smectic (001′) diffraction and the long period both clearly decreased within 1 ms after necking. They increased with increasing draw ratio up to 4.2, whereas the (001′) d-spacing increased between draw ratios of 4.2 and 4.5.

The increase in the (001′) intensity suggests that a larger amount of fibrillar structures consisting of molecular bundles was formed with increasing draw ratio up to 4.2, and the larger d-spacing for a draw ratio of 4.5 suggests that more constrained molecular bundles formed in the fibrillar structure. The larger amount of constrained fibrillar structures can bear a greater tensile force in tensile tests, therefore the drawn fibers have higher tensile strengths.

References

1) T. Yamaguchi, K. H. Kim, T. Murata, M. Koide, S. Hitoosa, H. Urakawa, Y. Ohkoshi, Y. Gotoh, M. Nagura, M. Kotera, K. Kajiwara, *J. Polym. Sci., Polym. Phys.*, 46, (2008), 2126-2142.

2) K. Sugawara, T. Ikaga, K.H. Kim, Y. Ohkoshi, K. Okada, H. Masunaga, T. Kanaya, M. Masuda, Y. Maeda, *Polymer*, 79, (2015), 37-46.

3) A. Mehta, U. Gaur, B. Wunderlich, *J. Polym. Sci. Polym. Phys. Ed.*, 16, (1978), 289.

4) W. Okumura, T. Yamaguchi, Y. Ohkoshi, Y. Gotoh, M. Nagura, *Intern. Polym. Proc.*, 17, (2002), 124-132.

5) S. Kase, T. Matsuo, *J. Polym. Sci.*, 3, (1965), 2541-2554.

6) D. Kawakami, B. S. Hsiao, C. Burger, S. Ran, C. Avila-Orta, I. Sics, T. Kikutani, B. Chu, *Macromolecules*, 38, (2005), 91-103.

7) T. Asano, F. J. Balta Calleja, A. Flores, M. Tanigaki, M. Mina, C. Sawatari, H. Itagaki, H. Takahashi, I. Hatta, *Polymer*, 40, (1999), 6475-6484.

8) R. Bonart, *Kolloid-Z*, 213, (1966), 1-11.

9) 16K. H. Kim, R. Aida, Y. A. Kang, T. Ikaga, Y. Ohkoshi, I. Wataoka, H. Urakawa, *Polymer*, 53, (2012), 4272-4279.

10) T. Konishi, Y. Miyamoto, *Polymer*, 42, (2010), 349-353.

11) Y. Y. Tomashpol'skii, G. S. Markova, *Polym. Sci. USSR*, 6, (1964), 316-324.

12) K. H. Kim, T. Yamaguchi, Y. Ohkoshi, Y. Gotoh, M. Nagura, H. Urakawa, M. Kotera, T. Kikutani, *J. Polym. Sci., Polym. Phys*., 47, (2009), 1653-1665.

13) H. Masunaga, H. Ogawa et. al., *J. Polym*. 43, 471-477 (2011).

14) R. P. Daubeny, C. W. Bunn, *J. Polym. Sci., Polym. Chem*. 226, (1954), A1954, 531.

15) J. Simizu, T. Kikutani, A. Takaku, N. Okui, *Sen'i Gakkaishi*, 40, (1984), T63-72.

16) E. Funai, S. Sakurai, S. Hara, K. Yamamoto, S. Okamoto, J. Kojima, T. Kikutani, *Sen'i Gakkaishi*, 60, (2004), 322-330.

17) K. Okada, M. Nakada, Y. Higashioji, K. Takahashi, Y. Ohkoshi, T. Kanaya, *Koubunshi Ronbunshu*, 71, (2014), 593-600.

18) G. Stoclet, J.M. Lefebvre, R. Séguéla and C. Vanmansart, *Polymer*, 55, (2014), 1817-1828.

19) B. K. Samui, M. P. Prakasan, C. Ramesh, D. Chakrabarty, R. Mukhopadhyay, *J. Textile Institute*, 104, (2013), 35-45.

20) Y. Liu, L. Yin, H. Zhao, G. Song, F. Tang, L. Wang, H. Shao, Y. Zhang, *J. Appl. Polym. Sci.*, 2015, DOI: 10.1002/APP. 42512.

21) T. Kikutani et al. "*Fundamental and Practical Technologies for Nano-structured Polymeric Materials*", 2008, p.56-110, CMC press, ISBN978-4-7813-0043-6.

Chapter 4

Effects of dimensions and regularity on the mechanical properties of the smectic phase formed during orientation-induced crystallization of poly(ethylene terephthalate)

Chapter 4: Effects of dimensions and regularity on the mechanical properties of the smectic phase formed during orientation-induced crystallization of poly(ethylene terephthalate)

1. Introduction

In this Chapter, we investigated the effects of dimensions and regularity of the smectic phase on the mechanical properties by high-precision X-ray measurements. The drawing stress dependence was 76–168 MPa and the spinning speed dependence of 250–2000 m/min. We improved the measurement resolution to analyze the effects of the drawing stress on the d-spacing change in a high drawing stress region. In addition to the proportion and d-spacing, we also estimated the persistence length, thickness, and second disorder parameter of the fibrillar smectic phase to quantify the uniformity of the molecular chain alignment in the microfibril. We estimated the second disorder parameter from a Hosemann plot of the (001′), (003′), and (005′) diffraction results. Our analysis of the spinning speed and draw ratio dependence on the development of these structural parameters based on high-precision data enables us to discuss the quantitative contributions of inter-fibrillar and intra-fibrillar tie-chains to the mechanical properties of the resultant fibers.

2. Experimental

2.1. Samples

The fibers used for drawing were prepared by melt-spinning of PET (IV = 1.32 dL/g) supplied by Toray Industries, Inc. The polymer was heated at 300 °C and extruded from a one-hole nozzle at a mass flow rate of 5.0 g/min, and taken-up at 250–2000 m/min. The nozzle diameter was 1.0 mm, and the length/diameter ratio was 3.

2.2. Drawing

Fibers were drawn continuously by the speed difference between the feed and take-up rollers under heating by CO_2 laser irradiation [1]. The fiber running speed after necking was fixed at 130 m/min, and the draw ratio was controlled by changing the fiber-feed speed. A random polarized laser beam with a wavelength of 10.6 µm and a 6-mm spot diameter was generated by a PIN-30R laser (Onizuka Glass Co., Ltd.) and irradiated on to the running fiber from three different directions. The laser power for each drawing condition was determined so as to minimize the fluctuations of the neck-drawing point. The drawing tension was measured by a tension meter (HS-1500S, Eiko Sokki Co., Ltd.) with a 1-N pickup installed between the neck-drawing point and the take-up roller. The drawing stress was calculated from the drawing tension and the diameter of the drawn fiber. The drawing conditions are listed in Table 2.

2.3. On-line measurements

X-ray diffraction patterns were measured by irradiating the X-ray beam onto the running fiber. This on-line measurement system has been described in a previous report [1]. X-ray images were acquired at time points after necking by changing the distance between the X-ray irradiation point and necking point. The distance was changed with the necking point by moving the laser irradiation position. The elapsed time after necking was calculated from the distance divided by the fiber running speed. In particular for elapsed times less than 1.2 ms, the distance was measured accurately from video images taken during the measurement. The video images were acquired from the direction coaxial to the X-ray beam with a video camera (Watec Co., Ltd. WAT-232S type) equipped with a telecentric lens (OPTART Co., Ltd. TV-2S) with 2× magnification. In addition to the average position of the necking point, we also determined its fluctuation width from 10 still images taken from video images. These data were used to determine the time resolution of the measurements.

The synchrotron X-ray beam of SPring-8 BL03XU (FSBL) was used in this study. An undulator was equipped to obtain ultrahigh-intensity X-ray beams. The wavelength of the X-ray beam was 0.10 nm and the beam dimensions were 60 μm × 100 μm along the vertical and horizontal directions. An X-ray image of the smectic (001′) diffraction peak was acquired by irradiating X-rays perpendicular to the fiber axis (0–2θ arrangement). To obtain high-resolution images, the diffraction patterns were acquired with a direct-detection X-ray SOI-CMOS 2D detector, SOPHIAS (1.9 Mpixels, 30 μm square pixels, imaging area of 26.7×64.8 mm^2) [2]. This system has integrating-type pixels [3] and was operated at 20 frames/s. To verify the precision of the measurements, 10 images were taken and analyzed individually and then averaged. The camera length was 543 mm, and the exposure time was 6 s for each image.

In addition to the measurements in the above mentioned 0–2θ arrangement, measurements in the θ–2θ arrangement were performed to analyze the smectic (003′) and (005′) diffractions. For this purpose, the fiber axis was tilted 8.2° from the normal plane of the X-ray beam. The X-ray wavelengths were set to be 0.06 and 0.10 nm for the (003′) and (005′) diffractions peaks, respectively. A Pilatus detector of 1043×981 pixel (172 μm/pixel) was used for this measurement. The camera length and exposure time were 310 mm and 20 s, respectively.

The time resolution of the measurements was calculated from the fiber speed and the position resolution, which was calculated from the length of the necking point (0.08–0.53 mm), width of the X-ray beam (0.1 mm), and the above-mentioned fluctuation width (0.15–0.30 mm) of necking point. A time resolution of 0.1–0.3 ms was obtained for both the 0–2θ and θ–2θ arrangements.

2.4. Birefringence

Refer to section 2.4 of Chapter 2.

2.5. Thermomechanical tests

Refer to section 2.4 of Chapter 2.

3. Result and discussion

3.1 Properties and structures of PET fiber

The structure and physical properties of the as-spun fiber are shown in Table 4.1. The birefringence of the as-spun fiber increased with spinning speed, and the crystallinity also increased at more than 1000 m/min. The structure and physical properties of the drawn fiber are listed in Table 4.2. As the drawing stress increased from 80 to 170 MPa, the crystallinity of the drawn fiber changed little, and the birefringence and Young's modulus increased no more than 10%, whereas the tensile strength increased more than 20%, and the thermal shrinkage stress increased more than 50%. It has been reported that for fibers spun under conditions similar to those of this work, the proportion of the smectic phase increases sharply between 29–103 MPa, and almost saturates over 103 MPa [4]. The proportion of smectic phase was also saturated in this study (section 3.4) as indicated by the crystallinity data above. Hence, we will discuss the reasons for the increase in tensile strength and thermal shrinkage stress after saturation of the smectic phase on the basis of our high-resolution d-spacing measurements and the sizes of the smectic phase.

Table 4.1 Structure and properties of as-spun fibers

Spinning speed / m min⁻¹	NDR	Birefringence	Cold-crystallization temperature/°C	Melting temperature / °C	Crystallinity / %	Tensile strength / MPa	Elongation / %	Young's modulus / GPa
250	3.5	0.001	139	253	6	143	558	2.0
500	3.0	0.004	135	253	6	162	477	2.0
1000	2.1	0.010	129	252	9	208	347	2.1
1500	1.8	0.020	124	253	13	274	249	2.1
2000	1.5	0.038	121	252	15	319	175	2.3

Table 4.2 Structure and properties of drawn fibers

Sample *	Spinning speed / m min⁻¹	Drawing stress / MPa	Draw ratio	Laser power / W	Necking length /mm	Resolution time /ms	Birefringence	Melting temperature / °C	Crystallinity / %	Tensile strength / MPa	Elongation / %	Young's modulus / GPa	Maximum shrinkage / %	Maximum shrinkage stress Stress / MPa	Maximum shrinkage stress Temperature / °C
250-H	250	165	5.5	25.4	0.08	0.11	0.201	256	35	1080	20	10.9	22.1	85	184
250-M	250	103	5.0	24.9	0.10	0.10	0.187	256	36	940	29	9.8	19.6	66	165
250-L	250	76	4.7	24.5	0.14	0.11	0.180	255	30	850	39	8.8	19.1	50	167
500-H	500	168	4.6	26.2	0.11	0.14	0.184	256	36	1010	26	10.6	12.0	84	183
500-M	500	99	4.2	25.0	0.13	0.11	0.176	256	35	880	33	10.4	11.5	68	172
500-L	500	81	4.0	23.8	0.12	0.11	0.168	255	33	810	38	10.0	10.5	55	179
1000-M	1000	96	3.1	24.7	0.14	0.11	0.166	256	36	820	33	10.8	7.3	58	172
1500-M	1500	93	2.5	24.4	0.29	0.16	0.161	256	36	790	33	10.1	6.6	65	165
2000-M	2000	110	2.1	25.0	0.53	0.29	0.157	256	42	830	31	11.1	6.1	66	182

* Sample name : [Spinning speed / m min⁻¹ – Drawing stress (High ~165 MPa / Medium ~100 MPa / Low ~80 MPa)]

3.2 Drawing Phenomena

Necking lengths are shown in Table 4.2. Because of the constant mass flow rate of 5.0 g/min, the diameter of the as-spun fiber decreased with spinning speed. The necking length clearly increased with the spinning speed, but hardly changed with the drawing stress despite the increase of the diameter change. Okumura et al. also reported that the necking length is almost independent of the drawing stress [5]. Because the take-up speed was fixed at 130 m/min in this study, a longer necking width requires a longer time for necking deformation, which might be explained by the uniformity of the network structure as discussed in section 3.6.

The fiber temperature profile was estimated from the energy balance equation considering the laser irradiation energy, heat transfer from the fiber surface, work of the external force of plastic deformation, and the latent heat of crystallization [1]. The necking point was decided by image analysis of video-images and the heat transfer coefficient was estimated by the empirical formula proposed Kase and Matsuo [6]. The absorption coefficient 1.149×10^4 (m^{-1}) [7] was used for the absorption of the PET fiber by the CO_2 laser. The heat of fusion of the drawn fiber (Table 4.3) was used as the heat of crystallization. The crystallization rate and crystallization induction time are listed in Table 4.3. For spinning speeds greater than 500 m/min, the reported values [4, 8] for the same spinning and drawing conditions are used for the calculation, whereas for 250 m/min, the values estimated from previous reports are used. The estimated fiber temperatures are also shown in Table 4.3. The temperature just before necking had little dependence on the drawing stress; however, the temperature immediately after necking increased with the drawing stress. The temperatures at the same drawing stress increased with spinning speed. The fiber temperature increased by 5–6 K within 0.3 ms from necking, at which point the smectic phase was most clearly observed by X-ray diffraction. The temperature at 0.3 ms represents a 35-K increase with the drawing stress and a 34-K decrease with the spinning speed.

Table 4.3 Fiber temperatures estimated for the drawing conditions

Sample	Heat of fusion / Jg⁻¹	Crystallization induction time / ms	Crystallization rate / 10^3 s⁻¹	Temperature immediately before the necking /°C	Temperature immediately after the necking /°C	Temperature at 0.3 ms after the necking /°C	Max. Temp. /°C & (Elapsed time / ms)
250-H	48			105	175	180	214 (2.2)
250-M	49	0.6 *	2.3 *	109	151	156	191 (2.2)
250-L	41			110	140	145	176 (2.2)
500-H	48	0.5 [17]	2.5 [17]	104	172	178	215 (1.9)
500-M	47	0.6 [17]	2.3 [17]	106	145	151	186 (2.1)
500-L	44	0.6 [17]	2.3 [17]	105	137	142	175 (2.2)
1000-M	49	0.5 [16]	3.7 [16]	97	131	138	176 (1.6)
1500-M	49	0.4 [16]	3.5 [16]	90	120	126	165 (1.5)
2000-M	57	0.4 [16]	7.7 [16]	84	117	122	167 (1.4)

* assumed value

3.3 X-ray diffraction images

X-ray diffraction images acquired for 500-M are shown Figure 4.1(a), and the meridional intensity profiles are shown in Figure 4.1(b). The streak-like diffraction shown at the right end of Figure 4.1(a) is the (001′) diffraction peak of the smectic phase. The (001′) diffraction peak appeared 0.1 ms after necking and achieved its maximum intensity at 0.3 ms, after which it gradually disappeared. The angle of the (001′) diffraction peak clearly increased with elapsed time. The intensity of the diffraction decreased with spinning speed but did not depend on the drawing stress.

Inclined X-ray diffraction images taken in the θ–2θ arrangement are shown in Figure 4.2. At a fixed tilt angle the X-ray wavelength was changed to locate the (003′) and (005′) reciprocal lattice points on the Ewald sphere. For all samples, the amorphous halo was concentrated in the equatorial direction by necking and the equatorial crystal diffractions appeared in the halo at 0.6 ms after necking. Diffraction peaks of the (−105) and (−103) crystal planes also appeared at 0.4−0.6 ms. In addition, streak-like meridian (001′), (002′), (003′), and (005′) diffraction peaks appeared 0.2 ms after necking. These diffraction peaks weakened at 0.4−0.6 ms accompanied by the appearance of (−105) and (−103) diffraction peaks.

The widths of the (00l′) diffraction peaks along both the meridional and equatorial directions appeared to increase with the diffraction order l. The equatorial widths of the (00l′) diffraction peaks are related to the disorientation and/or disordering of the molecular chains of the smectic phase. The former of these factors expands the peak width along the azimuthal angle, whereas the latter causes expansion along the direction perpendicular to the meridian. Kim et al. [9] attributed the widths of the (001′) and (003′) diffraction peaks to the effects of the disorientation and thickness. However, the increase of the azimuthal width with the diffraction order described above cannot be explained by the effects of either disorientation or thickness. Hence, we attribute this peak width behavior mainly to disorder of the chain arrangement along the chain axis. To evaluate the degree of disorder, we estimated the apparent thickness from the width of the (001′) diffraction peak perpendicular to the meridian.

The d-spacing and the persistence length of the smectic phase were also evaluated from the peak position and the meridian width of the (001′) diffraction. In addition, a second disorder parameter was obtained from the meridian widths of (001′), (003′), and (005′) diffraction features. The peak position and widths were obtained by peak fitting along each direction. The Gaussian and Pearson VII (Equation 4.1) functions were used to fit the profiles along and perpendicular to the meridian, respectively, as:

$$I_{(\varphi)} = \frac{I_0}{\left\{1+4\left(\frac{\varphi}{\beta_p}\right)^2\left(2^{\frac{1}{m}}-1\right)\right\}^m} \tag{4.1}$$

where I, β_p, and $m = 2.0$ are the intensity, width, and shape factor of profile perpendicular to the meridional direction, respectively. The parameter $\varphi = \tan^{-1}(x/C)$ is the angle from meridian, in which x and C are the distance from the meridian and the camera length. All the obtained profiles showed good agreement with the measured profiles.
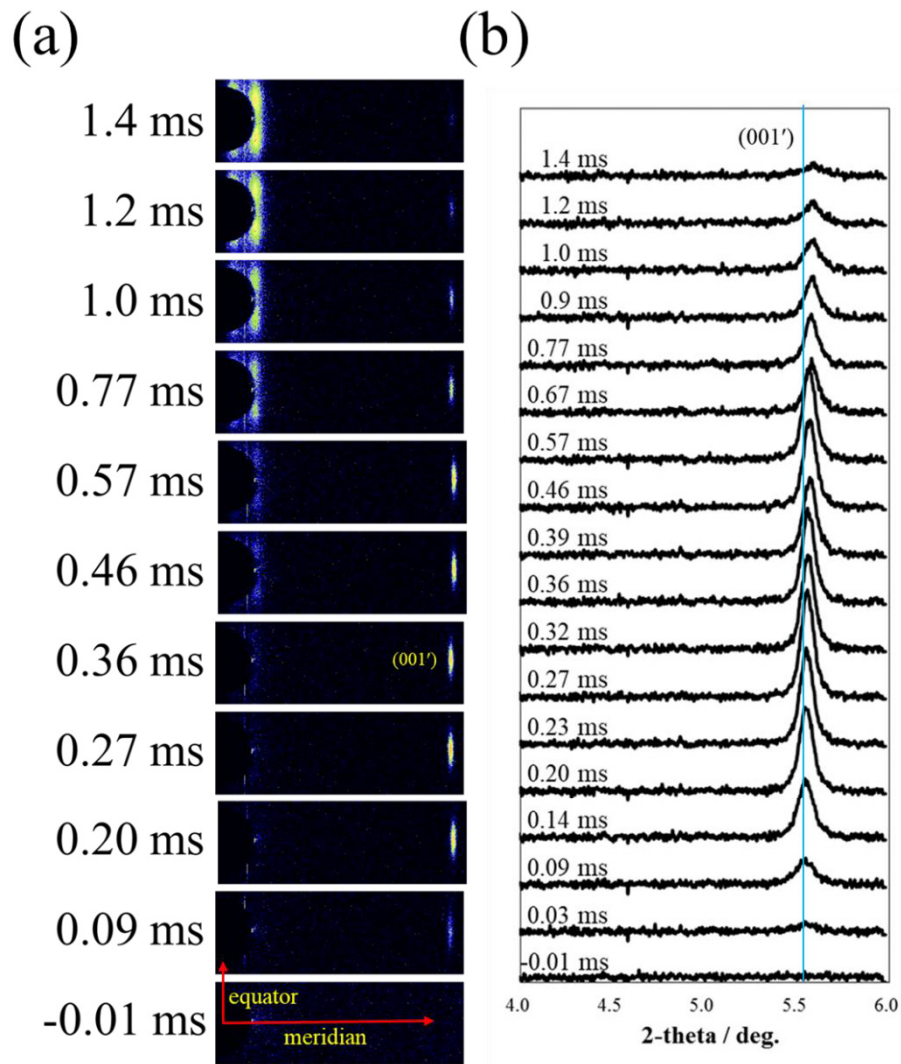

Figure 4.1 X-ray diffraction pattern (a) and meridional intensity profile (b) for 500-M. Times elapsed after necking are noted in the figure.
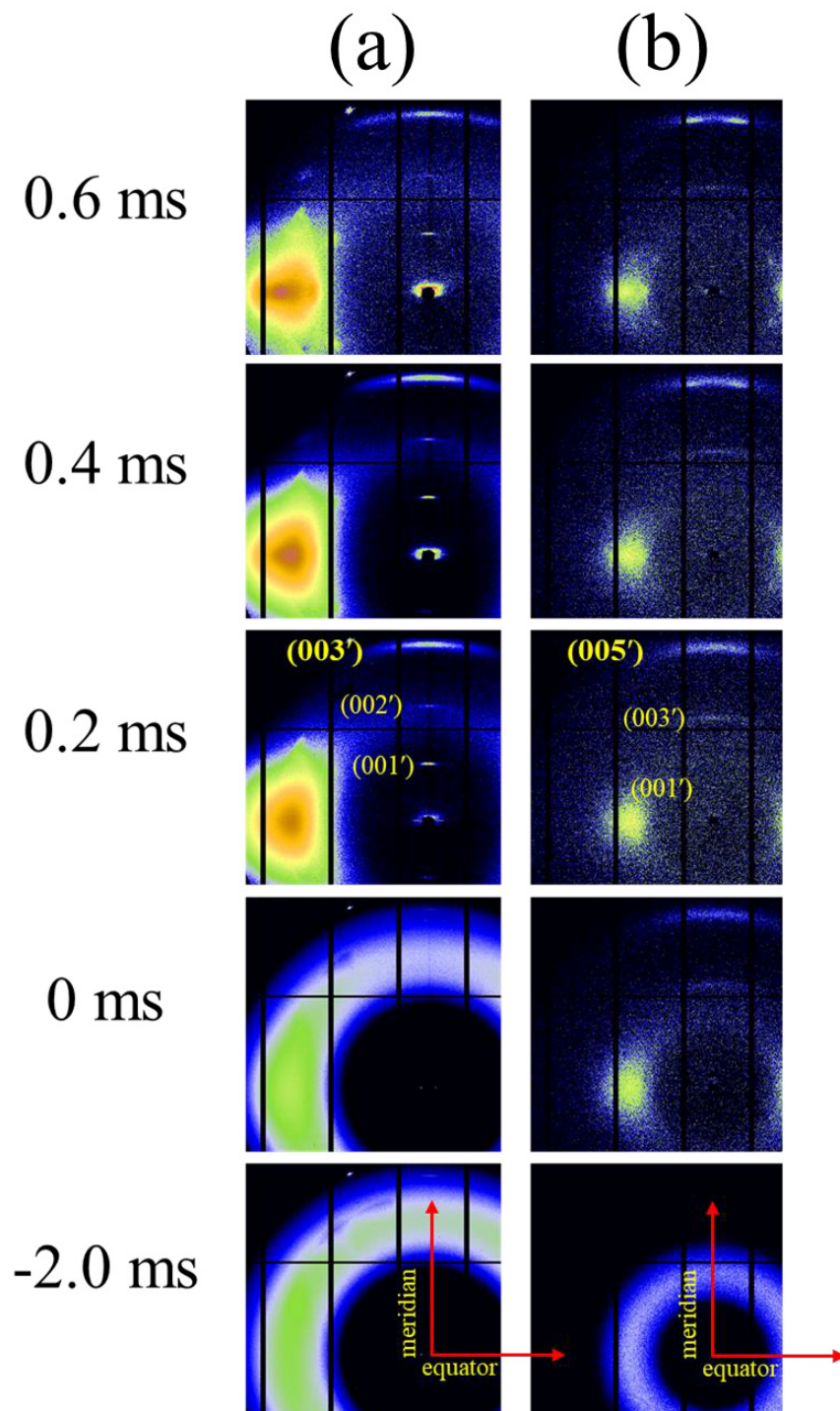
Figure 4.2 Inclined X-ray diffraction patterns for 500-M. Times elapsed after necking are noted in the figure. The fiber axis is inclined 8.2° from the meridian to fit the reciprocal lattice point of the (a) (003′) or (b) (005′) plane to the Ewald sphere by selecting the X-ray wavelength to be (a) 0.10 nm and (b) 0.060 nm.

3.4 Amount of smectic phase

The integrated intensities of the (001′) diffraction in the range of the diffraction angle 5°–6° are shown in Figure 4.3. Because the X-ray beam size in the direction perpendicular to the fiber of 60 μm was larger than the diameter of all the drawn fibers, we assumed that the X-ray beam irradiated the whole volume of the running fiber. Thus, the obtained integrated intensity was normalized by the X-ray irradiation volume. The intensity achieved a maximum at 0.3 ms after necking. The maximum intensity decreased with spinning speed but did not depend on the drawing stress. However, the intensity for drawing under the maximum drawing stress increased more rapidly than that at low drawing stress.
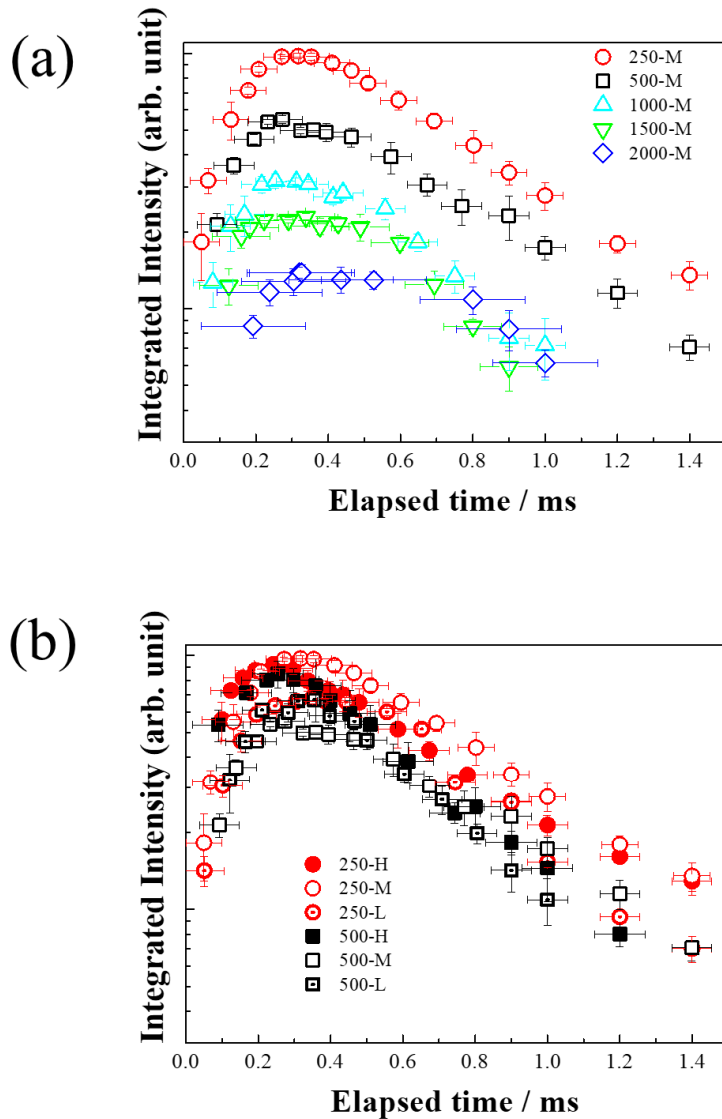
Figure 4.3 Integrated intensity of smectic (001′) diffraction peak normalized by the X-ray irradiated volume. Spinning speed dependence (a) and drawing stress dependence (b) are shown.

3.5 Size and disorder of microfibrils

The persistence length L and the apparent thickness D of the smectic phase were estimated by the Scherrer formula (4.2):

$$L = \frac{K\lambda}{\beta_a \cos \theta_a}, \qquad D = \frac{K\lambda}{\beta_p} \qquad\qquad (4.2)$$

where, λ is the X-ray wavelength and the constant K is 1. The half-diffraction angle θ_a, and integral widths (β_a, β_p) along and perpendicular to the meridian of the (001′) diffraction were used for the calculation. The Hosemann's second disorder parameter g_{II} was calculated from Equation 4.3 [10]:

$$\left(\frac{\beta_m \cos \theta_m}{\lambda}\right)^2 = \left(\frac{1}{L}\right)^2 + \frac{(\pi g_{II} m)^4}{d^2} \qquad\qquad (4.3)$$

where β_m is the integral width of the (00m′) diffraction peaks, and d is the d-spacing of the (001′) diffraction. The integral widths β_3 and β_5 were obtained from the inclined measurements (Figure 4.2). The above-mentioned integral width of the (001′) diffraction peak (β_a in Equation 4.2) for the corresponding elapsed time ±0.1 ms was used as β_1.

The calculated persistence length and thickness are shown in Figure 4.4 and 4.5, respectively. Both these factors showed a similar time dependence on the integral intensity, and both maximum values also showed a tendency to decrease with spinning speed and no dependence on the drawing stress. However, the persistence length increased rapidly at a higher drawing stress, and the thickness decreased rapidly after the maximum value at the maximum drawing stress. A typical Hosemann plot is shown in Figure 4.6. The points for the (001′), (003′), and (005′) diffraction peaks were not aligned on a straight line for all elapsed times, all spinning speeds, and all drawing stresses. We obtained two sets of g_{II} values from the datasets of (β_1, β_3, β_5) and (β_1, β_3), which expressed almost the same features; however, the g_{II} values obtained from (β_1, β_3, β_5) showed greater deviation caused by the larger deviation of β_5 particularly at the longer elapsed time. The greater β_5 deviation for the longer elapsed time is likely caused by the effects of overlap with the (−105) diffraction peak. Therefore, we selected the g_{II} values obtained from (β_1, β_3) for Figure 4.7. Under all conditions, g_{II} reached a minimum value of 3.7%–4.3% at 0.4 ms after necking. The minimum g_{II} values were clearly greater than the g_{II} values reported for the c-axis direction of PET crystal (<1%) [11]. This result indicates a lower regularity of the molecular chain rearrangement along the chain axis in the smectic phase than that in the crystal.

In addition to the maximum of integrated intensity, the persistence length, thickness, and g_{II} also reached their minimum values 0.3–0.4 ms after necking. This elapsed time was almost the same as the reported crystallization induction time of 0.3–0.5 ms [4, 8]. These results indicate that oriented

molecular bundles of the nematic state formed by necking changes to the smectic phase up to 0.3–0.4 ms, followed by further changes to the crystals. The nematic–smectic transition requires an axial shift of the molecular chain in the oriented molecular bundle. Despite the long persistence length of 50–70 nm, which indicates well-aligned polymer chain bundles, the smectic phase shows a clearly larger g_{II} value than that of the crystal. Thus, we attribute the disorder of the molecular chain arrangement to an incomplete axial shift between the molecular chains. The tendency of the azimuthal width to increase with diffraction order (as shown in section 3.3) can also be explained by residual disorder between the molecular chains. The faster increase in the integral intensity and persistence length and the faster decrease in thickness observed for the higher drawing stress are also caused by the axial shift promotion of drawing stress. That is to say, the external force applied through the inter-fibrillar tie-chains promoted the axial shift and accelerated the nematic–smectic transition. However, the higher drawing stress likely preserved a greater disorder between the molecular chains, which contributed to the thinner apparent fibril thickness.
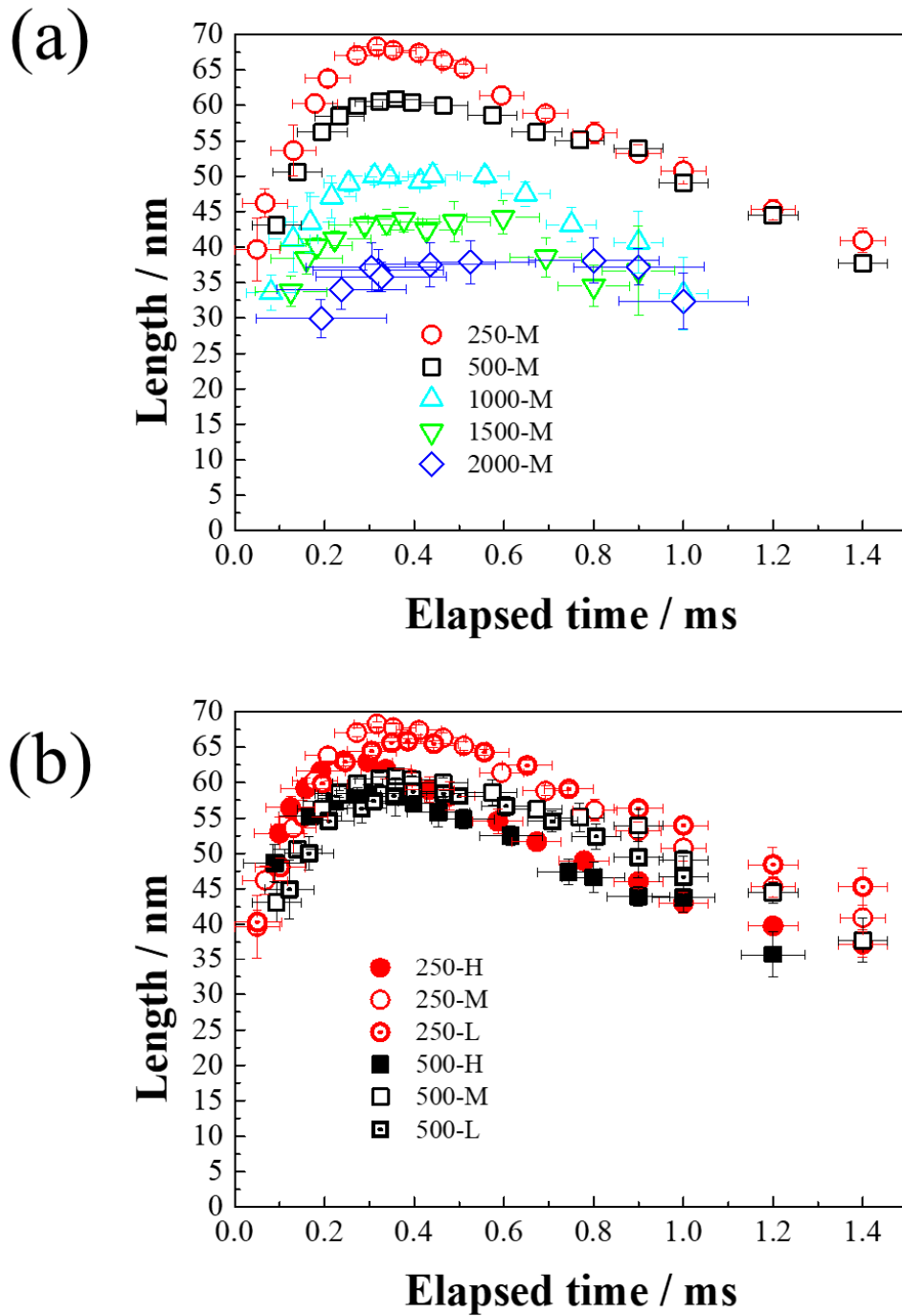
Figure 4.4 Persistence length of smectic phase estimated by equation 4.2. Spinning speed dependence (a) and drawing stress dependence (b) are shown.
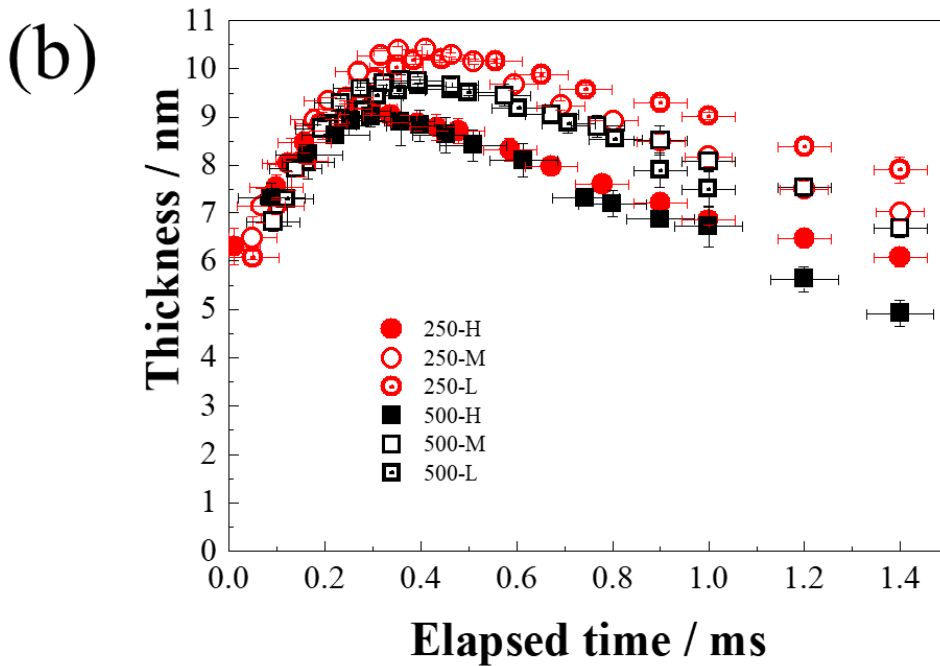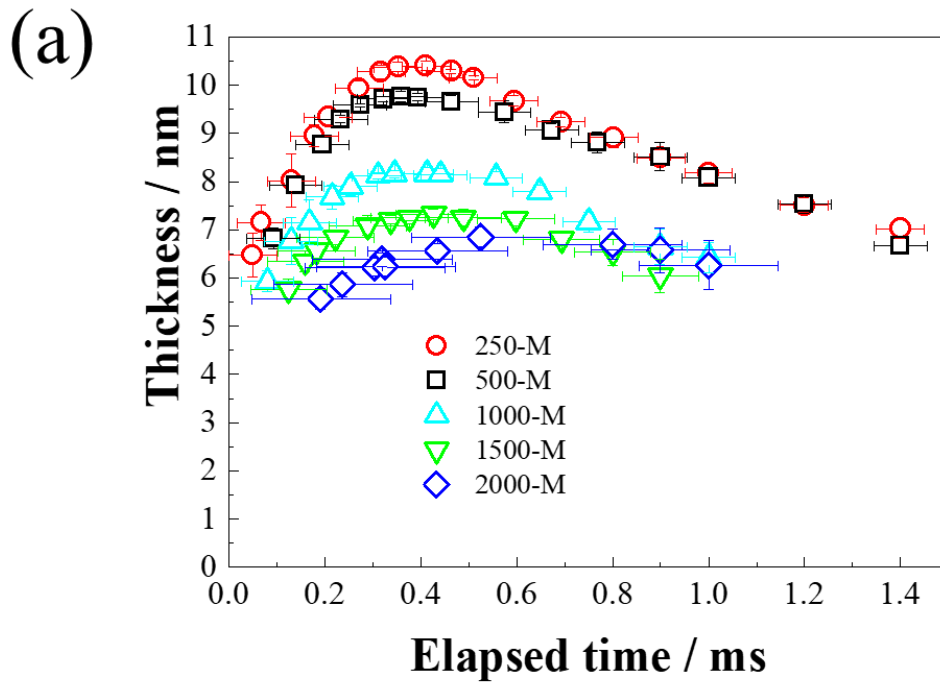
Figure 4.5 Thickness of smectic phase estimated by equation 4.2. Spinning speed dependence (a) and drawing stress dependence (b) are shown.
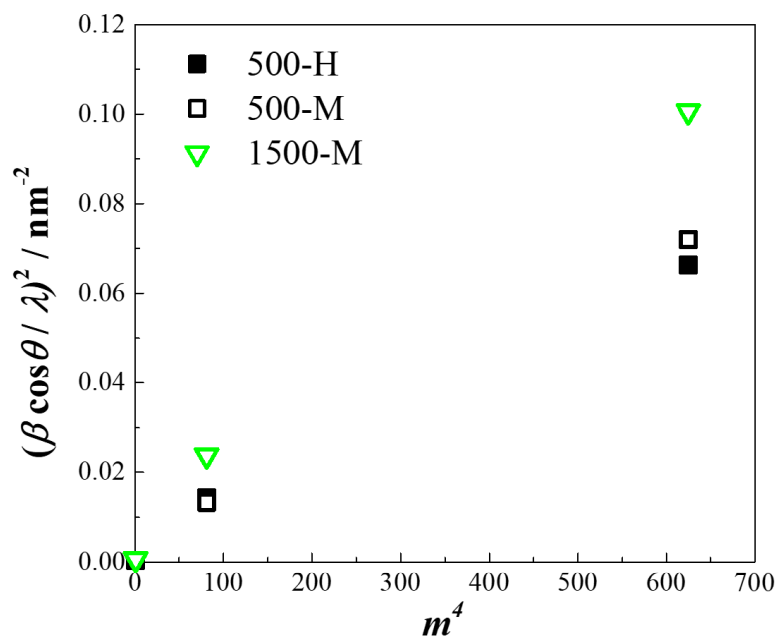
Figure 4.6 Hosemann plot for smectic (001′), (003′), and (005′) diffraction peaks at 0.4 ms. Sample names are noted in the figure.
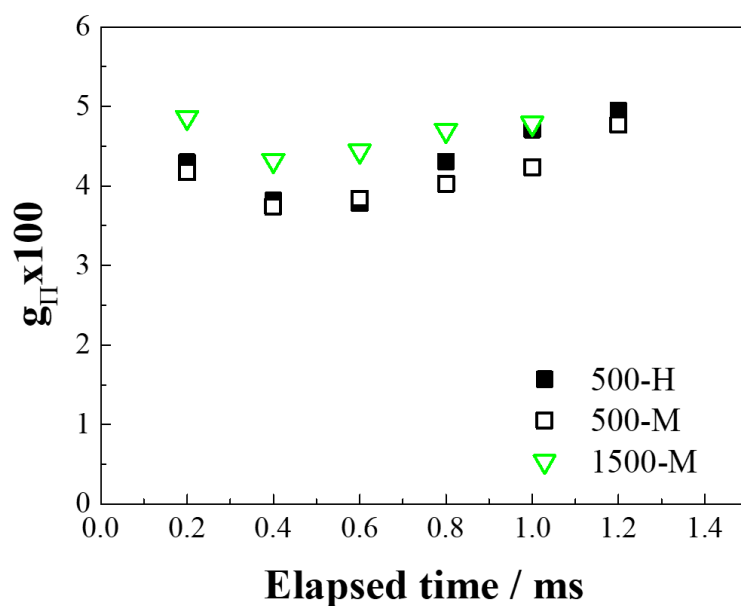

Figure 4.7 Disorder parameter g_{II} estimated from the smectic (001′) and (003′) diffractions following equation 3. Sample names are noted in the figure.

3.6 Uniformity in Network Structure

As shown in 3.5, the maximum persistence length strongly depends on the spinning speed but has little dependence on the drawing stress. The maximum persistence length plotted against the natural draw ratio (NDR) of the as-spun fiber is shown in Figure 4.8. The NDR, listed in Table 4.1, is considered to reflect the uniformity in the entanglement density and the chain orientation of the polymer chain network [12]. As shown in the figure, both the maximum persistence length and NDR decreased with spinning speed. In particular, at spinning speeds greater than 1500 m/min, the persistence length decreased more markedly.

As will be discussed in section 3.7, the smectic phase was considered to consist of well-aligned polymer chain bundles. Entanglements were excluded from the polymer chain bundle; thus, the maximum persistence length of the smectic phase was limited by the distance between entanglements. The decreases of both the maximum persistence length and NDR with spinning speed indicate that the spinning process determines the network structure, uniformity in the entanglement density, and chain orientation. Masubuchi et al. [13] reported that the uniformity in entanglement density decreased with spinning speed. That is, although the overall number of entanglements decreased with elongational deformation of the spinning the entanglement density near the chain ends hardly decreased. Owing to the decrease in the uniformity of entanglement density, the NDR decreased with the decrease in the shortest length of the network link bearing an external force. The decrease in the shortest length of the force-bearing network link should decrease the maximum persistence length of the smectic phase. The decrease in the uniformity should also increase the necking length, as shown in section 3.1, i.e., polymer networks with less uniformity require a longer time for yielding. The greater decrease in the persistence length than in the NDR observed at spinning speeds greater than 1500 m/min, as well as the clear decrease in the integral intensity and thickness, and the increase in g_{II}, can be explained by the stress concentration caused by oriented-nuclei formed in the spinning line [8]. Owing to stress concentration, the stress applied to the molecular bundle should decrease to suppress the axial shift of molecular chains.

The above results provide a structural basis for the empirical rule [12] that the maximum attainable strength of the PET fiber is determined mainly by the spinning conditions. As shown in Table 4.2, in this study fibers spun at higher speeds also had lower strength after drawing under the same drawing stress. The accessible drawing stress also generally decreases with spinning speed [8]. Therefore, the maximum attainable strength clearly decreases with spinning speed. The trend of the persistence length to decrease with spinning speed confirmed the validity of the obtained persistence length as a structural parameter for estimating uniformity in the entanglement density of polymer chain networks and the attainable maximum strength of resultant fibers.
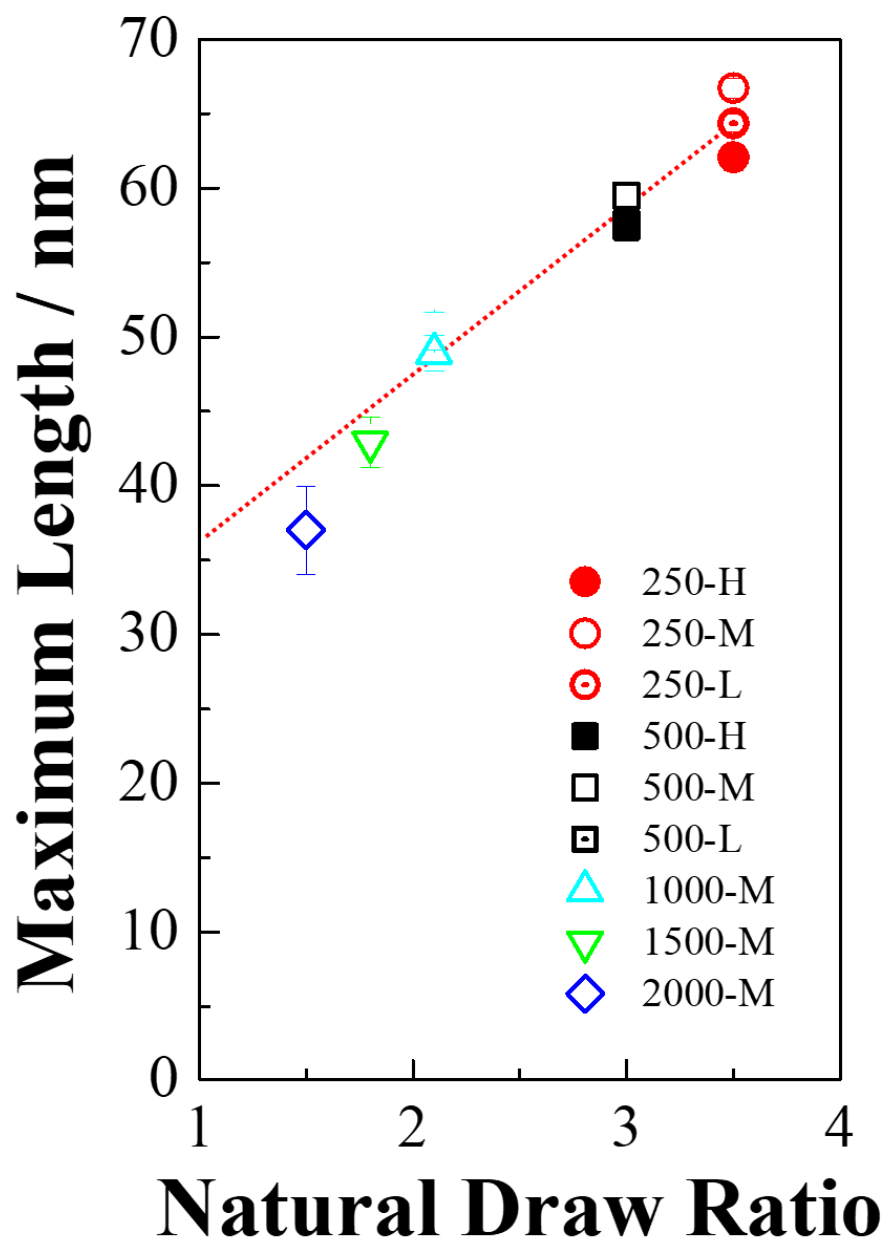
Figure 4.8 Observed maximum length of the smectic phase plotted against the NDR of the as-spun fiber. Sample names are noted in the figure.

3.7 d-spacing of smectic phase

The d-spacing d was determined by Bragg's equation (4.4):

$$2d\sin\theta = \lambda \qquad (4.4)$$

where θ is half of the (001′) diffraction angle. Obtained d-spacings are shown in Figure 4.9. All d-spacings decreased monotonically with time, and tended to decrease with spinning speed, in particular at spinning speeds of more than 1000 m/min. The larger variation at 2000 m/min is likely caused by the low intensity of the observed diffraction peaks.

Similar to the results of sections 3.4 and 3.5, the change in the d-spacing can be discussed separately before and after the elapsed time of 0.3–0.4 ms. Before that time, the change in d-spacing was strongly influenced by the spinning and drawing conditions, namely, a greater decrease was observed for fibers spun at higher spinning speeds or drawn under higher stress. The d-spacing continued to decrease after that time. The spinning-speed dependence of the d-spacing changed in the latter period, which corresponded well with the dependence of crystallization rate [8]. This result suggests that the d-spacing was decreased mainly by tilting of molecular chains owing to the phase transition from smectic to crystal [4, 8, 14]. Next, we consider the d-spacing in the earlier period, which is determined by the stress applied to the oriented chain bundle. In particular, the larger d-spacing observed in fibers formed under a higher drawing stress appeared to be caused by molecular chain extension. This presumption of molecular chain extension induced by the drawing stress is supported by the fiber temperature profiles measured by Yamaguchi et al. [15] and Kim et al. [16]. They reported that the measured fiber temperature immediately after necking was lower than the temperature estimated by assuming that the temperature increase was caused by work applied at the necking. The temperature difference increased together with the drawing stress, and disappeared with formation of the smectic phase. They suggested that a part of the applied work was stored as elastic energy, and released by relaxation of the extended molecular chain.

The d-spacing values of 1.017–1.068 nm [1, 9, 16-21] have been reported for the smectic phase formed in high-draw-ratio drawing of a low molecular orientation fiber. Previously reported d-spacings and those obtained in this study are plotted against the estimated fiber temperature (Figure 4.10). The d-spacings of approximately 0.3 ms were selected for the reported values, which had a time-resolution higher than 0.3 ms, whereas the maximum value was selected for the values having a lower time-resolution. All the d-spacings exceeded 95% for the crystal c-axis length of PET 1.077 nm [22], and tended to decrease with fiber temperature. The decreasing tendency can be explained by molecular chain shrinkage owing to entropic effects. The d-spacing value extrapolated to the room temperature was almost equal to the c-axis length of the crystal. Moreover, by using computer simulations, Abou-Kandil et al. revealed that all-trans conformations of methylene units are required for the smectic

(001′) diffraction peak to appear [23]. Therefore, the smectic phase can be regarded as a bundle consisting of perfectly oriented and almost fully extended molecular chains.
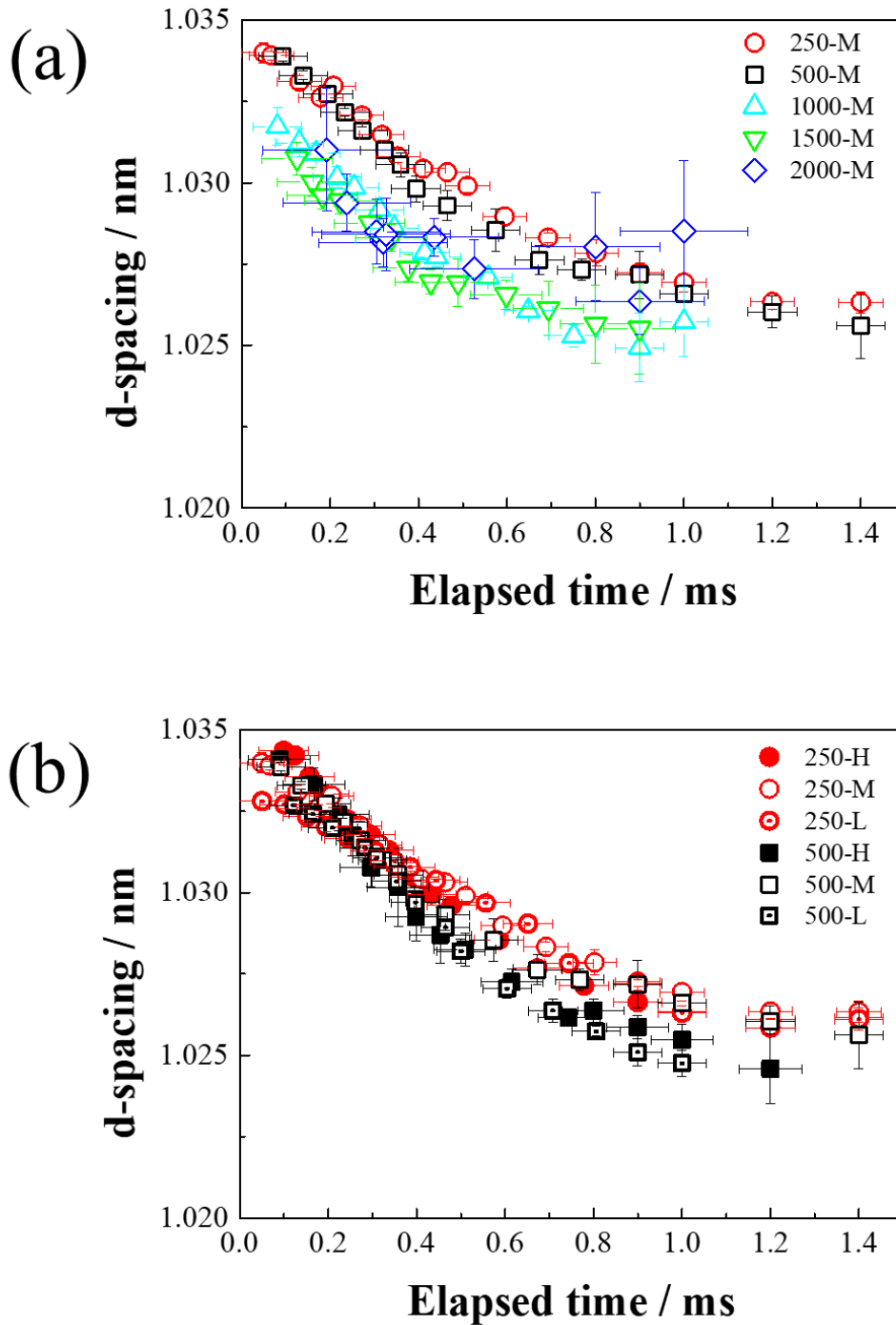
Figure 4.9 (a) Spinning speed and (b) drawing stress dependence on the d-spacing of smectic (001′) diffraction peak.
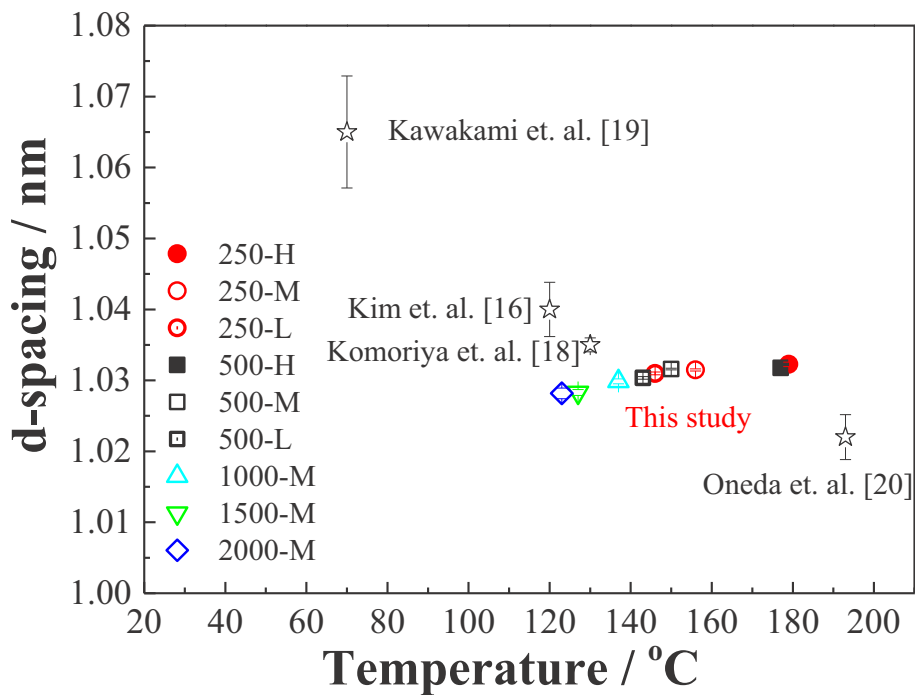
Figure 4.10 Reported d-spacing of smectic (001′) diffraction peak. Maxima or data for the maximum intensity around 0.3 ms, are plotted against the corresponding fiber temperature.

3.8 Modulus of the force-bearing molecular bundle

The high-resolution of the SOPHIAS detector enabled a nominal precision for the d-spacing of 0.6 pm. In fact, the standard deviations of all the obtained d-spacings shown in Figure 4.9 were less than 1 pm except for the data relating to very weak diffraction peaks. With the use of this high-precision d-spacing data, we tried to estimate the elastic modulus of the oriented molecular chain bundle from the drawing stress dependence. Figure 4.11(a) shows the same data as Figure 4.9; however, two data points of weak intensity, appearing immediately after necking at an elapsed time ~0.05 ms, were excluded because of their low accuracy. The d-spacing values measured from 0.10 to 0.25 ms indicated a clear drawing stress dependence but no clear spinning speed dependence between 250 and 500 m/min. The d-spacings lay on a straight line for each drawing stress within measurement error and appeared to converge at an elapsed time of 0.25–0.30 ms when the smectic formation was almost completed. This result suggests that the extended molecular chains relaxed with the axial shift between the chains. The average chain extension immediately after necking was estimated by extrapolating the d-spacing to the elapsed time zero. By plotting the extrapolated values against the drawing stress, as shown in Figure 4.11(b), the apparent elastic modulus of the oriented molecular chain bundle was determined

to be 40 GPa from the slope and intercept of the figure [24]. The accuracy of this value is not sufficiently high because the d-spacing depends on the fiber temperature, as shown above. That is, although the estimated fiber temperature for the same drawing stress increased no more than 6 K with elapsed time, the temperature increased up to 35 K with the drawing stress. A lower estimated modulus might be obtained by considering the temperature increase with drawing stress.

The obtained elastic modulus of 40 GPa is 1/3 smaller than the reported crystal modulus for PET (125 GPa), and 4 times as large as the Young's modulus of the drawn fibers (9–11 GPa). Because the fiber temperature immediately after necking was higher than the glass transition temperature of PET, only the orientated chain bundles, which account for approximately 1/3 of the molecules in the fiber cross-section, bear the drawing stress. Furthermore, when the obtained fibers were stretched at room temperature, the extension of microfibrils was considered to be limited to no more than 1/4 of the whole fiber extension because the modulus of microfibrils was no less than 40 GPa. As a result, most of the fiber strain can be attributed to the deformation of the inter-microfibrillar region.
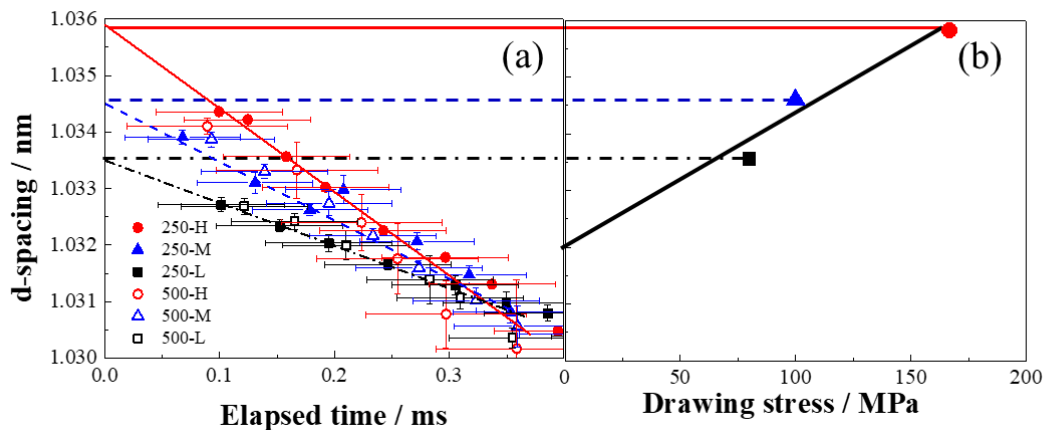
Figure 4.11 Extrapolation of (001′) d-spacings to the elapsed time of zero. An enlargement of Figure 4.9 (a) and extrapolated data are plotted against each drawing stress (b).

4. Conclusions

The effects of dimensions and regularity of a fibrillar-shaped smectic phase on mechanical properties of fibers were investigated by high-precision X-ray measurements with the use of the SOPHIAS detector. The drawing stress was set to be 76–168 MPa, a range over which the proportion of the smectic phase is reportedly almost saturated. The spinning speed dependence of 250–2000 m/min was also measured under a fixed drawing stress of approximately 100 MPa. Changes in the proportion, d-spacing, persistence length, and thickness of the smectic phase were measured from the intensity, peak position, and widths of the smectic $(001')$ diffraction peak, from just before necking to 1 ms after necking. Hosemann's g_{II} parameters were also determined from the meridian widths of the $(001')$ diffraction peak, and the $(003')$ and $(005')$ diffraction peaks obtained by inclined measurements.

The proportion, persistence length (50–70 nm) and thickness achieved maximum values, and g_{II} reached a minimum value (3.7–4.3%) at 0.3–0.4 ms after necking. The maximum and minimum values clearly depended on the spinning speed but showed little dependence on the drawing stress. The g_{II} value increased with spinning speed suggesting an incomplete axial shift between molecular chains. The persistence length and NDR of the as-spun fiber showed a linear relationship; however, a greater decrease in the persistence length than the NDR was observed at more than 1500 m/min.

The maximum value of the proportion and persistence length and thickness showed almost no dependence on the drawing stress. However, the proportion and persistence length increased more rapidly with drawing stress, and the thickness decreased more rapidly for the maximum drawing stress. The d-spacing of the smectic phase tended to decrease with temperature. Because the value extrapolated to room temperature almost corresponded to the crystal c-axis length, the smectic phase can be regarded as a bundle consisting of perfectly oriented and almost fully extended molecular chains. By increasing the d-spacing with drawing stress, an apparent elastic modulus of approximately 40 GPa was obtained for the oriented molecular bundle. This value suggests that external force concentrates on inter-microfibrillar tie-chains during tensile testing. We explain the considerable increase in tensile strength and thermal shrinkage stress, compared with the increase in the Young's modulus and birefringence, as drawing stress was increased, by the difference in the number and orientation of inter-microfibrillar tie-chains.

References

1) T. Yamaguchi, K. H. Kim, T. Murata, M. Koide, S. Hitoosa, H. Urakawa, Y. Ohkoshi, Y. Gotoh, M. Nagura, M. Kotera, K. Kajiwara, *J. Polym. Sci., Polym. Phys.*, 46, (2008), 2126-2142.

2) T. Hatsui, M. Omodani, T. Kudo, K. Kobayashi, T. Imamura, T. Ohmoto, A. Iwata, S. Ono, Y. Kirihara, T. Kameshima, *Proc. Int. Image Sensor Workshop*, 2013, Art. No. 3.05. http://www.imagesensors.org/Past%20Workshops/2013%20Workshop/2013%20Papers/03-_058_hatsui_paper.pdf

3) T. Hatsui, H. Graafsma, *IUCrJ* 2015, 2, (3), 371-383.

4) R. Tomisawa, T. Ikaga, K.H. Kim, Y. Ohkoshi, K. Okada, H. Masunaga, T. Kanaya, M. Masuda, Y. Maeda, *Polymer*, 116, (2017), 367-377.

5) W. Okumura, T. Kanegae, Y. Ohkoshi, Y. Gotoh, M. Nagura *Polymer Processing XVIII*, (2003), 1-7.

6) S.Kase, and T.Matsuo, *J. Polym. Sci. Part A*, 3, (1965), 2541.

7) W. Okumura, T. Yamaguchi, Y. Ohkoshi, Y. Gotoh, M. Nagura, *Intern. Polym. Proc.*, 17, (2002), 124-132.

8) R. Tomisawa, T. Ikaga, K.H. Kim, Y. Ohkoshi, K. Okada, H. Masunaga, T. Kanaya, M. Masuda, Y. Maeda, *Polymer*, 116, (2017), 357-366.

9) K. H. Kim, T. Murata, Y. A. Kang, Y. Ohkoshi, Y. Gotoh, M. Nagura, H. Urakawa, *Macromolecules*, 44, (2011), 7378-7384.

10) R. Hosemann, S. N. Bagchi, "*Direct Analysis of Diffraction by Matter*" (North-Holland, Amsterdam, 1962) Ch. 9.

11) J. Shimizu, T. Kikutani, A. Takaku, N. Okui, *Sen'i Gakkaishi*, 40, (1984), 177-183.

12) T. Kikutani et al. "*Fundamental and Practical Technologies for Nano-structured Polymeric Materials*", 2008, p.56-110, CMC press, ISBN978-4-7813-0043-6.

13) Y. Masubuchi, H. Watanabe, G. Iannirubeto, F. Greco, G. Marrucci, *Nihon Reoroji Gakkaishi*, 36, (2008), 181-185.

14) T. Asano, F. J. Balta Calleja, A. Flores, M. Tanigaki, M. Mina, C. Sawatari, H. Itagaki, H. Takahashi, I. Hatta, *Polymer*, 40, (1999), 6475-6484.

15) T.Yamaguchi, Y. Ohkoshi, Y. Gotoh, M. Nagura, *Seikei-Kakou*, 17, (2005), 649-653.

16) K. H. Kim, T. Yamaguchi, Y. Ohkoshi, Y. Gotoh, M. Nagura, H. Urakawa, M. Kotera, T. Kikutani, *J. Polym. Sci., Polym. Phys.*, 47, (2009), 1653-1665.

17) T. Yamaguchi, K. Komoriyama, Y. Ohkoshi, H. Urakawa, Y. Gotoh, N. Terasawa, M. Nagura, K. Kajiwara, *J. Polym. Sci., Polym. Phys.*, 43, (2005), 1090-1099.

18) A. Komoriya, R. Aida, K. H. Kim, Y. Ohkoshi, I. Wataoka, H. Urakawa, *Fiber preprints*, Japan, 56, (2010), 303.

19) D. Kawakami, B. S. Hsiao, C. Burger, S. Ran, C. Avila-Orta, I. Sics, T. Kikutani, B. Chu, *Macromolecules*, 38, (2005), 91-103.

20) S. Oneda, R. Tomisawa, T. Ikaga, K. H. Kim, Y, Ohkoshi, K. Okada, H. Masunaga, T. Kanaya, Y. Funatsu, M. Masuda, H. Katsuta, *Fiber preprints*, Japan, 72, (2017), 1B11.

21) K. Okada, K. Nakata, Y. Higashioji, K. Takahashi, Y. Ohkoshi, T. Kanaya, *Kobunshi Ronbunshu*, 71, 11, (2014), 593-600.

22) Y.Y. Tomashpol′skii, G.S. Markova, *Polym. Sci. USSR*, 6, (1964), 316-324.

23) A. I. Abou-Kandil, G. Goldbeck-Wood, A. H. Windle, *Macromolecules*, 40, (2007), 6448-6453.

24) I. Sakurada, T. Itou, *Koubunnsi Kagaku*, 19, (1962), 300-305.

Chapter 5

Ultra-SAXS observation of fibril-size structure formation after the necking of poly(ethylene terephthalate) and poly(phenylene sulfide) fibers

Chapter 5: Ultra-SAXS observation of fibril-size structure formation after the necking of poly(ethylene terephthalate) and poly(phenylene sulfide) fibers

1. Introduction

In this Chapter, we analyze the formation of the fibril-size structure after necking using ultra-small-angle X-ray scattering (USAXS), which enables observation of the void and craze formations. We attempted to obtain the USAXS image on the continuous drawing of the PET and PPS fibers. The fibrillar structure, which was several tens to hundreds of nanometers in diameter, was analyzed by the USAXS image.

2. Experimental

2.1. Sample

The fibers used for drawing were prepared by melt-spinning of PET (IV=1.32 dL/g) and PPS (MFR=120 g/10 min) provided by the Toray Co. The PET polymer was heated at 300 °C and the PPS polymer was heated at 330 °C. Both polymers were extruded from a one-hole nozzle at a mass flow rate of 5.0 g/min, and taken-up at 250 m/min. The nozzle diameter was 1.0 mm, and the length to diameter ratio was 3.

2.2. Drawing

Fibers were fed continuously from a feed roller, heated by irradiation with a CO_2 laser beam, and drawn based on the speed difference between the feed and take-up rollers [1]. The fiber running speed after necking was fixed at 110 m/min, and the draw ratio (DR) was changed by changing the feeding speed. A random polarized laser beam with wavelength and diameter of 10.6 μm and 6 mm, respectively, was generated using a PIN-30R laser (Onizuka Glass Co., Ltd.). The beam was used to irradiate the running fibers from three different directions. The laser power for each drawing condition was determined to enable fluctuations in the neck-drawing point to be minimized. The drawing tension was measured using a tension meter (HS-1500S, Eiko Sokki Co., Ltd.). A 100 gf pickup was installed between the neck-drawing point and the take-up roller. The drawing stress was calculated from the drawing tension and the diameter of the drawn fiber. The drawing conditions are shown in Table 5.1.

2.3. On-line measurement

USAXS images were obtained by X-ray irradiation of the running fiber during the continuous drawing. The on-line measurement system has been described in a previous report [1]. The distance from the necking point to the X-ray irradiation position was changed by moving the laser irradiation position. The elapsed time after necking was calculated by dividing the distance by the fiber running

speed.

The distance between the necking point and the X-ray irradiation position was measured with a CCD video camera (Watec Co., Ltd. WAT-232S type) that was placed coaxial to the X-ray beam using a mirror. The CCD video camera was equipped with a telecentric lens (OPTART Co., Ltd. TV-2S) with double magnification. The synchrotron X-ray beam used in this study was from SPring-8 BL03XU (FSBL), and an undulator was used to obtain an ultrahigh-intensity X-ray beam. The X-ray beam diameter was 10 μm, which was obtained through a 9 μm defining pinhole (50 mm-thick tantalum). Two pairs of Si crystals were arranged immediately downstream of the pinhole. The Si crystals were arranged vertically and horizontally under conditions that satisfy Bragg's diffraction angle. The parasitic scattering emitted from the defining pinhole was removed by the Si crystals. The Pilatus detector (DECTRIS Co. Pilatus3 S 1M), which has 1043×981 pixels (172 μm/pixel) was also used. The wavelength of the X-ray beam was 0.155 nm, the camera length was 7564 mm, and the exposure time was 60 s.

Time resolution was calculated using the same calculation method as previously reported [2]. Image processing could not be performed because the image extracted from the necking movie in this experiment was rough and blurred. Therefore, the time resolution was estimated by the length and the fluctuations of the necking with reference to those previously reported [2, 3]. That is, it was estimated that the neck fluctuation was 0.09–0.14 mm, the neck length was 0.13–0.28 mm for PET fibers, and the neck fluctuation was 0.095 mm, the necking length was 0.06 mm for PPS, where the size of the X-ray beam was 0.01 mm and the fiber running speed was 110 m/min. The estimated time resolution was 0.09–0.17 ms for PET and 0.06 ms for PPS.

2.4. Birefringence

Refer to section 2.4 of Chapter 2.

2.5. Thermomechanical tests

Refer to section 2.5 of Chapter 2.

3. Result and discussion

3.1. Properties and structures of fibers

The structure and properties of the PET and PPS fibers are shown in Table 5.1. The birefringence of the as-spun fibers was very small, approximately 0.0001, because both fibers were spun at the lowest speed at which stable winding could be achieved. The birefringence and tensile strength were increased, while the elongation was decreased with the increase of drawing stress for the PET fibers. It was considered that the larger drawing stress applied to the fiber oriented the molecular chains to the fiber axis, and increased the fiber strength.

Table 5.1 Structure and physical properties of the drawn fibers

Sample	Draw ratio	Drawing stress /MPa	Birefringence	Tensile strength / MPa	Elongation / %	Young's modulus / GPa	Thermal shrinkage / %	Melting temperature / °C	Heat of fusion / J/g	Crystallinity / %
PET	4.4	61	0.165	759	50	9.7	16	254	46	34
	5.0	105	0.179	944	33	10.9	19	255	52	38
	5.6	188	0.193	1087	26	10.8	20	256	53	40
PPS	4.3	100	-	677	24	6.4	14	283	40	28

3.2. Neck drawing and fiber temperature

From Table 5.1, PET was drawn with DR 4.4, 5.0 and 5.6 and PPS was drawn with DR of 4.3. The drawing stress was 61–188 MPa for PET and 100 MPa for PPS. PPS could be drawn in an extremely narrow drawable range of 4.2 to 4.4, and thus, was measured only with a draw ratio of 4.3.

The fiber temperatures around the necking point were estimated. The estimated profile was obtained on the basis of an energy balance equation considering temperature rise by laser irradiation, cooling by heat transfer from the fiber surface, work of plastic deformation by an external force, and the latent heat of crystallization [4]. The heat of crystallization was determined using the heat of fusion of the drawn fibers measured by DSC (Table 5.1). The crystallization induction time and crystallization rate were assumed, as shown in Table 5.2, with reference to the results of a previous report [3] and the value obtained by Ide et al. [2]. The estimated fiber temperature is shown in Table 5.2.

**Table 5.2** Fiber temperatures estimated for the drawing conditions

| Sample	Draw Ratio	Crystallization induction time / ms	Crystallization rate / x10³/s	Temperature immediately before the neck / °C	Temperature immediately after the neck / °C	Max. Temp. & Time / °C(/ ms)
PET	4.4			83	109	152 (2.4)
	5.0	0.6*	2.3*	100	140	185 (2.3)
	5.6			109	180	222 (2.4)
PPS	4.3	0.02	3	76	119	163 (2.0)

*assumed value

3.3. USAXS pattern

The USAXS images obtained by subtracting air scattering are shown in Fig. 5.1. Fig. 5.1(a) shows the scattering patterns of each elapsed time and draw ratio, and Fig. 5.1 (b) and (c) show the typical USAXS scattering pattern for PET and PPS. The horizontal direction of the figure shows the equatorial direction and the vertical direction shows the meridional direction. As shown in Fig. 5.1 (c), three streaks were observed for the USAXS pattern of PPS, which were meridional and equatorial streaks and total reflection. In addition to the three streaks observed for PPS, a layer-lined streak was observed for PET (Fig. 5.1 (b)). The extremely strong and thin streak overlapped with the streak of the fibril-sized structure in the equatorial direction. This should be the total reflection from the fiber surface. The total reflection could be cut off greatly by made a thinner X-ray beam. Although an X-ray beam approximately 1/6 of the fiber diameter was used in this study, we could not completely prevent the total reflection because the fiber fluctuated slightly along the perpendicular direction to the fiber axis. However, the total reflection could be distinguished clearly from the equatorial scattering because it was so sharp. Its influence was limited in a very narrow range around the equator.

Fig. 5.1(a) shows the USAXS pattern changing with the elapsed time. The negative elapsed time represents the data before necking, and 0 ms denotes the image taken at the necking point. Before necking, meridian and equatorial streaks were observed for PPS, while an equatorial streak was observed for the as-spun PET fiber. Upon necking, both equatorial and meridional streak intensities greatly increased. A layer-lined streak and meridional streak also appeared. However, the layer-lined streak for DR 5.6 was unclear. After then, the meridian streak was weakened with elapsed time.

(a)
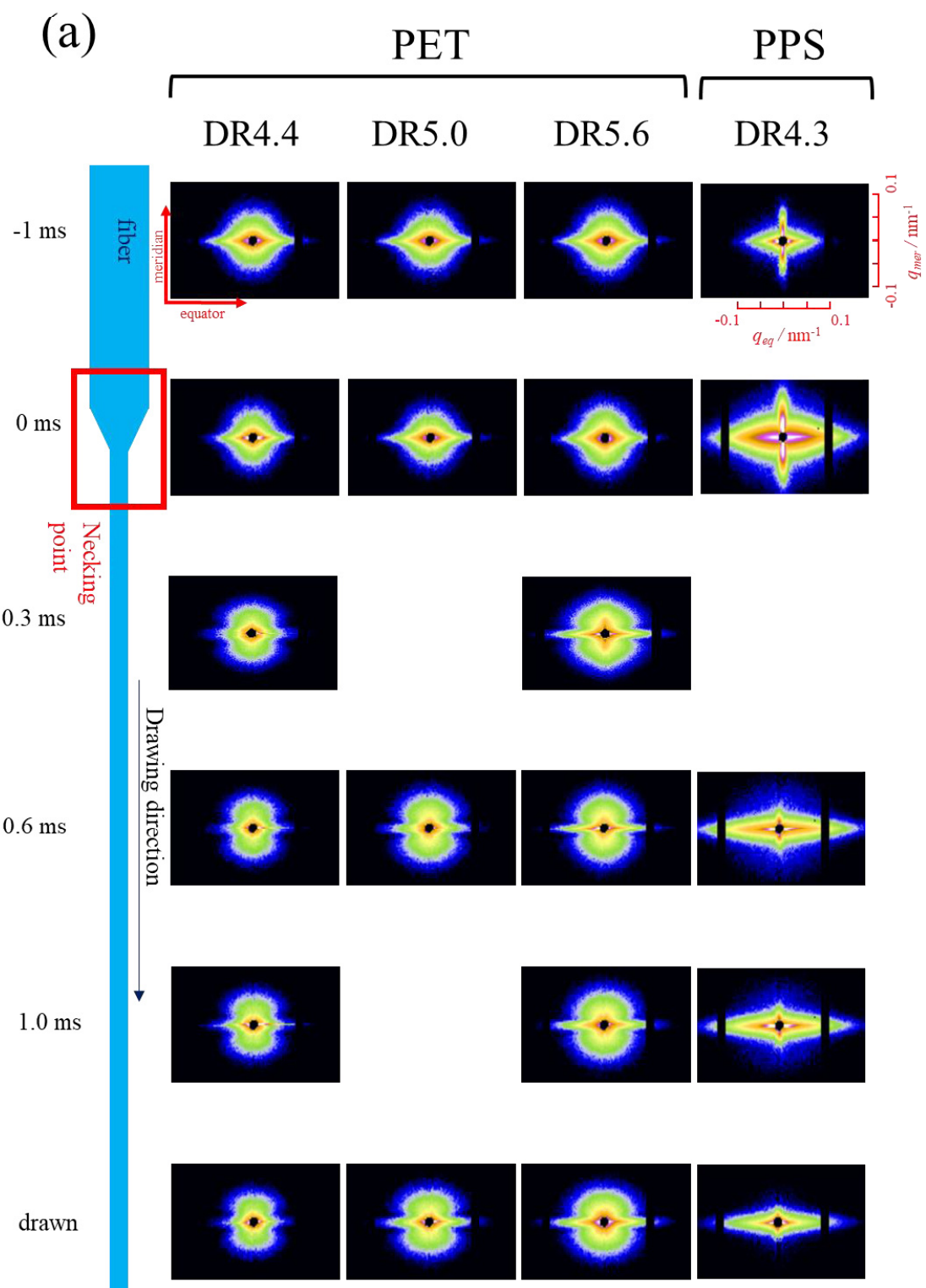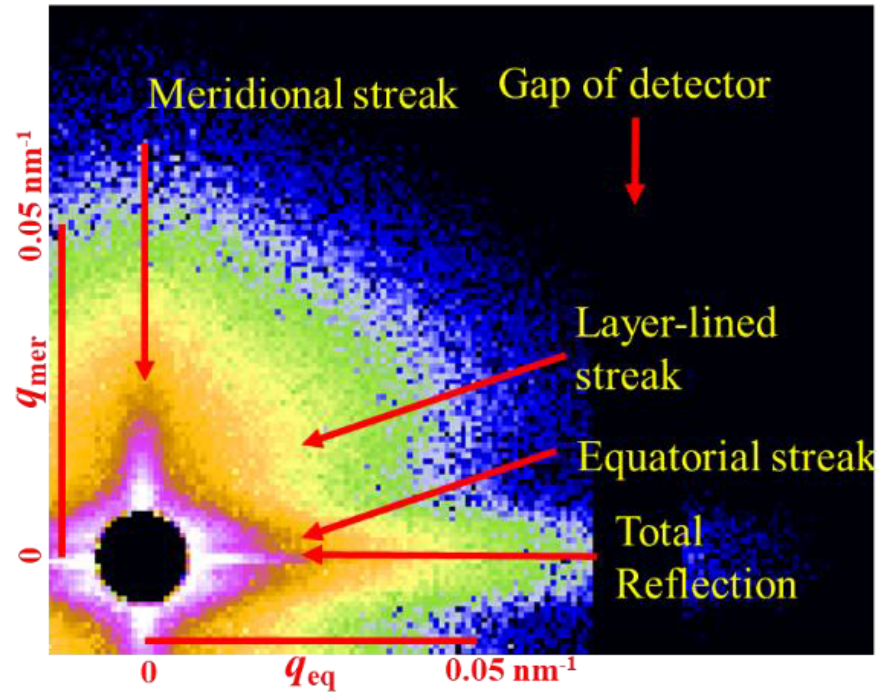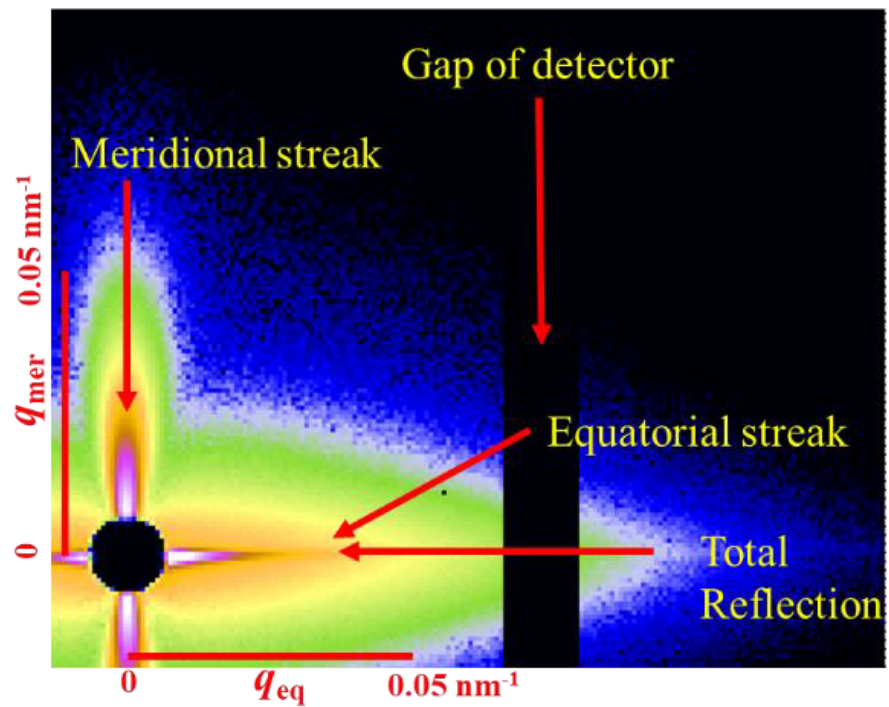
Fig. 5.1 (a) USAXS images of PET and PPS fibers at corresponding elapsed times after necking. The elapsed times after necking are noted in the figures. Typical USAXS image of (b) PET fiber with DR 5.6 at 0.1 ms and (c) PPS fiber with DR 4.3 at 0 ms after necking. q_{eq} and q_{mer} are the scattering vectors along equatorial and meridional direction, respectively.

3.4. Meridional streak

The meridional intensity profile of the USAXS image is shown in Fig. 5.2. The measured range of scattering vector q from 0.007 to 0.15 nm^{-1} corresponds a size of the scattering body of 50–900 nm. A meridian peak at q_{mer} of 0.012 nm^{-1} was observed only for PPS at -1.0 - 0 ms, and disappeared after necking. The corresponding size of the period was approximately 500 nm. For both PET and PPS, the intensity of the meridian streak took the maximum immediately after necking. The maximum intensity for PPS was more than 10 times larger than PET, and the intensity increased with the increase of drawing stress for PET. After that, the intensity decreased with the elapsed time for both PET and PPS. However, the streak intensity of the drawn PET fiber was still larger than that for as-spun PET fiber, while the intensity of the drawn PPS fiber became smaller than that before drawing. Furthermore, a broad shoulder appeared around q_{mer} = 0.03 nm^{-1} at DR 4.4 and 5.0 for PET, while this was not observed for DR 5.6. The corresponding size for the shoulder was approximately 200 nm.

The meridional peak observed at -1.0 ms showed a periodic density fluctuation along the fiber axis in the as-spun PPS fiber. The density fluctuation amplified by the necking was thought to arise from the craze formed in the lower density region. The elongational deformation of necking should form a craze, and the weakening of the meridional streak means the collapse of the craze. The larger intensity increase in PPS, indicating larger amount of craze forming, should be caused by the density fluctuation already formed in the as-spun fiber.
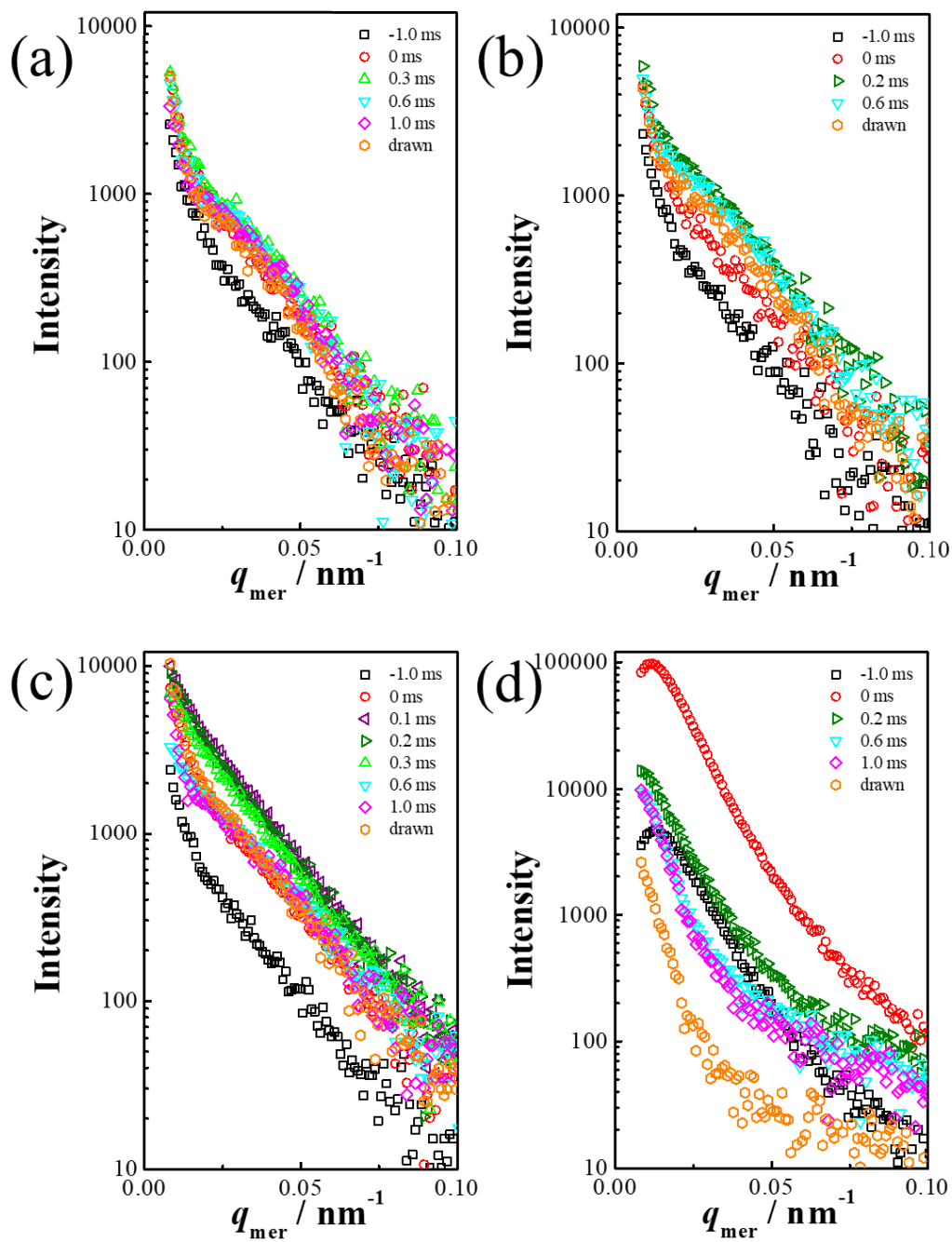
Fig. 5.2 Meridional intensity profiles. (a) PET, DR4.4, (b) PET, DR5.0, (c) PET, DR5.6, and (d) PPS DR4.3. Elapsed times are noted in figures.

3.5. Layer-lined streak and equatorial streak

To analyze this equator and layer-lined streaks, the USAXS image was analyzed as follows. Fig. 5.3 shows the intensity profiles along the meridional direction (q_{mer}). When q_{mer} exceeded 0.02 nm^{-1}, the peak of the layer-lined streak could be distinguished from the equatorial peak. To separate the components of the equatorial streak and layer-lined streak, the intensity profile was fitted by a Gaussian function, as shown in Fig. 5.4. The layer-lined streak was assumed to be symmetrical to the equatorial axis. Prior to the peak fitting, we deleted several data to eliminate the total reflection. Because the total reflection was far sharper than the equatorial streak, it could be ignored except for the very narrow range of q_{mer}. The deleted data range was $|q_{mer}| < 0.0037$ nm^{-1} for PET, and $|q_{mer}| < 0.0055$ nm^{-1} for PPS.

The equatorial profiles obtained by the fitting are shown in Fig. 5.5. For PET with DR 4.4, the intensity profile of equatorial streak did not change much with the elapsed time, while the intensity clearly increased by the necking for the larger draw ratios. In addition, as it was clearly shown for DR 5.6, the intensity continued to increase, and tended to be saturated at 1.0 ms. In contrast, for PPS, the intensity was drastically increased by the necking, and decreased with the elapsed time. The intensity increase by necking was far larger than the increase observed for PET.

The equatorial streak indicated a density fluctuation of several hundred nanometers perpendicular to the fiber axis, which seemed to be the density difference between so-called fibril and inter-fibrillar void. The larger increase of the streak intensity observed for PPS and the higher ratio drawn PET seemed to indicate the formation of a larger amount of inter-fibrillar voids. In contrast, the intensity decrease should indicate the dissipation of the voids. The large decrease of the PPS intensity seemed to be caused by the dissipation of inter-fibrillar voids formed by the necking. However, although the inter-fibrillar void should also collapse with the elapsed time for PET, it rather increased with time in particular for DR 5.6. This could be explained by the voids formed by the crystallization, which occurred less than 1.0 ms after necking [3].

The position of the layer-lined peak along q_{mer} were plotted against q_{eq} (Fig. 5.6). The streak appeared immediately after necking, and its position was hardly changed with elapsed time. The position also hardly changed with the draw ratio, but the peak separation became difficult owing to the decrease of the streak intensity, in particular at low q_{eq}. The position of the peak was inclined approximately 20° from the equator, which was similar to the inclination of the X-pattern observed for SAXS [3]. Therefore, it should not be a simple layer-lined streak, but it can be thought as a meridional shoulder peak observed around $q_{mer} = 0.03$ nm^{-1} overlapped with the X-shaped streak.
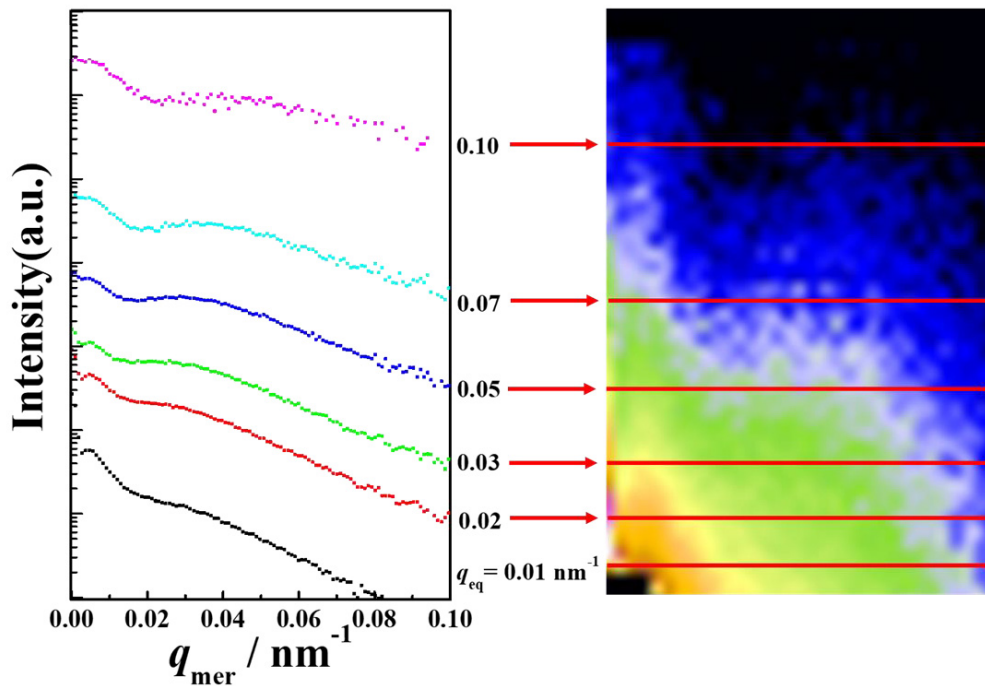
Fig. 5.3 Intensity profile along the meridional direction at each q_{eq} obtained by a PET drawn fiber with DR 4.4 at 0.3 ms after necking. The q_{eq} are noted in the figure.
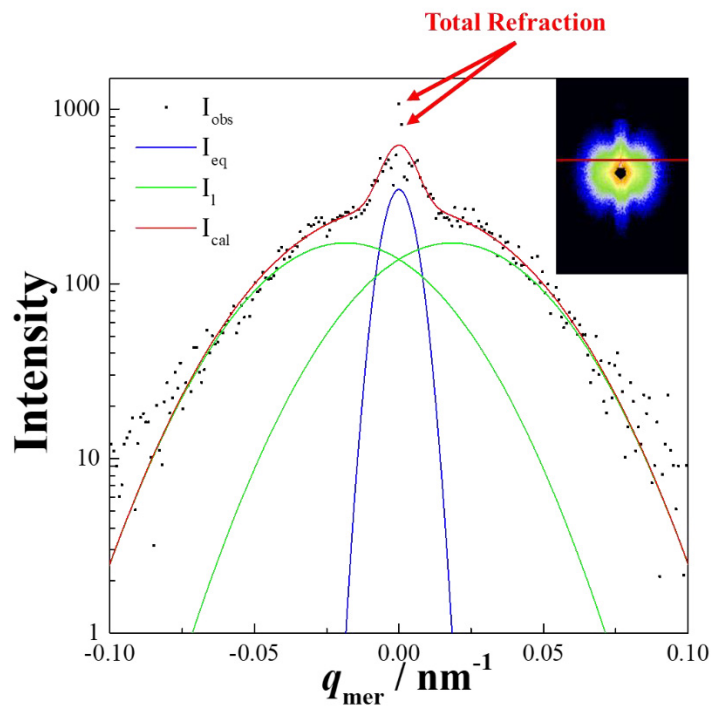
Fig. 5.4 An example of peak fitting for 4.4 times drawn PET fiber at 0.3 ms after necking. The intensity profile along the meridian direction at $q_{eq} = 0.023$ was fitted by the Gaussian equatorial scattering (I_{eq}) and symmetrical layer-lined scatterings (I_l) after deleting total reflection influenced data.
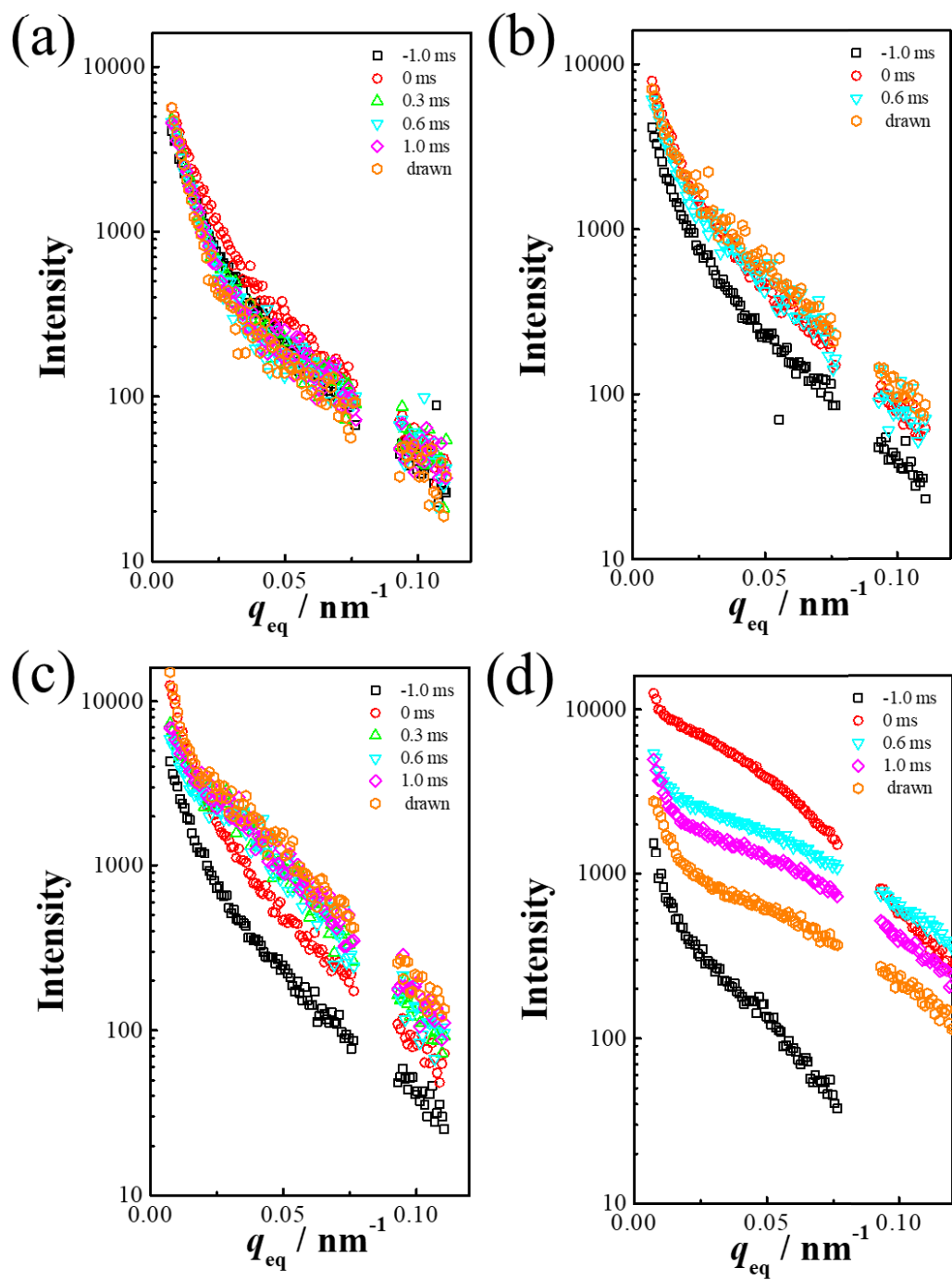
Fig. 5.5 Equatorial intensity profiles obtained from peak fitting, like in Figure 3. (a) PET, DR 4.4, (b) PET, DR 5.0, (c) PET, DR 5.6, and (d) PPS DR 4.3. Elapsed times are noted in the figure.
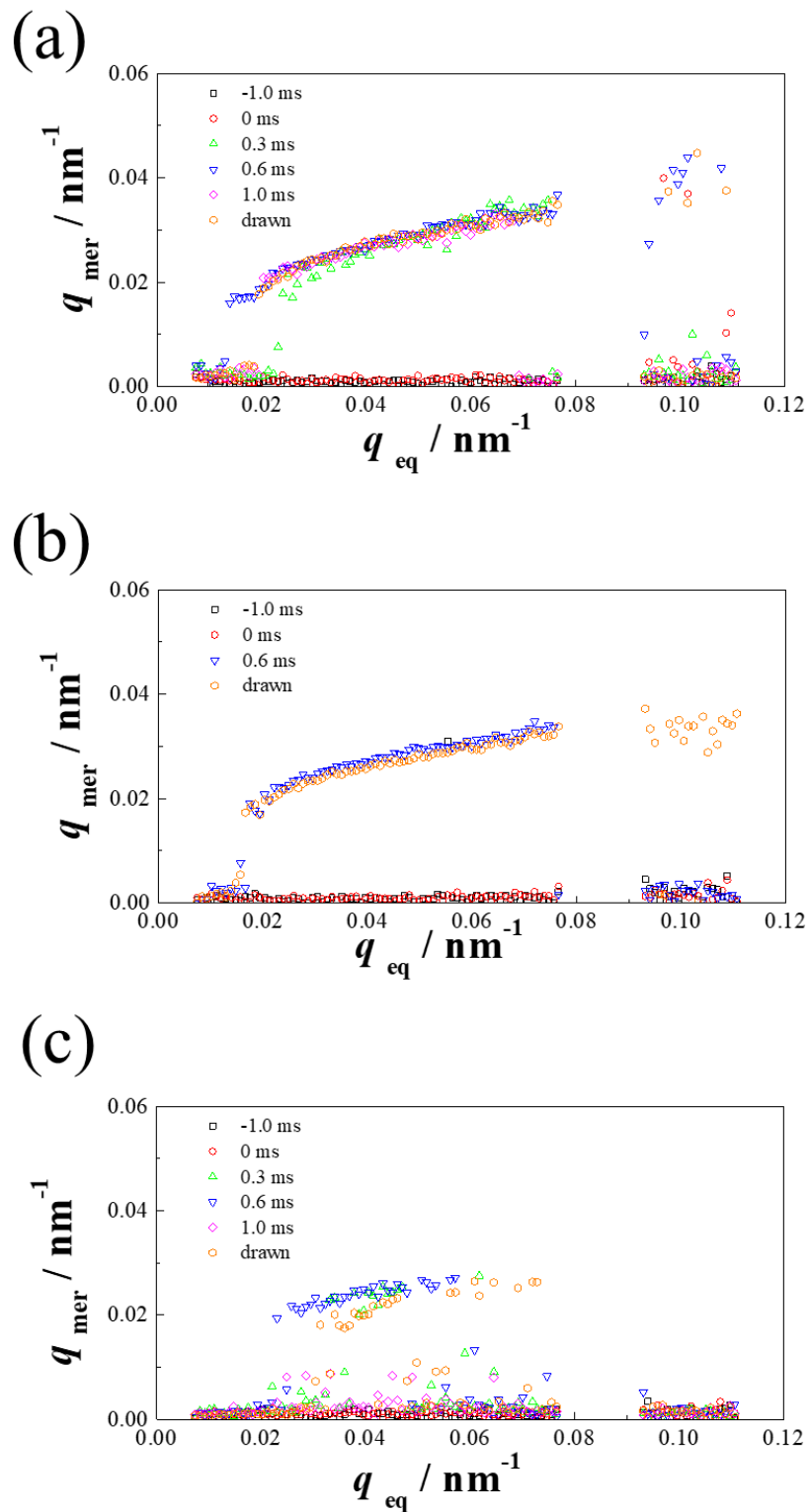
Fig. 5.6 Peak position of the layer-lined streak. Draw ratio (a) 4.4, (b) 5.0 and (c) 5.6. Elapsed times are noted in the figure.

### 3.6. Fibril-size structure development of PET and PPS

It is interesting that the USAXS patterns of PET and PPS were different although their SAXS patterns were similar. That is, both of them showed an X-shaped SAXS streak changing to a 4-point pattern [13, 20]. However, only PET showed the layer-lined USAXS streak, and PPS showed a far stronger USAXS meridional streak than PET. The layer-lined USAXS streak of PET can be explained by the fibrillar-shaped smectic phase formed less than 1.0 ms after necking, and its growing to microfibril [1]. This smectic phase is a metastable structure, first reported by Bonart [5], and has been formed during batch drawing [6] and heat treatment of oriented amorphous PET [7]. The smectic phase has also been observed for PEN [8] and PBT [9], although it has not been observed for PPS [2]. The period of 200 nm, corresponding to the layer-lined USAXS streak, can be assumed as the period of layered bundle of a fibrillar-shaped smectic phase of approximately 70 nm in length [1] and inter-fibrillar molecules. A far stronger meridional streak of PPS should be caused by the periodic density deviation preliminary formed in the as-spun fiber. Because of the density deviation along the fiber axis, craze formation preferentially occurred by necking for PPS, whereas slippage between the fibril-forming molecules preferentially occurred in the PET.

3.7. Model of the microfibril structure depends on the draw ratio

A schematic diagram of the drawing stress dependence on the fiber structure development is shown in Figure 5.7. This model is based on results for the minimum drawing stress mentioned in Chapter 3 and the larger drawing stress obtained in this study. For the minimum draw ratio, which was almost the same as the NDR, no smectic phase was observed. The maximum persistence length and the proportion of smectic phase increased with drawing stress but effectively saturated over 80 MPa. Moreover, an X-shaped SAXS pattern was observed only for the minimum draw ratio (See Chapter 3), and the intensity of the layer-lined USAXS streak decreased with the draw ratio. Hence, the crystallites that formed along the shear-band-like structure for the minimum drawing stress changed to a fibrillar smectic phase under a medium drawing stress. The arrangement of the fibrillar smectic phases along the shear-band-like structure became unclear at the maximum drawing stress.

As shown in Chapter 4, after saturation of the microfibril length and proportion, the Young's modulus and birefringence also saturated; however, the strength and thermal shrinkage stress of the drawn fiber continued to increase with drawing stress. The further increase in the strength and thermal shrinkage stress can be explained by the increase in the number and orientation of the inter-microfibrillar tie-chains connecting fibrils. The number and orientation of the inter-microfibrillar tie-chains should be lower than those of intra-microfibrillar tie-chains connecting crystallites in fibrils because inter-microfibrillar tie-chains consist of entanglement and molecular chain ends excluded from the oriented chain bundles whereas the intra-microfibrillar tie-chains should be formed by the fibrillar smectic phase.

Similar models that include a microfibril structure have already been proposed by Prevorsec [11] and Peterlin [12]. The originality of the current model is in the quantitative analysis of the fibrillar structure, in terms of the modulus, proportion, size, disordering, and arrangement. Through our analysis, the number and orientation of the inter-microfibrillar tie-chains can be discussed in greater detail. The relationship between the fibril structure formation and the uniformity of the network structure can also be discussed through the model. Hence, the mechanical and thermal properties of the fibers and films can be designed by choosing more appropriate processing conditions.
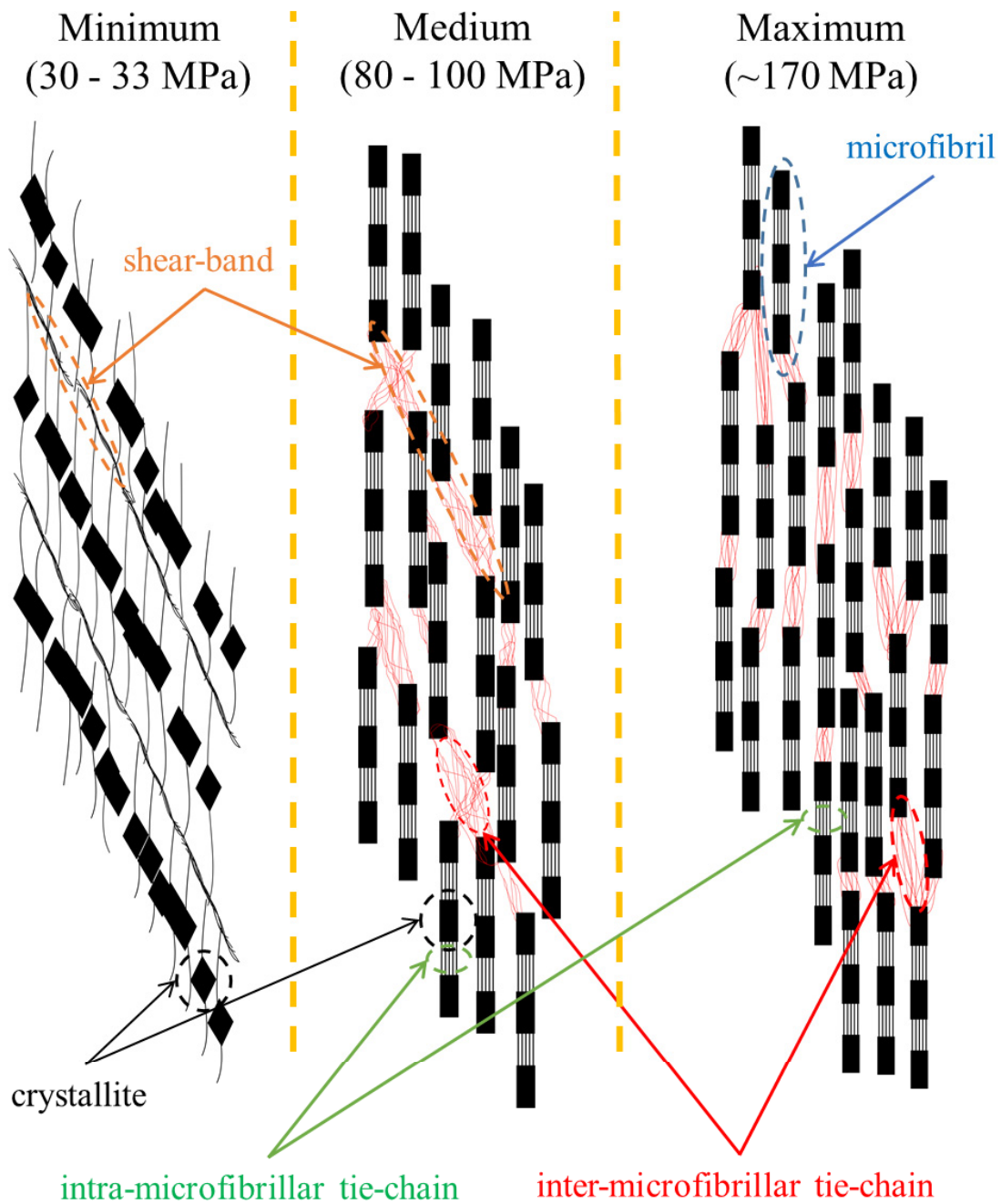
Fig. 5.7 Schematic diagram of the drawing stress dependence on the fibril structure.

4. Conclusions

We analyzed the formation of the fibril-size structure after necking using USAXS, which enables observation of the void and craze formations. Continuous laser-heated drawing and undulator synchrotron radiation are adopted to measure the structural development of PET and PPS fibers. PET was drawn with DR 4.4, 5.0 and 5.6 and PPS was drawn with DR of 4.3. The drawing stress was 61–188 MPa for PET and 100 MPa for PPS.

Three streaks were observed for the USAXS pattern of PPS, which were meridional and equatorial streaks and total reflection. In addition to the three streaks observed for PPS, a layer-lined streak was observed for PET. A meridian peak corresponding about 500 nm period was observed only for PPS before necking. Both fibers show an obvious increase in the meridional streak intensity just after necking, and an increase in the equatorial streak after necking. These increases are distinctive for PPS. Moreover, a layer-lined streak appeared after necking only for PET. The intensity of the meridian streak increased with the increase of draw ratio, whereas the intensity of layer-lined scattering decreased with the increase of draw ratio.

Far stronger meridional streak of PPS should be caused by the periodic density deviation preliminary formed in the as-spun fiber, and the layer-lined USAXS streak of PET can be explained by the periodic bundle of a fibrillar-shaped smectic phase.

Reference

1) T. Yamaguchi, K. H. Kim, T. Murata, M. Koide, S. Hitoosa, H. Urakawa, Y. Ohkoshi, Y. Gotoh, M. Nagura, M. Kotera, K. Kajiwara, *J. Polym. Sci., Polym. Phys.*, 46, (2008), 2126-2142.

2) K. Ide, T. Ikaga, Y. Ohkoshi, I. Wataoka, M. Masuda, and Y. Maeda, *Sen'i Gakkaishi*, 70, (2014), 4.

3) R. Tomisawa, T. Ikaga, K.H. Kim, Y. Ohkoshi, K. Okada, H. Masunaga, T. Kanaya, M. Masuda, Y. Maeda, *Polymer, 116C*, (2017), 357-366.

4) W. Okumura, T. Yamaguchi, Y. Ohkoshi, Y. Gotoh, M. Nagura, *Intern. Polym. Proc.*, 17, (2002), 124-132.

5) R. Bonart, *Kolloid-Z*, 213, (1966), 1-11.

6) K. Okada, K. Nakata, Y. Higashioji, K. Takahashi, Y. Ohkoshi, T. Kanaya, *Kobunshi Ronbunshu*, 71, 11, (2014), 593-600.

7) T. Asano, F. J. Balta Calleja, A. Flores, M. Tanigaki, M. Mina, C. Sawatari, H. Itagaki, H. Takahashi, I. Hatta, *Polymer*, 40, (1999), 6475-6484.

8) K. H. Kim, R. Aida, Y. A. Kang, T. Ikaga, Y. Ohkoshi, I. Wataoka, H. Urakawa, *Polymer*, 53, (2012), 4272-4279.

9) T. Konishi, Y. Miyamoto, *Polymer*, 42, (2010), 349-353.

10) P. Gulgunje, G. Bhat, and J. Spruiell, *Journal of Applied Polymer Science*, 125, (2012), 1890.

11) D. C. Prevorsec, *J. Polymer Sci. Symposium* no. 32 (1971).

12) A. Peterlin, *J. Polym. Sci.*, A-2, 7, (1969), 1151.

Chapter 6

Conclusions

Chapter 6: Conclusions

The force-bearing structure of PET fiber is important because it dominate the fiber properties. The structure is determined by the melt spinning and drawing conditions. In this study, the effects of melt spinning and drawing conditions on the force-bearing structure of PET fiber were investigated by using the on-line measurement. Relationships between the structure and thermomechanical properties of the obtained fibers were also discussed.

In Chapter 2, the effects of spinning conditions on the structure development of PET fibers after necking were analyzed by WAXD/SAXS measurements. Fibers obtained with a spinning speed of 500–2000 m/min were used for the measurements. The fibers obtained from laser spinning using a CO_2 laser beam irradiated onto the fiber at the melt spinning line were also analyzed. The as-spun fibers were drawn continuously at the minimum stable draw ratio and under a drawing stress of about 100 MPa. An X-shaped SAXS pattern was observed about 0.3 ms after necking for all fibers drawn at the minimum stable draw ratio. In contrast, clear dependence of the structure development on spinning speed was observed for fibers drawn under a drawing stress of 100 MPa. A higher crystallization rate and clear draw ratio dependence of crystallization rate were also observed for the fiber spun at 2000 m/min despite it having the lowest fiber temperature and smallest difference in drawing stress of the fibers investigated. These results suggest the crystallites were mainly developed from the oriented nuclei formed in the spinning process for the fibers spun at 2000 m/min, while they mainly formed by the phase separation of the fibrillar smectic phase for the fibers spun at 500–1500 m/min.

In Chapter 3, we investigated the effects of draw ratio on the fiber structure development of PET during continuous drawing. The fibers spun at 500 m/min are drawn at drawing stress from 22 to 149 MPa. The crystallites mainly formed by the phase separation of the fibrillar smectic phase in this condition as mentioned above. An X-shaped SAXS pattern was observed, but no (001′) smectic phase diffraction was observed for the minimum stable draw ratio. The (001′) diffraction intensity increased up to draw ratio of 4.2, then it saturated. The long period clearly decreased within 1 ms after necking and it increased with increase of draw ratio. However, no clear draw ratio dependences of the crystallization rate and induction time, 2.3–2.8 ms^{-1} and 0.4–0.6 ms, respectively, were observed.

In Chapter 4, the effects of dimensions and regularity of fibrillar-shaped smectic phase on mechanical properties of fiber were investigated by high-precision X-ray measurements with the use of the SOPHIAS detector. The drawing stress was set to be 76–168 MPa, at which range the proportion of the smectic phase is almost saturated as mentioned in Chapter 3. The spinning speed dependence for 250–2000 m/min was also measured under a fixed drawing stress of approximately 100 MPa. Changes in the proportion, d-spacing, persistence length, and thickness of the smectic phase were measured from the intensity, peak position, and widths of the smectic (001′) diffraction peaks, from just before necking to 1 ms after necking. Hosemann′s g_{II} parameters were also determined from the

meridian widths of the (001′) diffraction peak, and the (003′) and (005′) diffraction peaks obtained by inclined measurements. The proportion, persistence length (50–70 nm) and thickness achieved maximum values and g_{II} reached a minimum value (3.7–4.3%) at 0.3–0.4 ms after necking. The minimum value of g_{II} increased with the spinning speed but showed little dependence on the drawing stress. The larger g_{II} value observed here than that of a previously reported crystalline phase and the increase of g_{II} value with spinning speed can be explained by the incomplete axial shift between molecular chains.

The persistence length and NDR of the as-spun fiber showed a linear relationship and a greater decrease in the persistence length than the NDR was observed at more than 1500 m/min. The trend confirmed the validity of the obtained persistence length as a structural parameter for estimating the uniformity in the entanglement density of polymer chain networks and the maximum attainable strength of the resulting fibers. The maximum value of the proportion and persistence length and thickness showed almost no dependence on the drawing stress. However, the proportion and persistence length increased more rapidly with drawing stress, and the thickness decreased more rapidly for the maximum drawing stress. The d-spacing of the smectic phase tended to decrease with the fiber temperature. Because the value extrapolated to room temperature almost corresponded to the c-axis length of crystal, the smectic phase could be regarded as a bundle consisting of perfectly oriented and almost fully extended molecular chains. By increasing the d-spacing with a drawing stress, an apparent elastic modulus of approximately 40 GPa was obtained for the oriented molecular bundle. This value suggests that external force concentrates on inter-microfibrillar tie-chains during tensile testing.

In Chapter 5, we analyzed the formation of the fibril-size structure after necking using USAXS. PET was drawn with DR 4.4, 5.0 and 5.6 and PPS was drawn with DR of 4.3. The drawing stress was 61–188 MPa for PET and 100 MPa for PPS. Three streaks were observed for the USAXS pattern of PPS, which were meridional and equatorial streaks and total reflection. In addition to the three streaks observed for PPS, a layer-lined streak was observed for PET. A meridian peak corresponding about 500 nm period was observed only for PPS before necking. Both fibers show an obvious increase in the meridional streak intensity just after necking, and an increase in the equatorial streak after necking. These increases are distinctive for PPS. Moreover, a layer-lined streak appeared after necking only for PET. The intensity of the meridian streak increased with the increase of draw ratio, whereas the intensity of layer-lined scattering decreased with the increase of draw ratio. Far stronger meridional streak of PPS should be caused by the periodic density deviation preliminary formed in the as-spun fiber, and the layer-lined USAXS streak of PET can be explained by the periodic bundle of a fibrillar-shaped smectic phase.

Although no marked differences of birefringence, crystallinity, and SAXS patterns were observed for the drawn fibers, there were clear differences in their tensile strength and thermal shrinkage

behavior. From Chapter 4 and 5, the larger increase in tensile strength and thermal shrinkage stress than that in the Young's modulus and birefringence with the increase of drawing stress can be explained by the difference in the number and orientation of inter-microfibrillar tie-chains and the uniformity of them.

Publications

The dissertation is based on the following published papers.

Journal of articles

- <u>Ren Tomisawa</u>, Toshifumi Ikaga, KyoungHou Kim, Yutaka Ohkoshi, Kazuyuki Okada, Hiroyasu Masunaga, Toshiji Kanaya, Masato Masuda, Yuhei Maeda, *Polymer*, 116, (2017), 367-377.

- <u>Ren Tomisawa</u>, Toshifumi Ikaga, KyoungHou Kim, Yutaka Ohkoshi, Kazuyuki Okada, Hiroyasu Masunaga, Toshiji Kanaya, Masato Masuda, Yuhei Maeda, *Polymer*, 116, (2017), 357-366.

- <u>Ren Tomisawa</u>, Shun Oneda, Toshifumi Ikaga, KyoungHou Kim, Yutaka Ohkoshi, Kazuyuki Okada, Hiroyasu Masunaga, Toshiji Kanaya, Yoshitsugu Funatsu, Hiroo Katsuta, *Polymer*, 164, (2019), 163-173.

- <u>Ren Tomisawa</u>, Takumi Ando, Toshifumi Ikaga, KyoungHou Kim, Yutaka Ohkoshi, Kazuyuki Okada, Hiroyasu Masunaga, Toshiji Kanaya, Yoshitsugu Funatsu, Hiroo Katsuta, *Polymer Journal*, 51, (2019), 211-219.

Conferences

A part of the dissertation was presented in conferences as the following.

Oral presentations

- 第 26 回プラスチック成形加工学会年次大会: 冨澤錬、菅原昂亮、伊香賀敏文、大越豊、岡田一幸、増永啓康、金谷利治、増田正人、前田裕平、Poly(ethylene terephthalate)の繊維構造形成におよぼす巻取速度およびレーザー紡糸の影響

- 平成 27 年度繊維学会秋季研究発表会: 冨澤錬、伊香賀敏文、大越豊、岡田一幸、増永啓康、金谷利治、増田正人、前田裕平、ポリエチレンテレフタレート（PET）の繊維構造形成におよぼす製造条件の影響　(1)延伸倍率の効果

- 平成 27 年度繊維学会秋季研究発表会: 冨澤錬、伊香賀敏文、大越豊、岡田一幸、増永啓康、金谷利治、増田正人、前田裕平、ポリエチレンテレフタレート（PET）の繊維構造形成におよぼす製造条件の影響　(2) 巻取速度およびレーザー紡糸の効果

- 第 27 回プラスチック成形加工学会年次大会: 冨澤錬、大根田俊、伊香賀敏文、金慶孝、大越豊、岡田一幸、増永啓康、金谷利治、船津義嗣、増田正人、勝田大士、Poly(ethylene terephthalate)の繊維構造形成におよぼす延伸倍率の影響

- 平成 30 年度繊維学会年次大会: 冨澤錬、安藤巧、伊香賀敏文、大越豊、岡田一幸、増永啓康、金谷利治、船津義嗣、勝田大士、ポリエチレンテレフタレートおよびポリフェニレンサルファイド繊維のネック変形直後におけるフィブリルとクレーズの形成

- The 12th SPSJ International Polymer Conference: Ren Tomisawa, Yutaka Ohkoshi, KyoungHou Kim, Takumi Ando, Toshifumi Ikaga, Kazuyuki Okada, Hiroyasu Masunaga, Toshiji Kanaya, Yoshitsugu Funatsu and Hiroo Katsuta, Ultra-SAXS observation of fibril-size structure formation after the necking of poly(ethylene terephthalate) and poly(phenylene sulfide) fiber

Poster presentations

- 平成 26 年度繊維学会年次大会: <u>冨澤錬</u>、菅原昂亮、伊香賀敏文、大越豊、岡田一幸、増永啓康、金谷利治、増田正人、前田裕平、PET の繊維構造形成におよぼす溶融紡糸条件の影響

- 第 26 回プラスチック成形加工学会年次大会: <u>冨澤錬</u>、菅原昂亮、伊香賀敏文、大越豊、岡田一幸、増永啓康、金谷利治、増田正人、前田裕平、Poly(ethylene terephthalate)の繊維構造形成におよぼす巻取速度およびレーザー紡糸の影響

- 第 27 回プラスチック成形加工学会年次大会: <u>冨澤錬</u>、大根田俊、伊香賀敏文、金慶孝、大越豊、岡田一幸、増永啓康、金谷利治、船津義嗣、増田正人、勝田大士、Poly(ethylene terephthalate)の繊維構造形成におよぼす延伸倍率の影響

- The 14th Asian Textile Conference 2017: <u>Ren Tomisawa</u>, Yutaka Ohkoshi, KyoungHou Kim, Shun Oneda, Toshifumi Ikaga, Masato Masuda, Yuhei Maeda, Kazuyuki Okada, Hiroyasu Masunaga, and Toshiji Kanaya, Dimensions and stability of smectic phase formed on the structure development of poly(ethylene terephthalate) fiber

- 平成 28 年度第 46 回繊維学会夏季セミナー: <u>冨澤錬</u>、大根田俊、伊香賀敏文、金慶孝、大越豊、岡田一幸、増永啓康、金谷利治、船津義嗣、増田正人、勝田大士、Poly(ethylene terephthalate)の繊維構造形成におよぼす延伸倍率の影響

- 平成 30 年度繊維学会年次大会: <u>冨澤錬</u>、大根田俊、伊香賀敏文、大越豊、岡田一幸、増永啓康、金谷利治、船津義嗣、勝田大士、ポリエチレンテレフタレートの配向誘起結晶化過程で形成される smectic 相におよぼす紡糸・延伸条件の効果